THE RAPID ACQUISITION AND APPLICATION OF GEOPHYSICAL DATA TO THE SUSTAINABLE AND PROFICIENT MANAGEMENT OF SHALLOW AQUIFERS AND CEMETERIES

A Dissertation

by

JACOB MICHAEL MARTIN

Submitted to the Graduate and Professional School of
Texas A&M University
in partial fulfillment of the requirements for the degree of

DOCTOR OF PHILOSOPHY

Chair of Committee,	Mark E. Everett
Committee Members,	Peter S. K. Knappett
	Ryan C. Ewing
	Binayak P. Mohanty
Head of Department,	Julie Newman

May 2022

Major Subject: Geophysics

ABSTRACT

Rapidly acquired non-invasive geophysical data is key to reducing the risk inherent in subsurface investigations. It achieves this risk reduction by provision of spatiotemporally dense datasets and new methods to measure the efficacy of acquisition, analysis, and modeling. In a first example, I use two geophysical methods—electrical resistivity tomography and time-domain electromagnetics—to investigate the subsurface in a rapidly urbanizing alluvial floodplain setting. Specifically I focus on the geologic structure of a shallow alluvial aquifer in the Brazos River floodplain of Texas, characterizing dynamic hydrological interactions between the aquifer and the adjacent river. Based on new geophysical insights, I determine how the sedimentary architecture of the shallow alluvial aquifer acts as a control on its recharge and discharge and how bidirectional preferential flow pathways establish hydrologic communication between the aquifer and the river at human and geologic time scales. In a second example, I develop a protocol to improve identification of unmarked graves in a historic African-American cemetery. I show that a geophysicist's detection proficiency, expressed in terms of true-positive, true-negative, false-positive, and false-negative percentages, can be improved using radar signatures of nearby known targets as a proxy for ground-truth.

ACKNOWLEDGEMENTS

I am most grateful to my Creator and Redeemer Jesus Christ, who has spent the last five years teaching me the limitations of my capabilities and the sufficiency of His love, favor, and power. It has been an incredible privilege to research the wonders and beauty of Your creation.

I thank my advisor, Prof. Mark E. Everett, for the privilege of researching the wonders of the natural world alongside him as well as for the opportunity to teach undergraduates and serve the community together. The combination of these three made my time in this program a joy and delight.

I am thankful for the many hours put in by those who helped with fieldwork: Sidney Dangtran, Justin Estep, Nehe Jeon, Patrick Nebel, Potpreecha Pondthai, and Amir Sedaghatdoost (graduate students); Timothy Carpp, Changing Fan, Anne Fosli, Bronte Heerdink, Emily Metzler, Nicolas Lozano, Allison Miller, Nick Narduzzo, Grady Robertson, Seth Thomas, Elizabeth Smith (undergraduate students). Special callout to Miguel Manning for getting GPS coordinates for all the points in the Salem Cemetery. Data doesn't acquire itself, and you built the datasets for this research.

I am thankful for the hours put in by Brad Coffman to write the python code that visualized the ERT data and by Laura Everett to both host an ArcGIS workshop as well as create problem specific tutorials. Data also doesn't visualize itself, and you two made the ERT time-lapse and interactive ArcGIS map possible.

I am thankful for the two superintendents of the Texas A&M University Farm Services, Al Nelson and Stephen Labar, for access to, insightful knowledge about, and

occasional rescue from the Texas A&M Research Farm site. I am also thankful for Sherry Frisk and Ron Schaefer as well as Stacy Callihan for access to and insightful knowledge about the Salem and Old Danville-Shepherd Hill Cemeteries, respectively.

I am very thankful for my father and mother, Jeff and Rebecca Martin, for their genuine love of me, good data, and precise answers. I am also thankful for my grandparents, Rich and Margaret Dutch, who let me spend umpteen undisturbed hours in their house writing this dissertation.

I am immensely grateful for my brothers and sisters in Nehemiah, especially my mentor Pat Wells. It has been a joy to learn how to live in fellowship with all of you and with our Redeemer.

I am especially grateful for my wife, Mandy, and for her wonderful love and steadfast encouragement. It is a delight to be your husband.

CONTRIBUTORS AND FUNDING SOURCES

Contributors

This work was supported by a dissertation committee consisting of advisor Prof. Mark E. Everett, Prof. Peter S. K. Knappett, and Prof. Ryan C. Ewing, of the Department of Geology and Geophysics, and Prof. Binayak P. Mohanty of the Department of Biological and Agricultural Engineering.

The Texas Water Observatory provided the driller's log data for several monitoring wells at the Texas A&M Research Farm used in Chapters 2 and 3 as well as supported the Texas A&M Research Farm site and managed a data repository. Prof. Peter S. K. Knappett provided the groundwater data used in Chapters 2 and 3.

Figs. 4-1C, 4-3A, and 4-7A of Salem Cemetery are based upon a plan created by B. Baaske (drafting) and A. Billingsley (terrestrial laser scanning) for the Centre for Heritage Conservation at Texas A&M University. Used with permission. Figs. 4-1D, 4-3B, and 4-7B of the Old Danville-Shepherd Hill Cemetery are based upon a plan created by Texas Professional Surveying LLC. Used with permission.

All other work conducted for the dissertation was completed by the student independently.

Funding Sources

The work was funded in part by the U.S. Geological Survey, U.S. Department of Energy, under Subaward Number 06-505264-01007-M1903160 handled by the Texas

Water Research Institute. The views and opinions of authors expressed herein do not necessarily state or reflect those of the United States Government or any agency thereof.

The work was funded in part by the Patricia and George Morgan ’48 Endowed Fellowship as well as the Michel T. Halbouty ’30 Graduate Fellowship in Geology from the Department of Geology and Geophysics at Texas A&M University.

The work was funded in part by a Graduate Teaching Assistantship and by a Graduate Assistant Lectureship from the Department of Geology and Geophysics at Texas A&M University.

TABLE OF CONTENTS

Page

LIST OF FIGURES

Page

1. INTRODUCTION

Rapidly acquired non-invasive geophysical data is key to reducing the risk inherent in subsurface investigations by provision of spatiotemporally dense datasets and new methods to measure the efficacy of acquisition, analysis, modeling and interpretation. My dissertation illustrates this concept in two separate studies.

The first study uses electrical resistivity tomography and time-domain electromagnetics, including time-lapse measurements, to investigate the sedimentary architecture of an alluvial floodplain aquifer and its hydrologic communication with the adjacent river at human and geologic time scales. The second study uses ground-penetrating radar to demonstrate how identification of unmarked graves in a historic African-American cemetery can be improved using radar signatures of nearby known targets as ground-truth proxy.

1.1. Groundwater Study

Sustainable management of natural resources including soil, water, air, and minerals has become increasingly necessary in an era of world population growth especially in cities and urbanizing corridors (Muralikrishna and Manickam, 2017; Megdal, 2018). As populations use ever more fresh groundwater, sustainable management is critical to ensure its availability for future generations. Groundwater has become a focal point of international concern, with many regional and global studies investigating hydrological aspects such as capacities, recharges, and discharges of Earth's aquifers (Karim and Sadat, 2021; Ouyang et al., 2021) and policy aspects such as

accessibility and governance (e.g. Alley et al., 1999; Dalin, 2021; Lee et al., 2022; Megdal, 2018; Sanchez et al., 2021).

Whether considered on the global scale of the hydrosphere or on the scale of a shallow aquifer, several questions must be addressed to develop sustainable groundwater management strategies:

1) What is the current state of the groundwater system?
2) What is the desired state of the groundwater system?
3) Is the current trajectory likely to result in the desired state?
4) What changes, if any, can be made to the current state to result in the desired state?
5) What resources are needed to make those changes?

Addressing these questions requires acquisition of data mainly in hydrology and geology but also pedology, ecology, biology, etc. Such data form the basis for describing the current state of a groundwater system. Local stakeholders responding to a multitude of external factors determine the shape of the desired state. Modeling, the application of physical laws to an idealization of the current state, enables forecasting the trajectory of a groundwater system to a future state, with feedback directing progress toward the desired state.

Hydrogeological models serve as a scientific basis for groundwater management decisions (TWDB, 2017; Clark et al., 2011). In jurisdictions where water is considered a public resource regulated by the state, decisions can become law. It is therefore important to limit and measure risks associated with hydrogeological modeling. This

requires an improved understanding of how physical laws apply to particular settings over different time periods.

Alluvial floodplains—an important locus of world population growth—comprise a 'labyrinthine' hydrogeologic setting (Martinius, 2000; Hajek et al. 2010; Jerolmack and Paola 2007; Mackey and Bridge 1995; Nichols and Fisher 2007). Rivers meandering across alluvial floodplains periodically breach their banks to deposit mini-deltas of alluvium called crevasse splays, flood the surrounding plain, and avulse by cutting new river channels. The combination of these and other related processes steadily aggrade the floodplain. The resulting hydrogeologic architecture of the alluvial floodplain is complex and largely unknown (Mariethoz et al. 2009). Sparsely placed boreholes are inadequate to characterize floodplain architecture.

To resolve vertically and laterally complex geological structures of floodplains, an additional source of data is required, one that is dense enough to capture strong heterogeneity and be acquired rapidly enough to observe changing hydrologic conditions (Linde 2014; Linde et al. 2015). Geophysics is a collection of non-invasive proximal sensing methods that use seismic, electromagnetic, electrical, magnetic, gravitational and other physical principles to image the subsurface. Using borehole and traditional datasets as constraints, geophysicists densely interrogate the subsurface to characterize structure and monitor changing conditions.

The first contribution of this dissertation is a new, geophysics-based understanding of the hydrodynamics involved in the recharge and discharge of an alluvial floodplain aquifer of complex architecture. A bidirectional preferential flow

pathway is found between the river and adjacent aquifer that is active at both the human and geologic time scales.

1.2. Unmarked Graves Study

Unmarked graves are important for studies of cultural heritage and for site characterization prior to construction, but their reliable detection is extremely challenging (Dick et al. 2017). Traditional searches for unmarked graves are based on methods such as historical records, anecdotes and eyewitness accounts of burials, visual or remotely sensed observations of ground disturbance and subsidence, and/or probing with rods. Graves of various burial styles are found worldwide in a variety of soils in different climates, with or without headstones or other markers. If burial sites are neglected, they can become vandalized, overgrown with vegetation or built upon.

Of several applicable geophysical techniques, ground-penetrating radar (GPR) is perhaps the most widely used to achieve non-invasive proximal sensing of unmarked graves. Currently however there is no widely-accepted standard protocol for finding unmarked graves using GPR or any other geophysical technology (WSP 2018). As GPR targets, unmarked graves are difficult to detect since different burial styles produce different radar signatures, signal penetration is variably effective depending on soil type and moisture content, and over time the signatures of burials fade into the background owing to natural decomposition and soil consolidation processes. Geophysicists are faced with the task of discerning an unknown signal in the midst of unknown noise, and even detailed 3-D numerical modeling of the Maxwell equations governing

electromagnetic wave propagation (Warren et al. 2016) is seldom helpful except to understand the signatures of highly idealized scenarios.

Unmarked graves comprise one of several classes of subsurface targets that have been investigated using GPR in recent years. There is a large literature on GPR sensing of buried utilities such as cables and pipelines. An even larger literature exists for studies of landmine detection, discrimination and classification. Detection is the process of determining the existence of a subsurface object, and discrimination involves making a distinction between a target of interest and uninteresting "clutter", while classification is the determination of target-of-interest properties such as burial depth, size, orientation, etc. In many cemeteries, tree roots are the primary source of clutter. A closely related body of literature involves studies on sensing unexploded ordnance (UXO) using metal detectors based on electromagnetic induction (EMI) principles.

Medical imaging has developed protocols for optimizing the recognition or diagnosis of targets of interest such as tumors or other abnormalities. The concept of receiver operating characteristics (ROC) analysis is described in the landmark review paper of Metz (1978). ROC analysis suggests an interpretation protocol based on training on known examples such that the number of false alarms and missed diagnoses from a set of unknown examples is minimized. Extensions of ROC analysis have been applied in several areas of geophysics, most notably in GPR sensing of landmines (e.g. Lee et al. 2007; Frigui et al. 2010) and EMI sensing of UXO (e.g. Bijamov et al. 2014).

The second contribution of this dissertation is the development of a protocol inspired by previous medical and geophysical ROC analyses to improve GPR

identification of unmarked graves in a historic African-American cemetery. I show that a geophysicist's proficiency, expressed in terms of true-positive, true-negative, false-positive, and false-negative percentages, can be improved using radar signatures of nearby known targets such as marked graves and tree roots as ground-truth proxy.

As a final note on this research: the change in topics from alluvial aquifers in Chapters 2 and 3 to unmarked graves in Chapter 4 was due to the limitations imposed by the COVID-19 pandemic.

1.3. References

Alley, W.M., Reilly, T.E., and Franke, O.L. (1999) *Sustainability of ground-water resources*, U.S. Dept. of the Interior, U.S. Geological Survey ; U.S. G.P.O. ; U.S. Geological Survey, Branch of Information Services [distributor, Denver, CO; [Washington, D.C.]; Denver, CO.

Bijamov, A., J.P. Fernandez, B.E. Barrowes, I. Shamatava, K. O'Neill and F. Shubitidze. (2014) Camp Butner live-site UXO classification using hierarchical clustering and Gaussian mixture modeling, *IEEE Trans. Gesoci. Remote Sens.* **52**, 5218-5229.

Clark, B.R., Hart, R.M., and Gurdak, J.J., (2011) Groundwater availability of the Mississippi embayment. *U.S. Geological Survey Professional Paper 1785*.

Dalin, C. (2021) Chapter 25 - Sustainability of groundwater used in agricultural production and trade worldwide, in *Global Groundwater* (eds. Mukherjee, A., Scanlon, B.R., Aureli, A., Langan, S., Guo, H., and McKenzie, A.A.), Elsevier, pp. 347–357.

Dick, H.C., J.K. Pringle, K.D. Wisniewski, J. Goodwin, R. van der Putten, G.T. Evans, J.D. Francis, J.P. Cassella and J.D. Hansen. (2017) Determining geophysical responses from burials in graveyards and cemeteries, *Geophysics* **82**, B245-B255.

Frigui, H., L.J. Zhang and P.D. Gader. (2010) Context-dependent multisensor fusion and its application to land mine detection, *IEEE Trans. Geosci. Remote Sens.* **48**, 2528—2543.

Hajek E. A., Heller P. L. and Sheets B. A. (2010) Significance of channel-belt clustering in alluvial basins. Geology, 38(6), 535-538.

Jerolmack D. J. and Paola C. (2007) Complexity in a cellular model of river avulsion. Geomorphology, Special Issue 91(3-4), 259-270.

Karim, A.Q., and Sadat, S.H. (2021) Chapter 23 - Groundwater of Afghanistan (potential capacity, scarcity, security issues, and solutions), in *Global Groundwater* (eds.Mukherjee, A., Scanlon, B.R., Aureli, A., Langan, S., Guo, H., and McKenzie, A.A.), Elsevier, pp. 323–328.

Lee, K., Chang, S., Koop, S., van Leeuwen, K., and Park, J. (2022) Enhancing Informed Decisions for Coastal Groundwater Sustainability: A Network Analysis of Water-Related Indicator Results from 122 Cities. *Water*, **14** (2), 262.

Lee, W.H., P.D. Gader and J.N. Wilson. (2007) Optimizing the area under a receiver operating characteristic curve with application to landmine detection, *IEEE Trans. Geosci. Remote Sens.* **45**, 389—400.

Linde N. (2014) Falsification and corroboration of conceptual hydrological models using geophysical data. Wiley Interdisciplinary Reviews - Water, 1(2) 151-171.

Linde N., Renard P., Mukerji T. and Caers J. (2015) Geological realism in hydrogeological and geophysical inverse modelling: a review. Advances in Water Resources, 86(A), 86-101.

Mackey S. D. and Bridge J. S. (1995) Three-dimensional model of alluvial stratigraphy: theory and applications. Journal of Sedimentary Research, B65(1), 7-31.

Mariethoz G., Renard P., Cornator F. and Jaquet O. (2009) Truncated plurigassian simulations to characterize aquifer heterogeneity. Groundwater, 47(1), 13-24.

Martinius A. W. (2000) Labyrinthine facies architecture of the Tortola fluvial system and controls on deposition (Late Oligocene - Early Miocene, Loranca Basin, Spain). Journal of Sedimentary Rock, 70(4), 850-867.

Megdal, S.B. (2018) Invisible water: the importance of good groundwater governance and management. *npj Clean Water*, **1** (1), 1–5.

Metz, C.E. (1978) Basic principles of ROC analysis, *Sem. Nucl. Medicine* **8**, 283—298.

Muralikrishna, I.V., and Manickam, V. (2017) Chapter Three - Natural Resource Management and Biodiversity Conservation, in *Environmental Management* (eds.Muralikrishna, I.V., and Manickam, V.), Butterworth-Heinemann, pp. 23–35.

Nichols G. J. and Fisher J. A. (2007) Processes, facies, and architecture of fluvial distributary system deposits. Sedimentary Geology, Special Issue 195(1-2), 75-90.

Ouyang, Y., Wan, Y., Jin, W., Leininger, T.D., Feng, G., and Han, Y. (2021) Impact of climate change on groundwater resource in a region with a fast depletion rate: the Mississippi Embayment. *Journal of Water and Climate Change*, **12** (6), 2245–2255.

Sanchez, R., Breña-Naranjo, J.A., Rivera, A., Hanson, R.T., Hernández-Espriú, A., Hogeboom, R.J., Milman, A., Benavides, J.A., Pedrozo-Acuña, A., Soriano-Monzalvo, J.C., Megdal, S.B., Eckstein, G., and Rodriguez, L. (2021) Binational reflections on pathways to groundwater security in the Mexico–United States borderlands. *Water International*, **46** (7–8), 1017–1036.

Texas Water Development Board (TWDB). (2017) Groundwater availability model for the Brazos River Alluvium. INTERA Inc.

Warren, C., A. Giannopoulos, and I. Giannakis. (2016) “gprMax: Open source software to simulate electromagnetic wave propagation for ground penetrating radar,” Comput. Phys. Commun. 209, 163–170.

WSP Inc. and New South Assoc. Inc. (2018) Practical guide for developing effective scopes of work for the geophysical investigation of cemeteries, NCHRP Project 25-25, Task 98, 306pp.

2. COUPLING HYDROGEOPHYSICS WITH HYDRODYNAMIC MODELLING TO INFER SUBSURFACE HYDRAULIC ARCHITECTURE OF AN ALLUVIAL FLOODPLAIN*

2.1. Introduction

Sustainable management of shallow aquifers requires understanding their geometry and interactions with other bodies of water (Castagna et al. 2015). The interactions may be vertical—e.g. rainwater or floodwater infiltrating the variably-saturated (vadose) zone —or lateral—e.g. stream water infiltrating into, or exfiltrating out of the aquifer through its banks. Modelling the relevant hydrodynamics is vital for predicting potential future states of aquifers, in terms of water quality and quantity. These are inter-woven and are commonly driven by factors such as contaminant transport from land surface to aquifers or from rivers to aquifers, prolonged drought, over-pumping, or aquifer replenishment. Understanding the processes that drive the timing, direction and magnitude of surface-to-subsurface volumetric fluxes allows for better management of groundwater resources.

However, modelling volumetric fluxes is a complex problem within the floodplains of meandering rivers, owing to geologic heterogeneity. This heterogeneity is driven by periodic, major flooding of floodplains that can change a river's course,

* This section is reprinted, with permission, from Martin, J.M., Everett, M.E., and Knappett, P.S.K. (2021) Coupling hydrogeophysics with hydrodynamic modelling to infer subsurface hydraulic architecture of an alluvial floodplain. *Near Surf. Geophys.*, **19** (3), 335–352.

typically leaving behind an abandoned river channel filled with a heterogeneous mixture of sediments (Cattaneo and Steed 2003; Martinius 2000; Wright and Marriott 1993). The preserved, buried geologic structure is termed herein a channel-belt. Repeated flooding creates additional channel-belts and eventually can result in a floodplain characterized by anastomosing channel-belts. In such floodplains, lateral continuity of sedimentary layers or the water table cannot be assumed.

The lack of lateral continuity in a meandering-river floodplain limits the information value of widely spaced boreholes because they cannot resolve the laterally complex geological structure between them. An additional source of data is needed, which can be provided by geophysical surveys (Linde 2014; Linde et al. 2015). One such example of a meandering-river floodplain lacking lateral continuity is the Brazos River alluvial floodplain which runs southeast through Texas (see Figure 1). Rhodes et al. (2017) discovered that the Brazos floodplain aquifer water table remained persistently higher (several m) than the river stage along a nearby 24 km stretch over an approximately one-year time period. Whereas this would be expected if the river was gaining groundwater from the aquifer, no measurable discharge into the river occurred during the dry season when maximum differences in hydraulic head (>3 m) were observed between the aquifer and the river. To explain these observations, Rhodes et al. (2017) suggested that a subsurface, clay-dominated channel-belt (i.e. lateral discontinuity) prevents groundwater from flowing from the aquifer into the river.

In this paper we take the idea of a hydraulically-isolated aquifer as proposed by Rhodes et al. (2017), use geophysics—2-D electrical resistivity tomography (ERT) and

1-D time-domain electromagnetics (TEM)—to explore the subsurface sedimentary structures that result in this isolation at our field site, and then use modelling to explore how such an aquifer would recharge after being over-pumped if recharge could not come from nearby bodies of water like a river. Although some model details are specific to the Brazos site, we model a useful idealization of the aquifer so that the general principles of the hydrodynamic response should be applicable to other alluvial floodplains with a similar channel-belt geometry. This research fits into broader efforts to understand near-surface controls on the characteristics and behaviour of aquifers in alluvial floodplains under extreme flooding events, especially pertaining to sustainable management of ecosystems, agricultural resources, and mitigation of flood inundation hazards (especially in urbanizing corridors).

2.1.1. Alluvial Floodplains: Geological Characterization

River avulsions aggradate sediment in alluvial floodplains (Cattaneo and Steed 2003; Wright and Marriott 1993) and incise new channel-belts (Blum et al. 2013). Avulsions are controlled by the streambed gradient, which is itself controlled by factors such as climate (Amorosi et al. 2008; Blum and Tornqvist 2000; Maddy et al. 2001) and tectonics (Holbrook and Schumm 1999). While these global controls drive avulsions affecting the entire floodplain, local controls (e.g. sediment supply, water supply, and topography) drive smaller-scale avulsions by gradually producing widening meanders, cut-throughs, and isolated oxbow lakes. Smaller avulsions often reoccupy and stack upon pre-existing, sand-dominated channel-belts (Bryant et al. 1995; Mohrig 2000). Stacking of small-scale and large-scale avulsions results in strong, multi-scale geological

heterogeneity (Slingerland and Smith 2004) on scales of 100-101 m (Zaleha 1997). Martinius (2000) summarizes the heterogeneity as 'labyrinthine', a characterization supported by others (Hajek et al. 2010; Jerolmack and Paola 2007; Mackey and Bridge 1995; Nichols and Fisher 2007). Thus, we cannot determine the shape or composition of the channel-belt suggested by Rhodes et al. (2017) simply from examination of the present-day topography. Indeed, the full complexity of younger, not yet fully-buried channel-belts is only hinted at in the topography southwest of the modern Brazos River shown in Figure 1.

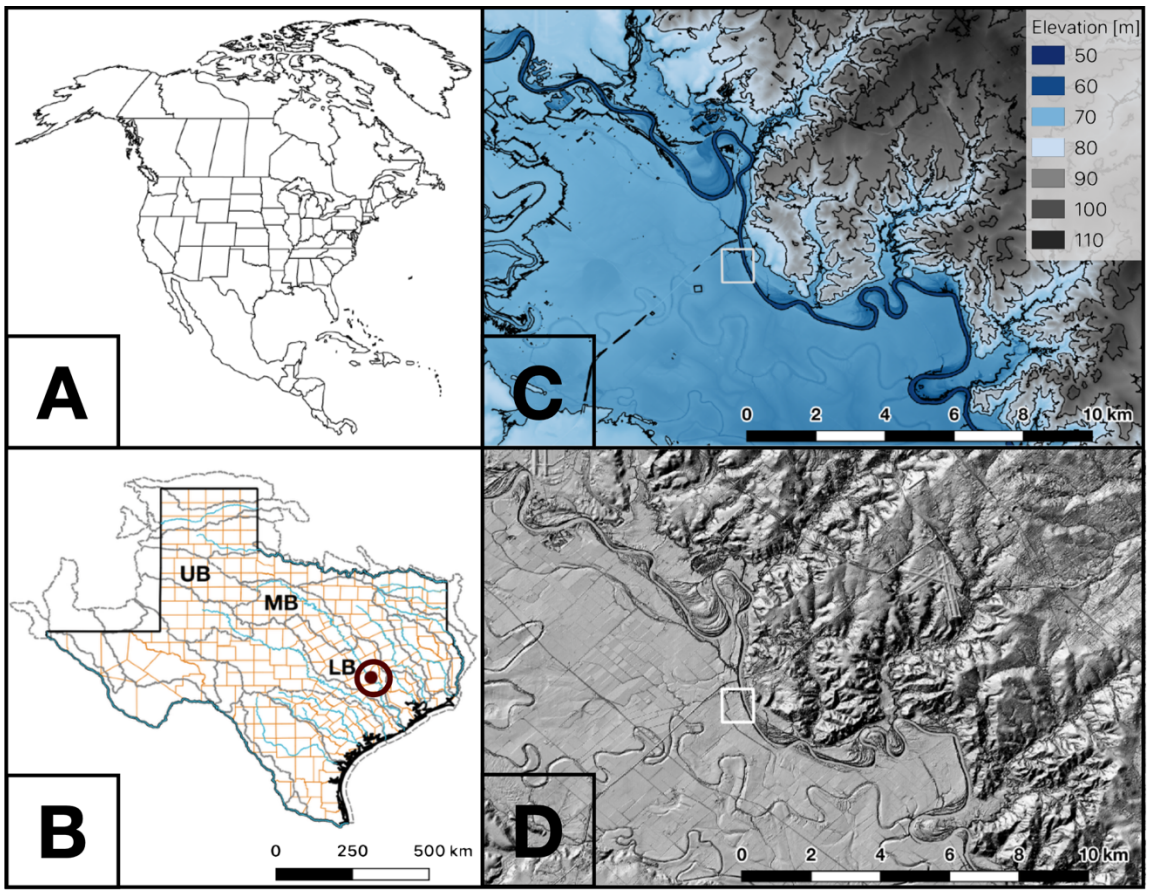

Figure 2.1. Context for field site; north toward the top. A North America. B Texas. County outlines in orange; major rivers in blue; watersheds in dotted grey (UB/MB/LB =

Upper/Middle/Lower Brazos). Field site (bullseye) is in Burleson County adjacent to the Brazos River in the Lower Brazos Watershed. C Topography of the Brazos River floodplain (dark to very pale blue) in lower left half around the Brazos River (dark blue); adjacent highlands (light to dark grey) in upper right half. D Hillshade view of the Brazos River floodplain in lower left half; adjacent highlands in upper right half containing the city of College Station, TX. Field site (white square) southeast of northeast-southwest trending US HW60. Topography rendered from 2017 USGS lidar data at 70 cm horizontal resolution.

As river avulsions control the geometry and composition of the channel-belts, the resulting preferential zones specify the connectivity between surface streamflow, surface sheetflow, and subsurface groundwater flow (Frei et al. 2009) and shape the responses to vertical and lateral hydraulic disturbances. The connectivity of preferential flow zones depends on the largely unknown, heterogeneous distribution of hydrofacies with the floodplain (Mariethoz et al. 2009) on the 100-101 m scale. The geometry or composition of the proposed channel-belt, and its enclosing hydrofacies, cannot be obtained simply by spatially interpolating information from outcrops or boreholes (Rhodes et al. 2017; Savoy et al. 2017; Zhang et al. 2013), which are typically separated by scales of 102-103 m. At Brazos, the separation of wells is ~103 m (see Figure 2).

2.1.2. Alluvial Floodplains: Geophysical Characterization

Many authors consider geophysics to be a reliable means to fill the information gap between boreholes and outcrops (e.g. He et al. 2014; Hoyer et al. 2017; Gottschalk et al. 2017; Gueting et al. 2015; Shuai et al. 2017). Geophysical techniques are largely non-invasive and less expensive than traditional geomorphological and hydrological methods, and – unlike the 1-D profiles obtained from borehole data – geophysical data can characterize 2-D and 3-D heterogeneities within large, spatially contiguous volumes

of the subsurface (Perri et al. 2012). Several studies have confirmed that electrical resistivity tomography (ERT)—which can probe lateral distances of 102-103 m and vertical distances of 100-102 m—is a reliable method for hydrological characterization of shallow subsurface structure including infiltration pathways (Binley and Beven 2003; Borner et al. 1996; Boucher et al. 2009; Chambers et al. 2010; Oldenborger et al. 2007). ERT has also become a robust method for delineating channel-belts in alluvial floodplains (Babek et al. 2018; Grygar et al. 2016; Kolker et al. 2013; Mastrocicco et al. 2010). Due to its ease of use and the availability of robust inversion software (e.g. Loke 1999; AGI EarthImager available from agiusa.com), ERT has become widely used. However, despite the utility of ERT as a stand-alone geophysical technique, the interpretation of ERT data is enhanced by adding complementary geophysical information, such as time-domain electromagnetics (TEM)—which can probe vertical distances up to 102-103 m (Ezersky et al. 2011; Gomez et al. 2019). In this study, ERT is employed as the primary geophysical means for imaging the suspected channel-belt while TEM provides validation of the ERT results.

2.2. Geological Setting

The field site is an 18-ha (0.18 km^2) portion of the 600-ha (6.0 km^2) Texas A&M University Research Farm (see Figure 2) in eastern Burleson County, Texas. Geographically, the farm lies near the southern margin of the humid-subtropical North American Great Plains physiographic province. Burleson County lies within a sub-tropical, sub-humid region of “mixed prairie, savanna, and woodlands” known as the

Post Oak Savanna (Texas Water Development Board 2012). To the east and south lie, respectively, the very humid, sub-tropical "evergreen-deciduous forestland" (the Piney Woods) and "marine prairies and marshes" (the Gulf Coastal Plains).

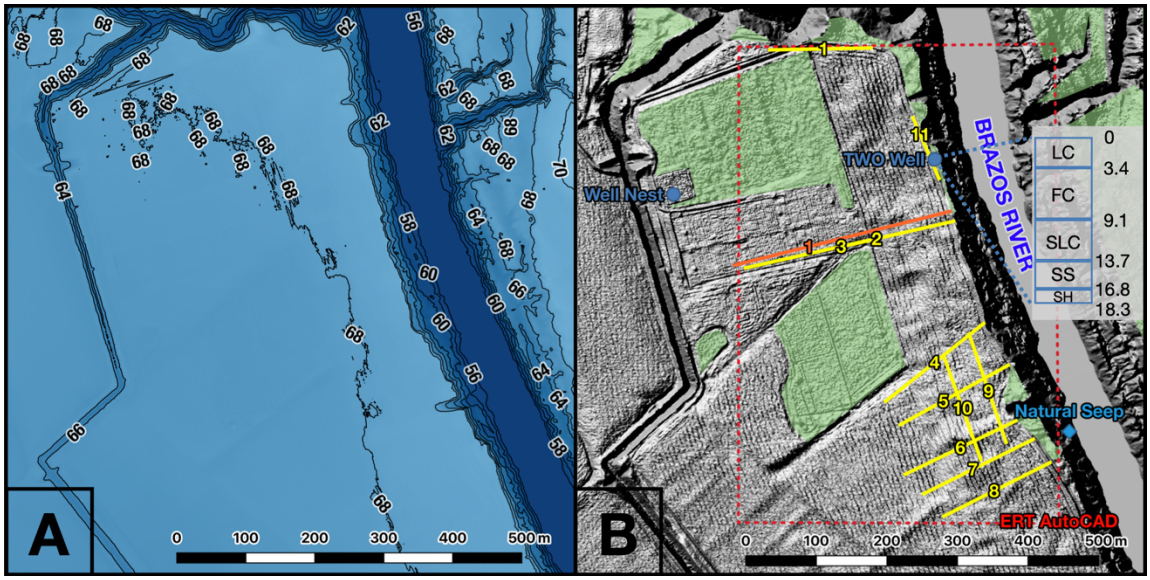

Figure 2.2. North-eastern section of the Texas A&M Research Farm on the western bank of the Brazos River (running from upper center to lower right corner) in Burleson County, TX. Rendered from 2017 USGS lidar data at 70 cm horizontal resolution. A Topographic map of the Farm. Brazos River at ~56 masl; agricultural fields on the western bank at ~68 masl. B Hillshade view of the Farm. 2D ERT lines (yellow) are 177.6 m long; TEM line (orange) is 300 m long composed of 31 soundings at a 10 m spacing; blue dots indicate the location of the well nest used by Rhodes et al. (2017) and the Texas Water Observatory (TWO) well and drilling log (depths in meters); LC = lean clay; FC = fat clay; SLC = sandy lean clay; SS = silty sand; SH = shale); a natural seep; forested areas (green); outline of the ERT fence diagram in Figure 5.

Hydrologically, the site is located along the perennial Lower Brazos River within the Brazos River watershed which drains into the Gulf of Mexico; major river avulsions have occurred in this watershed every ~2.5 ka (Taha & Anderson 2008). Pedologically, the prevailing Weswood-Coarsewood soils are moderately permeable, calcareous and

loamy. Geologically, the strata include Holocene/Pleistocene alluvium at the surface, underlain by Eocene shale at ~30 m depth.

The eastern side of the site is bounded by a steeply sloughing bluff overlooking the Brazos River (at the time of the geophysical surveys, the river stage was ~12 m below the floodplain); this bluff contains several natural seeps. At the top of the bluff is a monitoring well drilled by TWO in fall 2018. The lithology in that well (Figure 2B, units [m]) generally agrees with the pattern of clay, sand, gravel with increasing depth which was observed during the installation of 9 on-site vertical piezometer nests (Figure 2B, the 'Well Nest') described in Wrobleski (1996). Groundwater and river water resistivities were measured with a handheld probe as 9.1 and 15 Ωm, respectively. Due to this narrow range, we agree with Rhodes' et al. (2017) that, "…the differences in resistivity of the rocks and sediments [are] likely driven by the greatly contrasting resistivities of the predominant geology in the area…"

Our use of ERT, TEM, and hydrodynamic modelling was cooperative. The results of each ERT survey line helped determine the location of the next, the TEM was used primarily to validate the ERT results, and the combined geophysical results informed hydrodynamic modelling to study subsurface hydrodynamic interactions of the alluvial floodplain.

2.3. Methods

2.3.1. Electrical Resistivity Tomography

Electrical resistivity tomography is the primary geophysical method used in this study. To achieve the required lateral and vertical resolution, we used the dipole-dipole

configuration (Furman et al. 2003; Zonge et al. 2005) shown in Figure 3A. By measuring voltage, and knowing the current and electrode locations, the apparent resistivity for the four-electrode system is found using the equations:

$$\rho_a = \kappa Z \tag{1}$$

$$\kappa = \pi n(n+1)(n+2)a \tag{2}$$

$$Z = \frac{V_{PQ}}{I} \tag{3}$$

where ρ_a [Ωm] is apparent resistivity, κ is the geometric array factor, Z [Ω] is electrical impedance, n is the multiplier for the distance between electrode pairs, a [m] is the distance between the source/sink and potential electrodes, V_{PQ} [V] is the recorded voltage between electrodes P and Q, and I [A] is the injected current. The measured apparent resistivities are then assembled into a trapezoidal cross-section known as a pseudosection (Figure 3E). It is so-called because it is not a true section of the bulk resistivity distribution with depth, but rather a matrix displaying apparent resistivity versus electrode spacings; any value of apparent resistivity located therein would be the true resistivity only in the idealized case in which the volume of Earth probed by the four electrodes is spatially uniform.

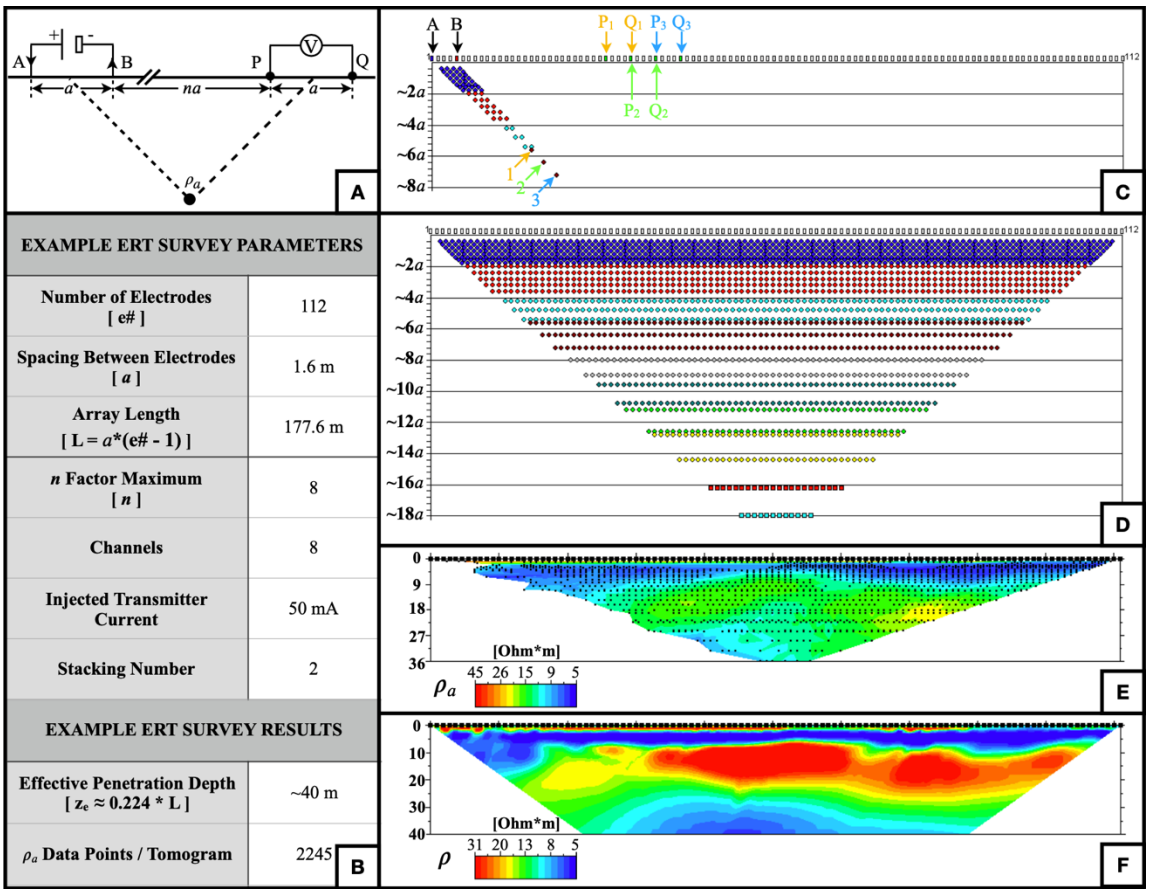

EXAMPLE ERT SURVEY PARAMETERS	
Number of Electrodes [e#]	112
Spacing Between Electrodes [*a*]	1.6 m
Array Length [L = *a**(e# - 1)]	177.6 m
n Factor Maximum [*n*]	8
Channels	8
Injected Transmitter Current	50 mA
Stacking Number	2
EXAMPLE ERT SURVEY RESULTS	
Effective Penetration Depth [$z_e \approx 0.224 * L$]	~40 m
ρ_a Data Points / Tomogram	2245

Figure 2.3. Theory and parameters of electrical resistivity tomography (ERT). A Basic dipole-dipole configuration: a = distance between current or voltage electrodes, n = multiplier of distance between electrode pairs A,B and P,Q, and ρa = apparent electrical resistivity. B Example parameter and result values. C Example of 3 simultaneous measurements. D Estimated spatial distribution of total number of apparent resistivity measurements. E Pseudosection of apparent resistivities with noisy (i.e. difference between the two stacked measurements at a single point is greater than 5%) data points removed. F Final, interpretable inverted tomogram.

The process described above provides the input data for the inverse method, i.e. the conversion of the apparent resistivity pseudosection into a resistivity image of the Earth (Figure 3F). A forward calculation is performed to obtain the computed

pseudosection for a given resistivity model. This is done, for each member of the sequence of current injection/withdrawals, by solving the Laplace forward equation that governs the spatial distribution of electric potential. We used the finite difference forward solver in the AGI Earth Imager software.

The EarthImager tomographic reconstruction algorithm, based on damped least squares, is used to minimize the difference between the measured and computed pseudosections. The algorithm iteratively adjusts the Earth resistivity model to achieve a good match between its response and the observed data. A smoothness constraint is enforced throughout the process to improve the stability of the reconstruction. The 2-D results are visualized as a trapezoidal cross-section of actual resistivities (Figure 3F), or tomogram. While ready for hydrogeological interpretation, care must be taken because the 2-D tomogram is technically the spatial average of a 3-D structure within a few meters on either side of the tomogram "projected" onto the 2-D vertical plane beneath the electrode array. Provided the 2-D tomograms vary only modestly from line to line, the 2-D approach should be sufficient to accurately characterize the actual 3-D subsurface.

To visualize the tomograms using a pseudo-3D display, the ERT tomograms are converted from raster to vector format using Scan2CAD, a software package typically used for vectorizing architectural diagrams. We then assembled the resulting georeferenced vector files and superimposed them on a vectorized map of the field site in AutoCAD.

It is important to understand the influence of acquisition parameters in an ERT survey. Regarding Figure 3B, the first four parameters ultimately determine both the effective penetration depth ze of the survey (Edwards 1977), and the total number of subsurface points at which apparent resistivity is measured. The "n Factor Maximum" parameter value of n = 8 is higher than often used (e.g. n = 6). As described below, the maximum electrical resistivity at the Brazos site is ~200 Ωm, i.e. the loamy soils and clay-rich alluvium at our site are relatively good conductors. These soils permit excellent coupling between the electrodes and the ground, yielding a good signal-to-noise ratio despite the high n Factor Maximum. The other three parameters—channels, injected transmitter current, and stacking number—respectively determine how many voltage measurements can be made simultaneously and therefore the speed of data acquisition, the strength of voltage signal, and number of repetitions of each measurement.

2.3.2. Time-Domain Electromagnetics

We employed the TEM method (Everett and Meju 2005) to complement the data acquired with ERT. To validate the subsurface electrical resistivity structures from the ERT tomograms prior to hydrodynamic modelling, we used a mobile central-loop sounding configuration (Everett 2013). The field setup consists of a 1-m radius receiver coil (RX) located in the centre of a 10 m x 10 m square transmitter loop (TX). When current flows through the TX, a transient primary magnetic field $\mathbf{B}^{P}(\mathbf{r}, t)$ is created. When the current is cut off, the associated electromotive force induces eddy currents to flow in the conductive subsurface (Figure 4A). The eddy currents, as they vanish with time, generate a transient secondary magnetic field $\mathbf{B}^{S}(\mathbf{r}, t)$, some of whose magnetic

field lines flux through the RX coil. Abruptly shutting off the electric current passing through the TX loop removes (after a time as short as possible) the $\mathbf{B}^{P}(\mathbf{r}, t)$ (Figure 4C), leaving only the decaying $\mathbf{B}^{S}(\mathbf{r}, t)$ to induce a small decaying voltage (during C, C' in Figure 4C and measured in Figure 4D). In a homogeneous half-space, the RX-voltage decay curve follows a predictable shape (Fitterman 2015). Departures from this shape indicate the presence of heterogeneity, such as layering or lateral variations in subsurface electrical conductivity. The observed decaying RX voltage is inverted using the IXG-TEM software (Interpex Limited 2012) to obtain a 1-D depth profile of the subsurface. Time decay and conductivity are related to RX voltage via the following expression (Spies 1989):

$$V^{l} = \frac{I\sigma^{\frac{3}{2}}\mu_0^{\frac{5}{2}}a^2}{30\pi^{\frac{1}{2}}t^{\frac{5}{2}}} \tag{4}$$

where V^{l} = [V] is late time voltage, I [A] is current, σ [S/m] is electrical conductivity, μ_0 [N/A^2] is the permeability of free space, a [m^2] is area of the coil, and t [s] is time.

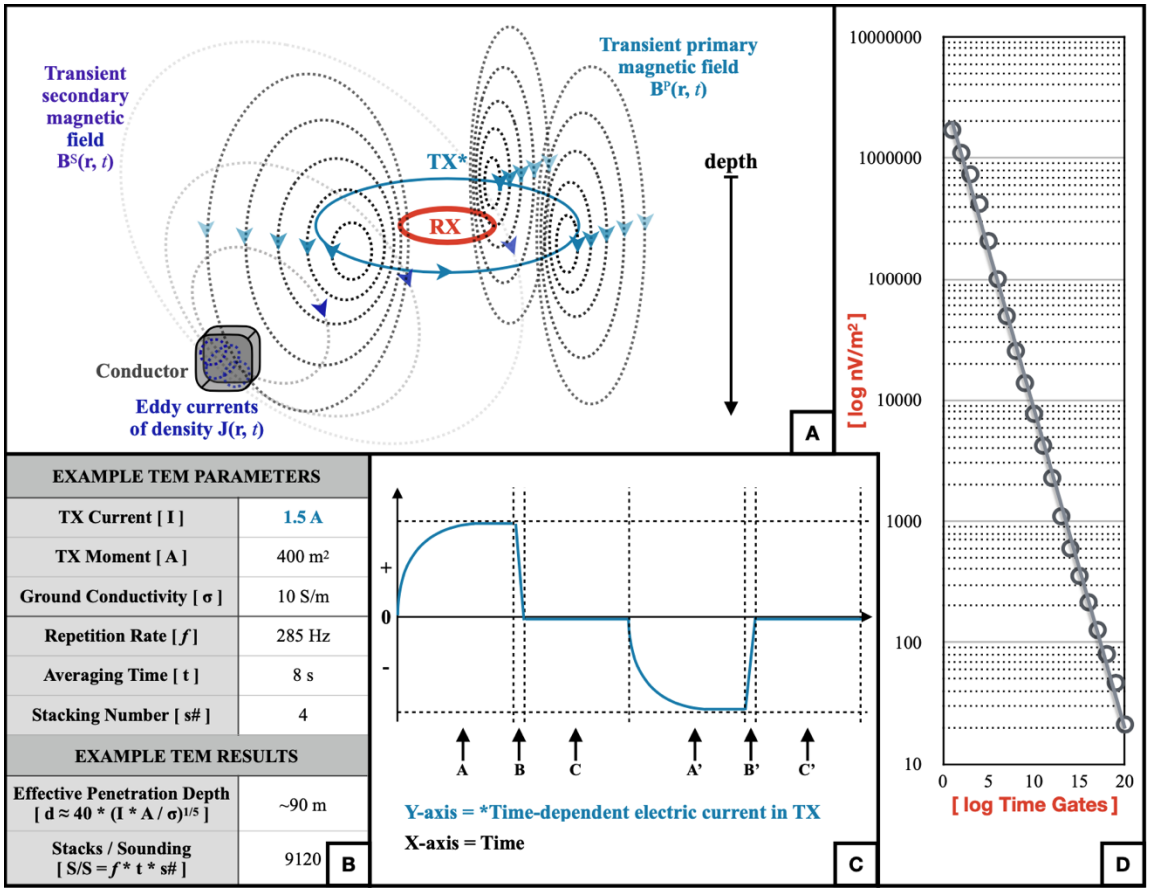

Figure 2.4. Theory and parameters of time-domain electromagnetics. A Central-loop, controlled-source, transient electromagnetic sounding, where TX = transmitter antenna, RX = receiver antenna. Only eddy currents in the conductor shown for simplicity; other eddy currents propagate into the subsurface. B Example parameter and result values. C Time-dependent electric current in TX; A, A' = time when TX current ramps to steady state value (i.e. +/-1.5 A), generating $B^P(r, t)$, and the electromotive force falls to zero toward the ends of these times; B, B' = time when TX current is switched off (~20 μs); C, C' = time when decaying BS(r, t) fluxes through and is measured by the RX coil. D Decay of $B^S(r, t)$ through RX induces decaying voltage, measured as a normalized value of the effective area of the RX coil (i.e. nV/m2). This decay is measured at specific time gates which are logarithmically spaced and have logarithmically increasing times during which they are open to repeatedly measure and average the decaying voltage; e.g. the 1st gate opens at 6.000 μs, is open for 1.625 μs, and closes at 7.625 μs; the 20th gate opens at 601.9 μs, is open for 188.1 μs, and closes at 790.0 μs.

Regarding Figure 4B, the first three parameters determine the effective penetration depth d of the survey, as discussed by Spies (1989). The TX current reaches its steady value near the end of A, A'; the TX moment is a function of the TX loop area and number of turns while ground conductivity is an uncontrollable variable. The last three parameters control the signal-to-noise ratio, which is quite good since we perform 9120 stacks per sounding. The TX-current cycle shown in Figure 4C occurs 285 times per second and the response is acquired and averaged for 8 s, and that process is replicated 4 times.

2.3.3. Hydrodynamic Modelling

We explore hydrodynamic responses of a buried sandy channel, whose geometry is similar to that inferred by the foregoing geophysical imaging, that is initially unsaturated and then the ground surface above it is covered with standing water. We employed HYDRUS-2D, a hydrological software package that simulates the movement of water, heat, and multiple solutes in variably saturated porous media (Šimůlek et al. 2012) by solving Richards' equation. The aquifer geometry was input into the model by specifying the constituent geomaterials whose unsaturated soil hydraulic parameters include: residual water content Qr, saturated water content Qs, saturated hydraulic conductivity Ks, inverse of the air-entry value (or bubbling pressure) α, pore-size distribution index n, and pore-connectivity parameter l. We used the software default values for the parameters corresponding to the various geomaterials measured and inferred to be present at the Brazos site. The geomaterials are determined by comparing the geophysical results with the TWO-well drilling log and analysis. Outputs of a

HYDRUS-2D model simulation include subsurface pressure head, groundwater velocity, and variably saturated water content.s

We did not make an explicit attempt to model the particular hydrodynamics operating at the Brazos field site at the time of the geophysical surveys. Since the geophysical results showed an intriguing geometric distribution of electrical resistivities, we constructed a useful idealization of the distribution of the likely prevailing geomaterials and consider our modelling as the simulation of a plausible hydrologic scenario, specifically one wherein the alluvial aquifer is subjected to over-pumping and then flooding conditions. These are both relevant conditions to the Brazos River cultivated alluvial floodplain.

2.4. Results

2.4.1. Electrical Resistivity Tomography

The locations of the 11 ERT tomograms acquired at the Brazos site are shown in Figure 5A. The average RMS fit is 3.78 ± 0.88% (the highest was 5.55% at ERT-10) and the tomograms contained an average of 18.91 ± 13.74% noisy data points that were excluded from the inversion. Inversion iterations were performed until the misfit was reduced below 5%. For inversion, we set the minimum and maximum resistivities at 1 and 10,000 Ωm, respectively, the smoothness and damping factors both at 10, and the resolution factor at 0.2 in accordance with the recommendations explained in the Instruction Manual for EarthImager 2D Version 2.4.0. We also set the horizontal/vertical roughness ratio at 2, which is greater than the default value of 1 because we expect to

observe significant lateral variation in alluvial floodplains in general (as explained in the Introduction) and at our site in particular (as suggested by Rhodes et al. (2017)).

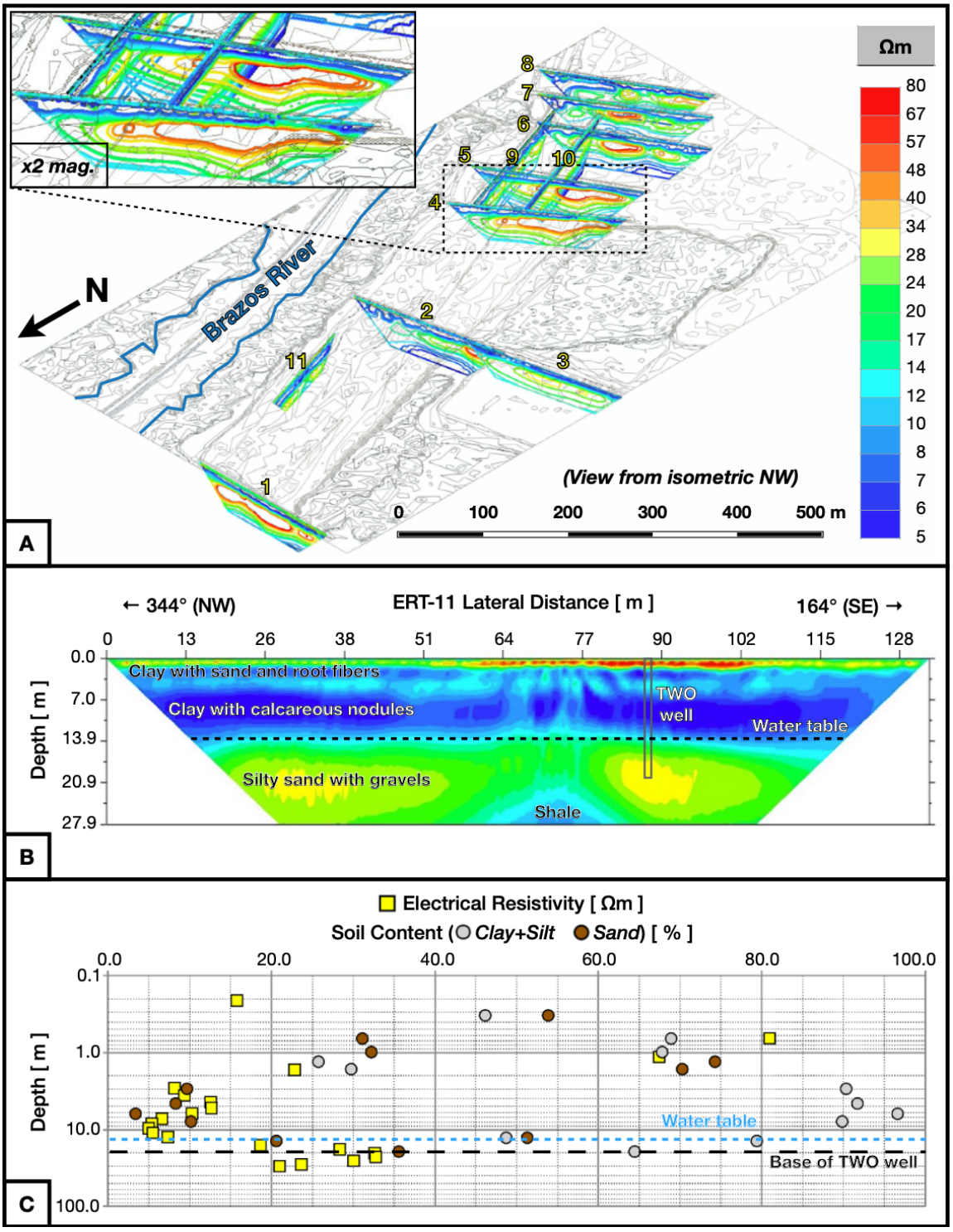
A
x2 mag.
N
Brazos River
(View from isometric NW)
0 100 200 300 400 500 m
Ωm
80
67
57
48
40
34
28
24
20
17
14
12
10
8
7
6
5
1
2
3
4
5
6
7
8
9
10
11
B
← 344° (NW)
ERT-11 Lateral Distance [m]
164° (SE) →
0 13 26 38 51 64 77 90 102 115 128
Depth [m]
0.0
7.0
13.9
20.9
27.9
Clay with sand and root fibers
Clay with calcareous nodules
Silty sand with gravels
Shale
TWO well
Water table
C
Electrical Resistivity [Ωm]
Soil Content (Clay+Silt Sand) [%]
0.0 20.0 40.0 60.0 80.0 100.0
Depth [m]
0.1
1.0
10.0
100.0
Water table
Base of TWO well

Figure 2.5. ERT results. A ERT fence diagram; 16 colours are logarithmically scaled between 5 and 80 **Ωm** due to the range of electrical resistivities encountered in ERT-11 adjacent to the TWO well. Transparent "holes" within the highest resistivity (i.e. most red) contours are regions with electrical resistivities higher than 80 Ωm. Each trapezoidal tomogram is 177.6 m long across its top. The short base of the ERT tomograms approximates geologic properties at 41 ± 2 m depth, except ERT-3 (base depth 31 ± 1 m) and ERT-11 (base depth 28 ± 1 m). Inset shown at x2 magnification. B ERT-11 adjacent to the TWO well; driller's log descriptions and the depth of the water table encountered on the day of drilling included at appropriate depths. C Depth vs. electrical resistivity (Ωm) and soil content (%); x-axis is in both Ωm and %.

The geophysical literature contains various inversion schemes that include structural constraints favouring abrupt discontinuities rather than smooth transitions in a subsurface physical property. Indeed, the AGI EarthImager software has a "blocky inversion" option that emphasizes sharp boundaries. In this paper we have elected to use the "smooth inversion" option since we found it returned sufficiently useful information about the isolated sand bodies buried in the alluvial floodplain. Moreover, the choice of whether to perform probabilistic or deterministic inversion is largely a matter of taste, since neither can overcome fundamental limitations such as non-uniqueness and the curse of dimensionality. In the end, both approaches identify Earth models with desired attributes that fit a given dataset, and both can provide a local sensitivity analysis of the inversion result. The resistivity structure in our tomograms ERT-4 to ERT-10 slowly varies from one to the next; in particular, there is good along-strike continuity between ERT-4 to ERT-8. This suggests that our 2-D approach should be sufficient to accurately characterize the subsurface at the Brazos site.

From Figure 5A, a zone comprising the highest resistivities (>33 Ωm; i.e. yellow to red) is evident which begins at ERT-1 and is of ~180 m width and ~25 m thickness.

The zone widens to ~210 m by ERT-2 and ERT-3. At least part of this high-resistivity zone veers to the SE, gradually thinning and shrinking between ERT-4 to ERT-8, although it is possible that an additional part may veer to the SW in a Y-shape where no data are available. Additional fieldwork is required to refute or corroborate the presence of the additional part.

To the east, the zone fragments into smaller, less discernible channels, see ERT-9 and ERT-10, or pinches out altogether (ERT-11). Generally, the high-resistivity zone is oriented roughly parallel to the river. Intriguingly, while the roof of the zone is sub-horizontal and sub-planar, its base is asymmetrically and varies substantially in depth (e.g. Figure 5A, insert). The river-distal sides of the zone have shallower bases than the river-proximal sides of the zone.

Also visible the Figure 5A insert is a gradual thickening of a moderately resistivity (~14-28 Ωm; i.e. green) wedge toward the river. The green resistivities are thinnest beneath the thickest part of the higher resistivity but thicken toward the left (i.e. closer to the river) until the green wedge completely pinches out the most resistive zone.

Plotted in Figure 5B is the TWO well driller's log and water table on ERT-11. The drilling information enables a correlation between directly measured parameters and the ERT-inferred geoelectrical structure. A soil analysis of the cores from the well (Sedaghatdoost et al. 2019) provides a quantitative characterization of the correlation (Figure 5C) and shows a good (±7 Ωm or 7%) correlation with depth between ERT-inferred bulk resistivity (yellow squares) and percentage sand content (brown circles).

The correlation is not as good where the sand content rapidly changes back and forth (i.e. at 12.8 m depth). From the bulk resistivities and the Waxman-Smits equation (Waxman and Smits 1968), a variant of Archie's Law for clay-bearing sands, we compute porosity (ϕt) values of ~26-36%. The Waxman-Smits equation is

$$\frac{1}{R_t} = \phi_t^m S^n \left(\frac{1}{R_{water}} + \frac{1}{R_{clay}}\right) \quad (5)$$

where Rt is bulk resistivity [19-33 Ωm], ϕt is total porosity, m is the cementation exponent [~1.7], S is hydraulic saturation [1.0, i.e. fully saturated], n is the saturation exponent [usually taken to be 2], Rwater is the resistivity of the water [9.1 Ωm], and Rclay is the resistivity of the clay [5 Ωm].

From the above results, we suggest the zone described above is "sand-dominated", by which we mean a mixture of clay, silt, and sand where sand is >33% of the total content. We also suggest from the soil analysis in Figure 5C that ERT-derived electrical resistivity is a useful proxy for percent sand content, and therefore that the central core of the higher-resistivity zone (>80 Ωm, i.e. red) is at least 80% sand. We further suggest that the moderate electrical resistivity wedge (i.e. green) is mostly clay and silt, and that the low electrical resistivity (i.e. blue) region near the surface is almost completely clay, as is the shale bedrock at depth.

2.4.2. Time-Domain Electromagnetics

The TEM central-loop transect (see Figure 2B) of length 300 m, with station spacing 10 m, coincides with ERT-2 and ERT-3. Shown in Figure 6A is a stitched-together vertical section comprising 1-D resistivity-depth profiles obtained from separate

inversions of the 31 soundings along the TEM transect. The mutual inductance effects of a multi-turn TX, in addition to the finite ramp-off time, have been taken into account with the IXG-TEM software used (Interpex Limited 2012). The median RMS misfit (the root mean squared misfit between the calculated and apparent resistivities) is 14.6%, which is considered to be an acceptable fit, whereas the mean RMS misfit is 24.5%. A graph of misfit versus sounding number is shown in Figure 6B. Soundings #8 to #10 (which have very large misfits) are adversely influenced by a natural gas pipeline that runs roughly perpendicular to the TEM survey line. The pipeline generated scattered TEM responses at soundings #8 to #12, especially at late time (i.e. the last eight time gates). The resulting distortion in those TEM responses is such that they cannot be fit by a 1-D depth profile (see Figure 6C; left). An example of a TEM response that can be fit to low misfit by a 1-D depth profile is shown in Figure 6C, right.

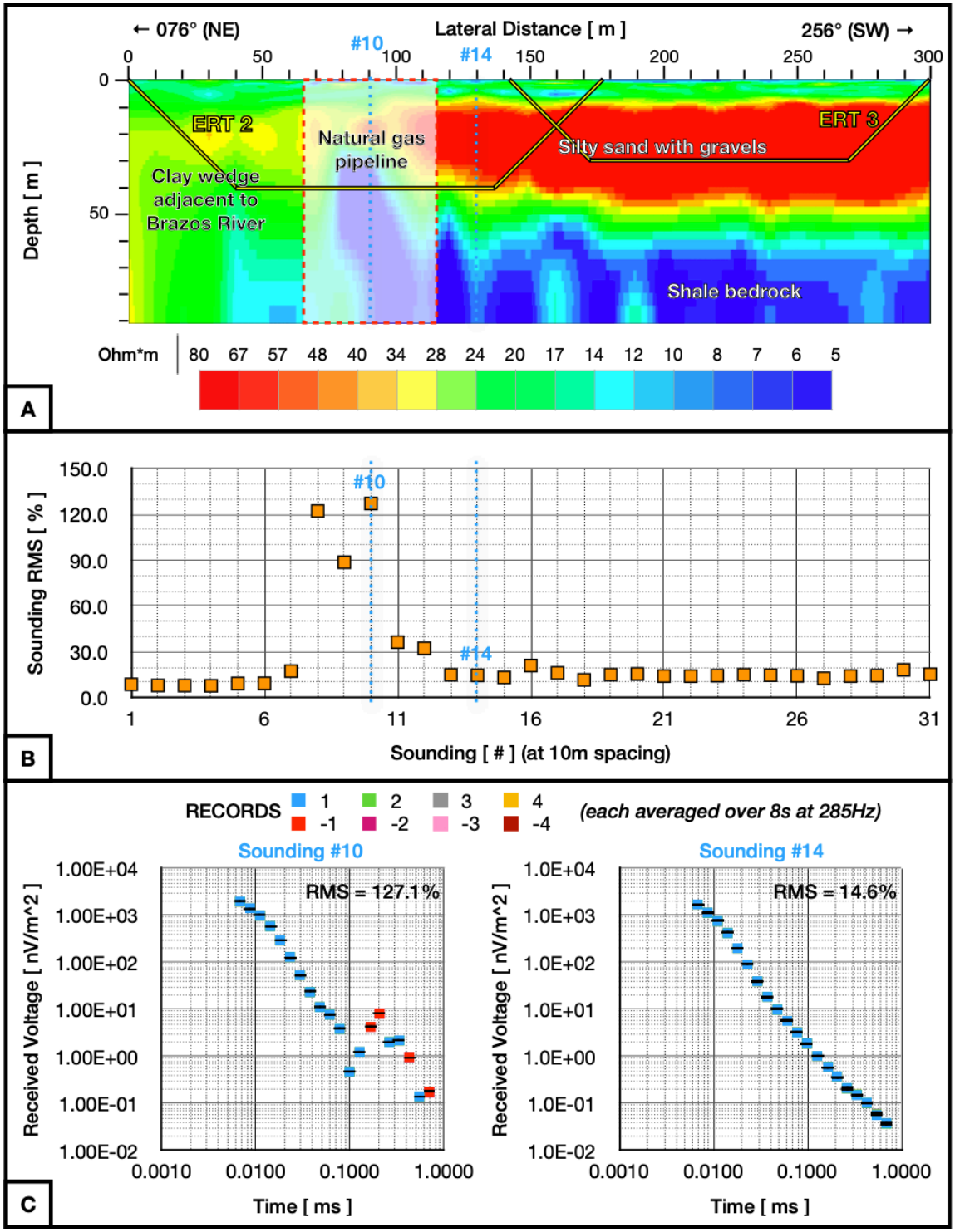
← 076° (NE)
Lateral Distance [m]
256° (SW) →
#10
#14
0
50
100
150
200
250
300
Depth [m]
ERT 2
Natural gas pipeline
ERT 3
Silty sand with gravels
Clay wedge adjacent to Brazos River
Shale bedrock
Ohm*m
80 67 57 48 40 34 28 24 20 17 14 12 10 8 7 6 5
A
Sounding RMS [%]
150.0
120.0
90.0
60.0
30.0
0.0
#10
#14
1
6
11
16
21
26
31
Sounding [#] (at 10m spacing)
B
RECORDS
1
-1
2
-2
3
-3
4
-4
(each averaged over 8s at 285Hz)
Sounding #10
RMS = 127.1%
Sounding #14
RMS = 14.6%
Received Voltage [nV/m^2]
1.00E+04
1.00E+03
1.00E+02
1.00E+01
1.00E+00
1.00E-01
1.00E-02
0.0010
0.0100
0.1000
1.0000
Time [ms]
C

Figure 2.6. TEM results. A Contoured cross-section of 31 TEM soundings (central loop) spaced at 10m intervals. Spatial relation to ERT-2 and ERT-3 highlighted in yellow. Lateral location of natural gas pipeline noted and corresponding region with >30% RMS values noted with 50% opacity; no geologic interpretation made from this region, rather geologic interpretations made from ERT results and TWO well cores. B RMS values for each sounding. Note the characteristic double peak indicative of a survey transect perpendicular to a buried pipe. C Selected voltage decay curves. Per Figure 4B, each of the 4 records is the average of 2280 measurements (i.e. 4 x 2280 = 9120); negligible differences between these records result in only the blue (positive) and red (negative) records being visible on the graphs and also in very tight y-axis error bars (in black). Late time apparent resistivities (i.e. the last 20% of the number of measurements) range from 10-8 to 10-9 Ωm for the soundings not distorted by the pipeline and from 10-6 to 10-9 Ωm for soundings distorted by the pipeline.

Consistent with the ERT results, the TEM resistivity image in Figure 6A shows a zone of higher resistivities (>33 Ωm; i.e. yellow to red) on the western (river-distal) side, a deep zone of lower resistivities (<12 Ωm; i.e. blue), and a wedge of moderate resistivities (~14-28 Ωm; i.e. green) on the eastern side proximal to the river. A comparison can be made between tomograms ERT-2 and ERT-3 and the TEM inversion results. While there are clear differences in size of the resistive zone; the overall shape and ranges of the distribution of electrical resistivities are similar. The TEM result appear to be vertically elongated by a factor of 2 compared to the ERT images; these differences will be addressed in the Discussion.

2.4.3. Modelling the Impact of the Sand Channel on Groundwater Flow

We used HYDRUS-2D to calculate the resulting pressure heads, velocities, and water content at 640 mesh nodes from the modelling of a dry sand channel-belt encased in moist clay and subjected to half a year of flooding on the surface. The proposed scenario includes a hydraulically-isolated, shallow aquifer that has been over-pumped to

the point of being dry and then inundated by flood waters. Under such circumstance the question posed for the modelling is: can this over-pumped, shallow aquifer be refilled in a timely manner and if so, how will that refilling take place? Note that this scenario is not the current state of sand channel-belt at our field site, and note that while hydraulically-isolated means the aquifer cannot interact with bodies of water 101-102 m away (see the white, no-flux nodes in Figure 7B), the aquifer can interact with porewater in immediately adjacent sediments (<100 m).

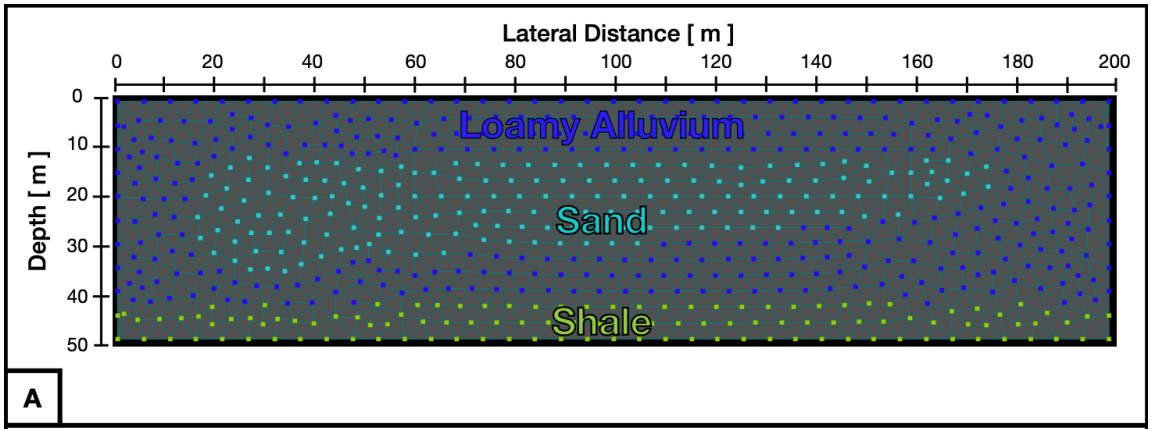

A

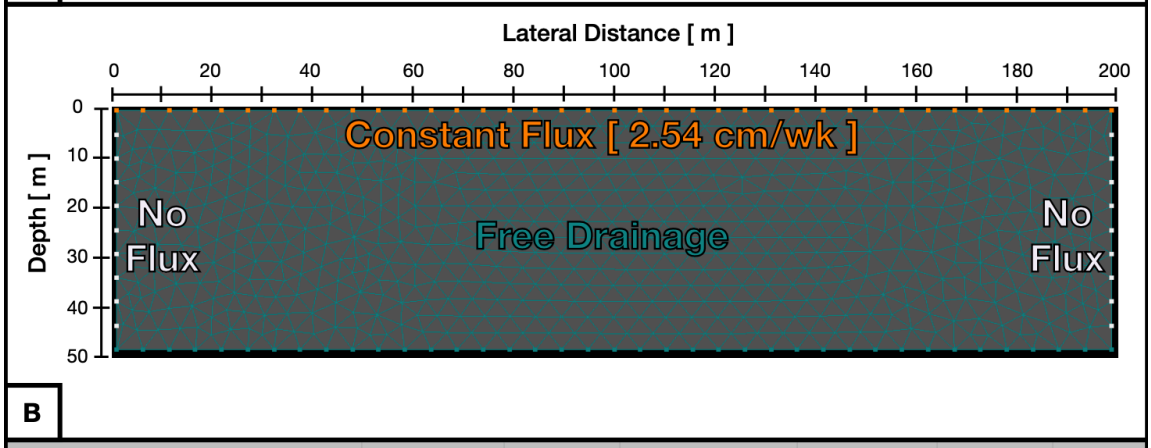

B

DOMAIN PROPERTIES	Qr	Qs	Ks	α	n	l
	%	%	cm/day	1/cm	-	-
Silty Clay Loam	8.9	43	**1.68**	0.01	1.23	0.5
Sand	4.5	43	**712.80**	0.145	2.68	0.5
Silty Clay	7.0	36	**0.48**	0.005	1.09	0.5

C

Figure 2.7. Modelling setup in HYDRUS-2D of a 2-D generalized vertical model of the asymmetric geometry of the channel-belt under variably saturated conditions (i.e. the vadose zone) and lacking lateral, hydrodynamic continuity with its surroundings. A Domain properties; loamy alluvium (blue nodes) surround a sand channel-belt (dark teal nodes) and overlay a shale bedrock (yellow green nodes). B Boundary conditions; constant flux of floodwaters through the surface at 2.54 cm/wk (orange nodes) with no flux at the edges of the model (white nodes) and free drainage everywhere else (very dark teal nodes). C Unsaturated soil hydraulic parameters: Qr = residual water content, Qs saturated water content, Ks = saturated hydraulic conductivity, α = inverse of the air-entry value (or bubbling pressure), n = pore-size distribution index, and l = pore-connectivity parameter.

For the domain properties in Figure 7A, we noted the asymmetric structure of the higher resistivity channel-belt in the ERT tomograms and TEM soundings and created a model to reflect that structure in a generalized geometry (i.e. one side of the channel-belt has a much shallower base than the other side). Drawing on Rhodes' et al. (2017) evidence of a lack of lateral hydrodynamic continuity between the river and the aquifer 300 m inland from the river, we prevented flux through the left and right boundaries of the model, assuming this to be the structure that was blocking flow and propagation of hydraulic heads. Consistent with the tendency of floodplains to flood, we subjected the upper boundary to constant infiltration of 2.54 cm/wk over 26 weeks (i.e. the steady infiltration of floodwaters). Infiltration of floodwater into an agricultural field is dependent on soil type and tillage style. The flux value of 2.54 cm/wk was estimated by weekly-averaged maximum infiltration rate for this field site by personnel on the experimental farm (Al Nelson, pers. comm.). Our petrophysical step consisted of taking the ERT resistivity and TWO well drilling log and soil analysis correlations and

converting them into the closest applicable geomaterials programmed into HYDRUS-2D and their default, isotropic hydraulic properties (see Figure 7C). Specifically, we assigned:

- "Silty Clay Loam" for the loamy alluvium. The Natural Resources Conservation Service (1994) noted this as the geomaterial class for the Weswood-Coarsewood soil present here.
- "Sand" for the sand-dominated channel-belt. We decided to model the simplest case of just sand and save the more complex silty sand for later research.
- "Silty Clay" for the shale bedrock. HYDRUS-2D lacks shale as an option, so we substituted "Silty Clay" because it had the lowest available saturated K value and thereby mostly closely resembled the shale bedrock; however, because the simulation terminated before constant flux on the surface reached the bottom 8m, these values do not appear to affect the simulation.

While these lithologies are empirically correlated from the TWO well, their porosities (i.e. saturated water content Qs in Figure 7) are slightly higher than the theoretically determined values from the Waxman-Smits Equation (Waxman and Smits 1968) of 26-36%. We keep the higher porosities for our synthetic model so as to simulate an aquifer under less clay-clogging recharge and storage conditions.

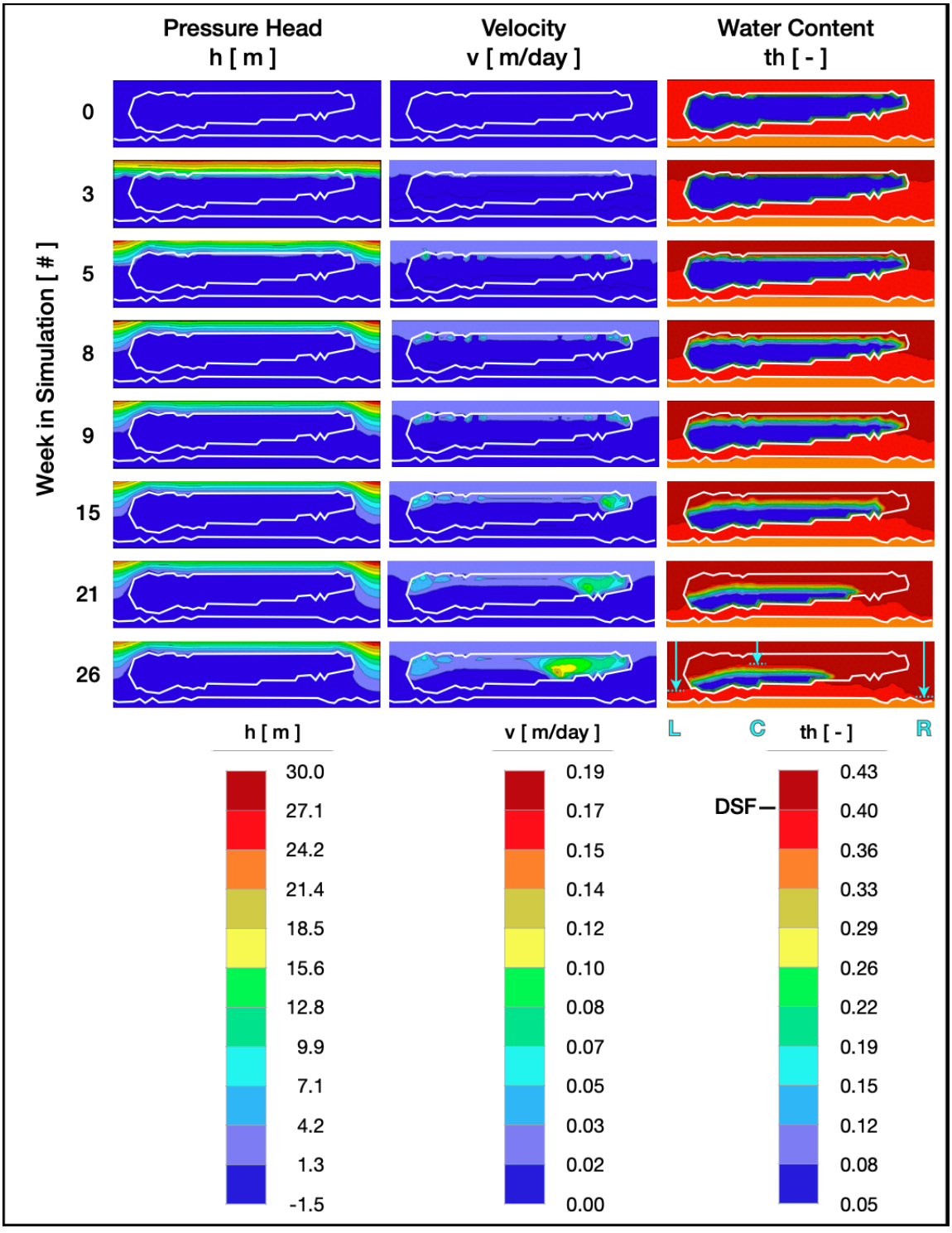
Pressure Head
h [m]
Velocity
v [m/day]
Water Content
th [-]
Week in Simulation [#]
0
3
5
8
9
15
21
26
h [m]
30.0
27.1
24.2
21.4
18.5
15.6
12.8
9.9
7.1
4.2
1.3
-1.5
v [m/day]
0.19
0.17
0.15
0.14
0.12
0.10
0.08
0.07
0.05
0.03
0.02
0.00
L
C
R
th [-]
DSF
0.43
0.40
0.36
0.33
0.29
0.26
0.22
0.19
0.15
0.12
0.08
0.05

Figure 2.8. HYDRUS simulation of constant infiltration; 8 selected weeks spaced out over a 26-week-long simulation. Selected snapshots are included for three model outputs: pressure head, velocity, and water content. The initially-dry sand channel-belt and bedrock are outlined in white throughout the snapshots. At week 26 for water content, the vertical depth of infiltration is indicated by arrows; left L = 37 m, center C = 17 m, and right R = 42 m. Though the 11 step rainbow scale here somewhat resembles the 16 step rainbow scales in Figures 5 and 6, the colors in this figure do not correspond to the electrical resistivities in those figures.

The perimeter of the sand channel-belt is outlined by the white contours in Figure 8. Our description focuses on the water-content column of snapshots, shown at right, though some references will be made to the associated velocities and pressure heads shown in the other two columns.

Initially at week 0, before any infiltration occurs, the simulation shows zero pressure head and zero velocity within both the dry sand channel-belt and the enclosing moist clay-dominated alluvium. The latter has a higher residual water content than sand (see Figure 7C). Over the first three weeks of the simulation, the descending saturation front (DSF; i.e. the boundary above which pore spaces are fully saturated) infiltrates uniformly into the model at a slow velocity (~0.02-0.03 m/day). The DSF reaches the roof of the sand channel-belt at week 3 of the simulation.

Rather than continuing to progress uniformly into the model, starting at week 5 the DSF and its associated pressure head wrap around the upper corners of the dry sand channel-belt, and velocity increases there. The DSF continues this pattern of infiltration through weeks 8-9 of the simulation. The DSF intrudes preferentially beneath the

shallower right base of the sand channel-belt, having infiltrated much faster through the moist, loamy alluvium than through the roof of the channel-belt.

By week 15, the DSF begins to intrude beneath the right base of the sand-dominated channel-belt. The DSF slowly infiltrates vertically into the channel-belt roof but also laterally into the belt from its right edge. The velocity reaches ~0.1 m/day, an order of magnitude higher than the velocity at week 3. The DSF continues this pattern until the end of the simulation at week 26. The final snapshot shows that the DSF has made significant headway into channel-belt from its right side, reaching a maximum velocity of ~0.15 m/day. Though it has vertically infiltrated 37 and 42 m on the left (L) and right (R) sides, respectively, the DSF has infiltrated only 17 m above the left base of the channel-belt (C), which accordingly has remained quite dry.

2.5. Discussion

2.5.1. Existence of the Sand-Dominated Channel-Belt and Clay Wedge

As highlighted earlier, ERT-2 and ERT-3 in Figure 5 show clear differences when compared to the TEM soundings in Figure 6, both in the geometric distribution of electrical resistivities and their relative magnitudes. These differences are expected because these methods probe the earth in fundamentally different ways, ERT by predominantly vertical current flow paths emanating and terminating on grounded electrodes at the surface and TEM by induced currents forming closed horizontal loops within the subsurface. Indeed, it is well known that resolving the resistivity of a resistive layer with TEM is difficult, so the overcompensation—with greater depth and higher

electrical resistivity values in the sand-dominated channel-belt (i.e. the red zone)—is not completely unexpected. While the ERT depths and electrical resistivities values are likely more reliable than those generated with the TEM since the ERT tomograms are truly 2-D and the TEM profile is only a series of 1-D soundings stitched together, both methods show a belt of sand-dominated geomaterials to the west, a wedge of mostly clay to the east near the river, and a very electrically conductive shale bedrock at depth. The TEM soundings therefore confirmed both the presence of the clay wedge and the asymmetric depth to the base of the sand-dominated channel-belt that appear in the ERT tomograms.

From our correlation of the soil analysis of the TWO well's cores to ERT-11 and resulting resistivity assignments, the ERT images generally show:

1) a gently undulating Eocene shale bedrock at depths ~25-30 m below the surface;
2) a layer of clay-rich alluvium ~23-28 m thick overlying the shale which thickens to ~40 m to the east near the Brazos River;
3) a surficial layer of Weswood-Coarsewood soil ~1-2 m thick overlying the alluvium;
4) a meandering belt of sand-dominated alluvium ~7-28 m thick.

The broad, curving structure of the sand-dominated channel-belt is suggestive of an oxbow lake. A channel-belt does indeed exist onsite, but it is composed of high-K sand-dominated alluvium. Thus, instead of compartmentalizing the aquifer, the channel-

belt serves as an integral component of the aquifer. The picture produced here suggests that the clay wedge between the river and the channel-belt performs the compartmentalizing by inhibiting lateral flow. The clay wedge prevents hydraulic head communication of short and long-term river stage pulses between the river and the adjoining floodplain (Rhodes et al., 2017). The seep in Figure 2 resides at a terminus of the channel-belt, suggesting very minor connectivity between the river and the floodplain due to this clay wedge. Therefore, if either drought or over-pumping depletes the alluvial aquifer, clay wedges separating the river from the aquifer can inhibit recharge such that onsite rainfall or inundation of the floodplain will be necessary to recharge the aquifer.

2.5.2. Unexpected Features of the Simulation of Infiltration of Standing Floodwaters into the Highly Conductive Channel

Given the scenario devised for the HYDRUS-2D modelling—namely that a laterally-confined, shallow aquifer has been over-pumped to the point of being dry—is it possible for infiltrating floodwater to refill this over-pumped, shallow aquifer in a timely manner and if so, how exactly will that refilling take place? As shown by the HYDRUS-2D snapshots in Figure 8, wherein no flux is permitted through the left or right boundaries of the model, the vertical infiltrating floodwater unexpectedly fills the initially-dry sand channel-belt primarily through its sides. A visual inspection of the initial (week-0) and final (week-26) models of water content indicates that the saturation front preferentially infiltrates the sand channel-belt from the right side, rather than the left side or roof. We have quantified this aspect of the simulation by plotting the

cumulative distance infiltrated by the DSF into the sand channel-belt from the left side, right side, and the middle of its roof (Figure 9). The following relationships at 26 weeks into the simulation are found:

1) lateral infiltration into the sand-dominated channel-belt is ~240-500% faster than vertical infiltration, depending on the thickness of the sand-dominated channel-belt at its edges;

2) lateral infiltration into the sand-dominated channel-belt's shallower right side is ~75% faster than into the deeper left side;

3) both lateral and vertical cumulative infiltration can be modelled by fourth-order polynomials that increase monotonically in time;

4) vertical cumulative infiltration can also be modelled as a linearly-increasing trend ($R^2 = 0.993$).

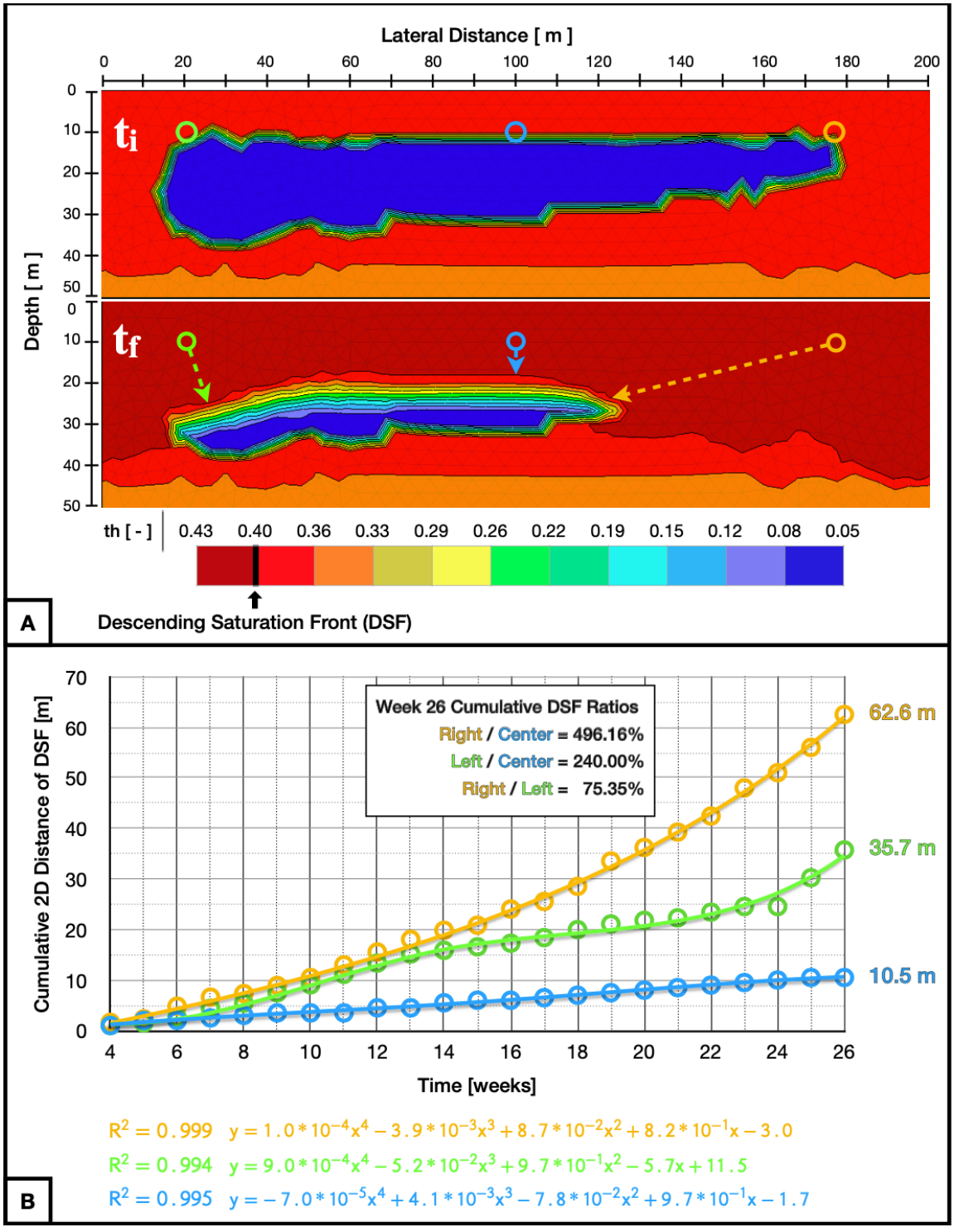
Lateral Distance [m]
0 20 40 60 80 100 120 140 160 180 200
Depth [m]
t_i
t_f
th [-] 0.43 0.40 0.36 0.33 0.29 0.26 0.22 0.19 0.15 0.12 0.08 0.05
Descending Saturation Front (DSF)
A
Cumulative 2D Distance of DSF [m]
Time [weeks]
Week 26 Cumulative DSF Ratios
Right / Center = 496.16%
Left / Center = 240.00%
Right / Left = 75.35%
62.6 m
35.7 m
10.5 m
$R^2 = 0.999$ $y = 1.0*10^{-4}x^4 - 3.9*10^{-3}x^3 + 8.7*10^{-2}x^2 + 8.2*10^{-1}x - 3.0$
$R^2 = 0.994$ $y = 9.0*10^{-4}x^4 - 5.2*10^{-2}x^3 + 9.7*10^{-1}x^2 - 5.7x + 11.5$
$R^2 = 0.995$ $y = -7.0*10^{-5}x^4 + 4.1*10^{-3}x^3 - 7.8*10^{-2}x^2 + 9.7*10^{-1}x - 1.7$
B

Figure 2.9. Descending saturation front (DSF) within the sand channel-belt. A Initial and final snapshots of water content; fully saturated is a water content 0.4 and greater. B Cumulative distance of the descending front of saturating water into the relic sand channel-belt at three different locations.

The higher residual water content of the silty-clay loam, compared to that of the sand apparently allows the surface-water infiltration to more rapidly saturate the former, even though the saturated K of sand is more than two orders of magnitude greater than that of loam. As groundwater wraps around the sides of the sand channel-belt, lateral hydraulic pressure is increased. The resulting pressure head rapidly pushes water into the sand-dominated channel-belt, leading to much higher lateral infiltration rates than the vertical rate, but even half a year of such infiltration is not enough to fully recharge the over-pumped aquifer.

2.5.3. Implications and Future Research

The combination of the clay wedge between the river and the aquifer with the asymmetrical channel-belt geometry results in asymmetric recharge of the aquifer. We find that the side of the channel belt with the shallower base will recharge via floodwater infiltration faster than the side with the deeper base but also that recharge through the roof will be comparatively slower than lateral infiltration. Therefore, the depth to the water table may vary on the order of several meters over less than 200 m across the surface, fluctuate seasonally in time, and even be underlain by a dry pocket. If a well was drilled into this deepest part of the aquifer (i.e. the well which over-pumped the aquifer), the lack of lateral connectivity with the river and an asymmetric filling pattern ultimately result in this well's well screen and pump being inside that dry pocket, even

after half a year of constant infiltration into a silt-free sandy aquifer (i.e. an aquifer with a very high K). We make two conclusions from this:

1) If even half a year of constant floodwater infiltration into a silt-free sandy aquifer is not enough to fully recharge an aquifer close to the Earth's surface, great care should be taken by landowners and groundwater managers to avoid over-pumping shallow aquifers.

2) If such a scenario as the one modelled here (or similar) occurs, a new well should be drilled in the side of the channel-belt with the shallower base, as that side will recharge faster than the other. In other words, the best placement for new wells may not always be in the deepest part of the aquifer.

More broadly, our approach of combining near-surface geophysical imaging with hydrologic modelling informs the placement of production or monitoring water wells to study water and chemical fluxes and transformations in alluvial floodplain aquifers and helps explain the evidence others have reported on the extreme level of compartmentalization of shallow, alluvial aquifers that are bounded by impermeable bedrock below (e.g. Brunner et al. 2009). As the field scale was chosen for both the geophysical possibilities (i.e. the shape and size of the channel-belt) and the relevant processes, the asymmetric infiltration process discovered in modelling could occur throughout the floodplain. A larger-scale geophysics survey—using either airborne EM or denser, ground-based 2-D coverage—could discover multiple channel-belts, which would open new avenues of investigation: are the various channel-belts within the

floodplain discharging independently into the Brazos River? or are they hydraulically connected such that water fluxes between them prior to discharge at stream?

These more spatially dense geophysical datasets would be necessary to model other scenarios, including: 1) how a shallow aquifer is depleted due to drought or over-pumping; 2) how land cover affects recharge (e.g. differences between ploughed fields—i.e. our site—unploughed fields, forests, urban settings, etc.), and 3) how the presence or absence of a clay wedge along the riverbank affects discharge to the river. The presence or absence needs to be evaluated because, while Rhodes et al. (2017) showed the lack of lack continuity in this region and our research showed that it is due to the clay wedge, we cannot assume the clay wedge is present along the entire length of the Brazos River in its floodplain without performing additional geophysical surveys.

2.6. Conclusions

Using the soil analysis of well cores from the Texas Water Observatory, we constrained the interpretation of our ERT and TEM geophysical results. We partially corroborated the existence of a clay-dominated channel-belt, as proposed by Rhodes et al. (2017) to explain the lack of lateral connectivity between the alluvial aquifer and the nearby Brazos River. We discovered the channel-belt but found it to be sand-dominated as well as asymmetrically shaped, and that the channel-belt is separated from the river by a clay wedge, thus indicating that the channel-belt is in fact the aquifer itself and that it is the clay wedge that inhibits hydraulic connectivity and therefore flow between it and

the river. We then input the asymmetric geometry of the channel-belt—generalized from several tomograms—into HYDRUS-2D using simplified lithologies to explore a proof-of-concept model. This model simulated the impact of a flood on an alluvial floodplain containing a sand channel-belt that has been depleted of water content due to over-pumping. The modelling revealed that the saturation front preferentially enters the originally dry channel-belt through its sides, not its roof. This represents an improvement in understanding of how the hydraulic architecture of channel belts shapes preferential hydraulic connectivity within an alluvial floodplain. The 2-D mapping and hydrologic modelling results advances our understanding of where and how water is stored and released from a heterogeneous alluvial aquifer and a river. This result has implications for water well placement for production, monitoring, environmental remediation and studying the timing, fluxes and transformations of water and elements moving through a watershed.

2.7. References

Amorosi A., Pavesi M., Lucchi M. R., Sarti G. and Piccin A. 2008. Climatic signature of cyclical fluvial architecture from the Quaternary of the central Po Plain, Italy. Sedimentary Geology, 209(1-4), 58-68.

Babek O., Sedlacek J., Novak A. and Letal A. 2018. Electrical resistivity imaging of anastomosing river subsurface stratigraphy and possible controls of fluvial style change in a graben-like basin, Czech Republic. Geomorphology, 317, 139-156.

Binley A. and Beven K. 2003. Vadose zone flow model uncertainty as conditioned on geophysical data. Groundwater, 41(2), 119-127.

Blum M., Martin J., Milliken K. and Garvin M. 2013. Paleovalley systems: insights from Quaternary analogs and experiments. Earth Science Reviews, 116, 128-169.

Blum M. D. and Tornqvist T. E. 2000. Fluvial responses to climate and sea-level change: a review and look forward. Sedimentology, 47(1), 2-48.

Borner F. D., Schopper J. R. and Weller A. 1996. Evaluation of transport and storage properties in the soil and groundwater zone from induced polarization measurements. Geophysical Prospecting, 44(4), 583-601.

Boucher M., Favreau G., Descloitres M., Vouillamoz J. M., Massuel S., Nazoumou Y., Cappelaere B. and Legchenko A. 2009. Contribution of geophysical surveys to groundwater modelling of a porous aquifer in semiarid Niger: an overview. Comptes Rendus Geoscience, 341(10-11), 800-809.

Brunner P., Cook P. and Simmons C. 2009. Hydrogeologic controls on disconnection between surface water and groundwater. Water Resources Research, 45(1), W01422. https://doi.org/10.1029/2008WR006953

Bryant M., Falk P. and Paola C. 1995. Experimental-study of avulsion frequency and rate of deposition. Geology, 23(4), 365-368.

Castagna M., Bellin A. and Chiogna G. 2015. Uncertainty estimation and evaluation of shallow aquifers' exploitability: the case study of the Adige Valley Aquifer (Italy). Water, 7(7), 3367-3395.

Cattaneo A. and Steed R. J. 2003. Transgressive deposits: a review of their variability. Earth Science Reviews, 162(3-4), 187-228.

Chambers J. E., Wilkinson P. B., Wealthall G. P., Loke M. H., Dearden R., Wilson R., Allen D. and Ogilvy R. D. Hydrogeophysical imaging of deposit heterogeneity and groundwater chemistry changes during DNAPL source zone bioremediation. Journal of Contaminant Hydrology, 118(1-2), 43-61.

Edwards L. S. 1977. A modified pseudosection for resistivity and IP. Geophysics, 42, 1020-1036.

Everett M. 2013. Near-surface applied geophysics. Cambridge, UK: Cambridge University Press

Everett M. E. and Meju M. A. 2005. Near-surface controlled-source electromagnetic induction: background and recent advances. In Y. Rubin & S.S. Hubbard (Eds.), Hydrogeophysics (pp. 157-183). New York, NY: Springer.

Ezersky M., Legchenko A., Al-Zoubi A., Levi E., Akkawi E. and Chalikakis K. 2011. TEM study of the geoelectrical structure and groundwater salinity of the Nahal Hever sinkhole site, Dead Sea shore, Israel. Journal of Applied Geophysics, 75(1), 99-112.

Fitterman, D. 2015. Tools and techniques: active-source electromagnetic methods. In: *Treatise on Geophysics, 2nd ed.* (ed. G. Schubert), pp. 295-333. Elsevier.

Frei S., Fleckenstein J. H., Kollet S. J. and Maxwell R. M. 2009. Patterns and dynamics of river-aquifer exchange with variably-saturated flow using a fully-coupled model. Journal of Hydrology, 375(3-4), 383-393.

Gomez E., Larsson M., Dahlin T., Barmen G. and Roseberg J. E. 2019. Alluvial aquifer thickness and bedrock structure delineation of electromagnetic methods in the highlands of Bolivia. Environmental Earth Sciences, 78(3), A#84.

Gottschalk I. P., Hermans T., Knight R., Caers J., Cameron D. A., Regnery J. and McCray J. E. 2017. Integrating non-colocated well and geophysical data to capture subsurface heterogeneity at an aquifer recharge and recovery site. Journal of Hydrology, 555, 407-419.

Grygar T. M., Elznicova J., Tumova S., Famera M., Balogh M. and Kiss T. 2016. Floodplain architecture of an actively meandering river (the Ploucnice River, the Czech Republic) as revealed by the distribution of pollution and electrical resistivity tomography. Geomorphology, 254, 41-56.

Gueting N., Klotzche A., vander Kruk J., Vanderborght J., Vereecken H. and Englert A. 2015. Imaging and characterization of facies heterogeneity in an alluvial aquifer using GPR full-waveform inversion and cone penetration tests. Journal of Hydrology, 524, 680-695.

Hajek E. A., Heller P. L. and Sheets B. A. 2010. Significance of channel-belt clustering in alluvial basins. Geology, 38(6), 535-538.

He X., Koch J., Sonnenberg T. O., Jorgensen F., Schamper C. and Refsgaard J. C. 2014. Transition probability-based stochastic geological modelling using airborne geophysical data and borehole data. Water Resources Research, 50(4), 3147-3169.

Holbrook J. and Schumm S.A. 1999. Geomorphic and sedimentary response of rivers to tectonic deformation: a brief review and critique of a tool for recognizing subtle epeirogenic deformation in modern and ancient settings. Tectonophysics, 305(1-3), 287-306.

Hoyer A. S., Vignoli G., Hansen T. M., Vu L. T., Keefer D. A. and Jorgensen F. 2017. Multiple-point statistical simulation for hydrogeophysical models: 3-D training image development and conditioning strategies. Hydrology and Earth System Sciences, 21(12), 6069-0689.

Interpex Limited. 2012. IXG-TEM instruction manual. http://www.interpex.com

Jerolmack D. J. and Paola C. 2007. Complexity in a cellular model of river avulsion. Geomorphology, Special Issue 91(3-4), 259-270.

Kolker A. S., Cable J. E., Johannesson K. H., Allison M. A. and Inniss L. V. 2013. Pathways and processes associated with the transport of groundwater in deltaic systems. Journal of Hydrology, 498, 319-334.

Linde N. 2014. Falsification and corroboration of conceptual hydrological models using geophysical data. Wiley Interdisciplinary Reviews - Water, 1(2) 151-171.

Linde N., Renard P., Mukerji T. and Caers J. 2015. Geological realism in hydrogeological and geophysical inverse modelling: a review. Advances in Water Resources, 86(A), 86-101.

Loke M. H. 1999. Electrical imaging surveys for environmental and engineering studies: a practical guide to 2-D and 3-D surveys. https://urldefense.com/v3/__https://www.aarhusgeosoftware.dk__;!!KwNVnqRv!RiVLnEsgJgJsUkGy2ApB0CccEj6nd7F9greAKlO7_fyI1HCFwhZG25k35X_9VcDmDSgqd9tcKrKPGA$

Mackey S. D. and Bridge J. S. 1995. Three-dimensional model of alluvial stratigraphy: theory and applications. Journal of Sedimentary Research, B65(1), 7-31.

Maddy D., Bridgeland D. and Westaway R. 2001. Uplift-driven valley incision and climate-controlled river terrace development in the Thomas Valley, UK. Quaternary International, 79, 23-36.

Mariethoz G., Renard P., Cornator F. and Jaquet O. 2009. Truncated plurigassian simulations to characterize aquifer heterogeneity. Groundwater, 47(1), 13-24.

Martinius A. W. 2000. Labyrinthine facies architecture of the Tortola fluvial system and controls on deposition (Late Oligocene - Early Miocene, Loranca Basin, Spain). Journal of Sedimentary Rock, 70(4), 850-867.

Mastrocicco M., Vignoli G., Colombani N. and Abu Zeid N. 2010. Surface electrical resistivity tomography and hydrogeological characterization to constrain

groundwater flow modelling in an agricultural field site near Ferrara (Italy). Environmental Earth Sciences, 61(2), 311-322.

Mohrig D., Heller P. L., Paola C. and Lyons W. J. 2000. Interpreting avulsion processes from ancient alluvial sequences: Guadalope-Matarranya (northern Spain) and Wasatch Formation (western Colorado). Geological Society of America Bulletin, 112(12), 1787-1803.

Nichols G. J. and Fisher J. A. 2007. Processes, facies, and architecture of fluvial distributary system deposits. Sedimentary Geology, Special Issue 195(1-2), 75-90.

Oldenborger G. A., Knoll M. D., Routh P. S. and LaBrecque D. J. 2007. Time-lapse ERT monitoring of an injection/withdrawal experiment in a shallow unconfined aquifer. Geophysics, 72(4), F177-F187.

Outlined Map of North America. 2019. World Atlas. https://non-art.info/map-of-blank-outline-map-of-north-america/outlined-map-of-north-america-map-of-north-america/

Perri M. T., Cassiani G., Gervasio I., Deiana R. and Binley A. 2012. A saline tracer test monitored via both surface and cross-borehole electrical resistivity tomography: comparison of time-lapse results. Journal of Applied Geophysics, 79, 6-16.

Rhodes K. A., Proffitt T., Rowley T., Knappett P. S. K., Montiel D., Dimova N., Tebo D. and Miller G. R. 2017. The importance of bank storage in supplying baseflow

to rivers flowing through compartmentalized, alluvial aquifers. Water Resources Research, 53(12), 10539-10557.

Savoy H., Kalbacher T., Dietrich P. and Rubin Y. 2017. Geological heterogeneity: goal-oriented simplification of structure and characterization needs. Advances in Water Resources, 109, 1-13.

Sedaghatdoost A., Mohanty B., and Huang Y. 2019. The effect of heterogeneities in soil physical and chemical properties on redox biogeochemistry in subsurface soils. American Geophsyical Union Fall Meeting 2019, Expanded Abstracts, San Francisco, United States, B33E-08.

Šimůlek J., Šejna M. and van Genuchten M. T. 2012. The HYDRUS software package for simulating two- and three-dimensional movement of water, heat, and multiple solutes variably saturated porous media - technical manual (version 2.0). PC Progress, Prague, Czech Republic

Slingerland R. and Smith N. D. 2004. River avulsions and their deposits. Annual Review of Earth & Planetary Sciences, 32, 257-285.

Taha Z. P. and Anderson J. B. 2008. The influence of valley aggradation and listric normal faulting on styles of river avulsion: a case study of the Brazos River, Texas, USA. Geomorphology, 95(3-4), 429-448.

Texas Water Development Board (TWDB). 2012. Water for Texas 2012: State Water Plan. https://www.twdb.texas.gov/waterplanning/swp/2012/index.asp

United States Geological Survey (USGS). 2017. Brazos, Freestone, & Robertson Counties Lidar, 2017-03-01. https://data.tnris.org/collection/b6ea8e3a-c8b7-4d97-b4d1-4eb8172eb87d

Waxman M.H. and Smits L.J.M. 1968. Electrical conductivities in oil-bearing shaly sands. Society of Petroleum Engineers Journal, 8(2): 107–122.

Wright V. P. and Marriott S. B. 1993. The sequence stratigraphy of fluvial depositional systems - the role of floodplain sediment storage. Sedimentary Geology, 86(3-4), 203-210.

Wrobleski C. L. 1996. An aquifer characterization at the Texas A&M University Brazos River hydrologic field site, Burleson Co., Texas (Master's thesis). Retrieved from OAKTrust Library via https://oaktrust.library.tamu.edu/handle/1969.1/ETD-TAMU-1996-THESIS-W76. College Station, TX: Texas A&M University.

Zaleha, M. J. 1997. Fluvial and lacustrine palaeoenvironments of the Miocene Siwalik Group, Khaur area, northern Pakistan. Sedimentology, 44, 349-368.

Zhang Y., Green C. T. and Fogg G. E. 2013. The impact of medium architecture of alluvial settings on non-Fickian transport. Advances in Water Resources, 54, 78-99.

Zonge K., Wynn J. and Urquhart S. 2005. Resistivity, induced polarization, and complex resistivity. In D.K. Butler (Ed.), Near Surface Geophysics (pp. 265-300). Tulsa, OK: Society of Exploration Geophysicists.

3. BIDIRECTIONAL PREFERENTIAL FLOW IN ALLUVIAL FLOODPLAINS: A KEY TO MODELLING AND SUSTAINABLY MANAGING SHALLOW GROUNDWATER RESOURCES

3.1. Introduction

Management of water resources in the 21st century has become increasingly necessary and complex (Gleeson et al. 2020; Griebler and Avramov 2015; Klove et al. 2014; Xiang et al. 2021). This is certainly true for shallow groundwater resources in alluvial floodplains that are highly susceptible to overexploitation and contamination due to their proximity to the surface (Dafny and Silburn 2014; Macdonald et al. 2018). The proximity of shallow aquifers to the atmosphere, plants and rivers allows for bidirectional groundwater flow, which refers to groundwater that can flow in either of opposing directions through a given medium. Examples of bidirectional flow include:

- the vadose zone, wherein meteoric water infiltrates downward but may also rise via capillary action (e.g. Scheidegger et al., 2021)
- forested slopes, wherein water uptake by tree roots may locally reverse the generally downhill-sloping hydraulic gradient via local cones of depression (e.g. Bosch et al., 1996; Ghazavi et al., 2011)
- riverbanks, wherein natural or artificial river stage fluctuations drive water in and out of bank storage (e.g. Rhodes et al., 2017)

Knowing the location and scale of bidirectional flow and the factors controlling flow reversals is vital for developing hydrogeological models of the subsurface and subsequent predictions of groundwater flow paths (as well as contaminant transport). Such models comprise a scientific basis to inform groundwater management decisions (TWDB, 2017; Clark et al., 2011).

Bidirectional flow through the river banks and in the vadose zone of an alluvial floodplain is the focus of this study. Alluvial floodplains cover vast areas adjacent to Earth's major river systems. Floodplains grow through river meander migration and overbank flow, and they are defined by their boundary with an active channel (Bridge, 2009; Nanson and Croke, 1992). Typical lowland river floodplain architecture consists of elements such as cutoff channels, crevasse splays, overbank deposits, clay wedges, each exhibiting a range of particle sizes from clay to sand. The distribution of these structures and grain sizes defines the architecture that hosts shallow groundwater resources. An architectural element that is explored in this study is a clay wedge that is physically positioned between the river channel and the floodplain aquifer(s); the fine particle size of the clay inhibits hydraulic connectivity between river water and its immediately adjacent permeable bank where short-term bank storage occurs and the groundwater of the aquifer.

Unfortunately, the degree to which the clay wedge inhibits hydraulic connectivity remains poorly understood (Menichino and Hester, 2015). Preliminary data from Rhodes et al. (2017) suggest that while connectivity may generally be low, it is not necessarily low at all locations or times within the clay wedge. We therefore hypothesize that while

a clay wedge generally inhibits connectivity between a meandering river and a floodplain aquifer, bidirectional preferential pathways may allow for focused connectivity in both space and time. Our goals are therefore to: 1) identify the location and timing of a hypothesized, preferential pathway capable of bidirectional flow using rigorously appraised geophysical data; 2) develop a hydrogeological explanation for the existence of such a pathway; and 3) highlight the implications of these findings for the distribution of water, sediment, and contaminants. These findings will help constrain theoretical models of the formation alluvial floodplains and the groundwater that flows through them as well as expanding the record of empirical phenomena to aid geophysicists, engineers and hydrogeologists aiming to characterize in alluvial floodplains.

In the following sections of this paper, we discuss the characteristics of the field site and the time-lapse geophysical and hydrological methods employed. We appraise the quality of the geophysical data with regard to its robustness, sensitivity, repeatability, and reproducibility, and take into account river stage fluctuations observed 25 km upstream of the field site. After describing the geophysical time-lapse results, we perform geophysical forward modeling to investigate the smoothing effects of the inversion process on the interpretation. We also explore the lag time between precipitation and a spatially and temporally concentrated feature in the time-lapse images that appears to be a preferential fast flow pathway. We conclude with a final hydrogeological interpretation of the subsurface, explore the implications, and note some areas for future research.

3.2. Field Site

We conducted a 61-day time-lapse electrical resistivity tomography (ERT) study adjacent and parallel to the Brazos River in Burleson County, Texas. Six major rain events occurred during the study period (NOAA, 2021). The precipitation provided an opportunity to observe spatially concentrated changes of electrical resistivity in the soil and sediment which we then interpreted as preferential pathways of rainwater infiltrating into the subsurface.

The ERT transect was located above a known clay wedge that obstructs hydraulic communication between an outer bend of the Brazos River and the adjacent Brazos River Alluvial Aquifer. The field site is located on agricultural land managed by Texas A&M University Farm Service (Martin et al., 2020). Both the Brazos River and the investigated portion of the aquifer beneath the field site run roughly parallel to each other in a NNW-SSE orientation. Soil in the region is moderately well drained and has very low permeability and very high shrink-swell potential (USDA, 2014).

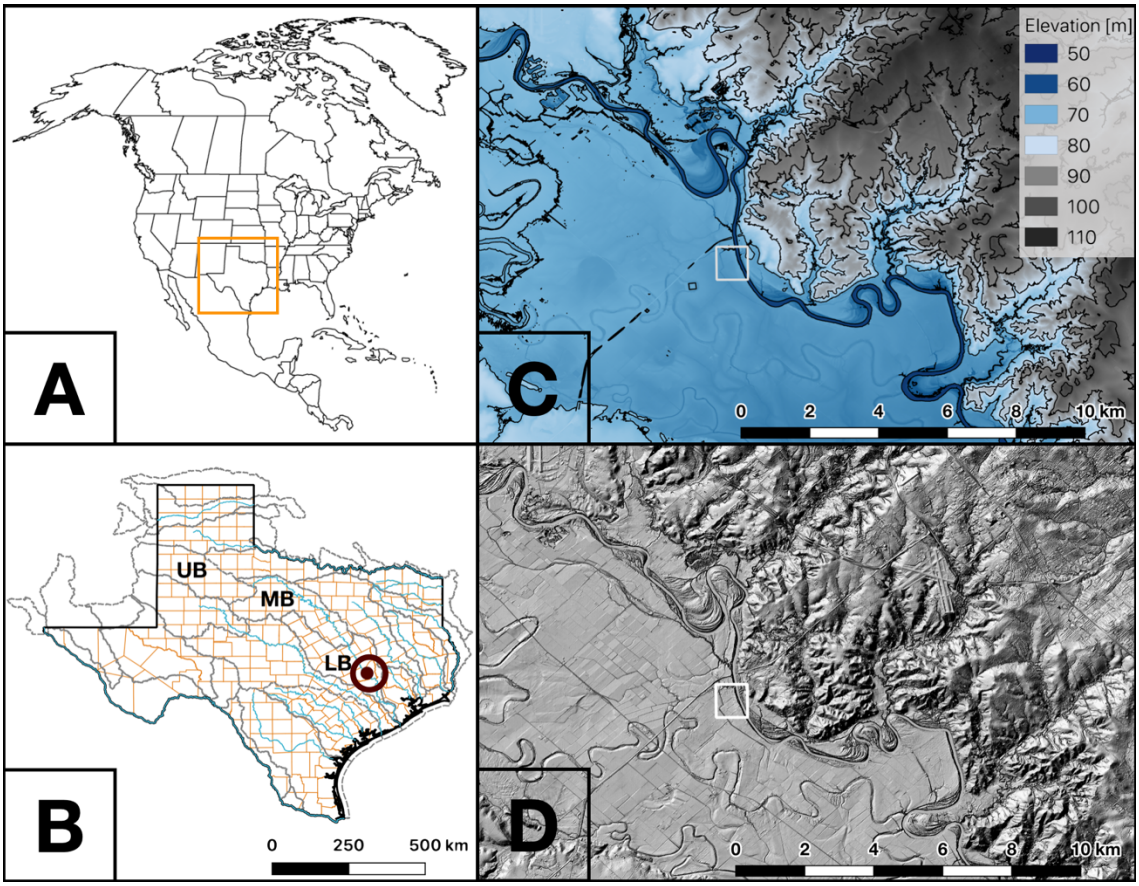

Figure 3.1. Context maps for fieldwork site; north toward the top (from Martin et al. 2020). A North America. Orange box highlights region of subfigure B. B Texas. County boundaries are displayed orange; major rivers are blue; and watershed boundaries are dotted grey (UB/MB/LB = Upper/Middle/Lower Brazos). Field site (bullseye) is in Burleson County adjacent to the Brazos River in the Lower Brazos Watershed. C Topography of the Brazos River floodplain (dark to pale blue) in lower left half around the Brazos River (dark blue); adjacent outcrop of the Yegua-Jackson formation (light to dark grey) in upper right half. D Hillshade view of the Brazos River floodplain in lower left half; adjacent highlands in upper right half containing the city of College Station, TX. Topography rendered from 2017 USGS lidar data at 70 cm horizontal resolution.

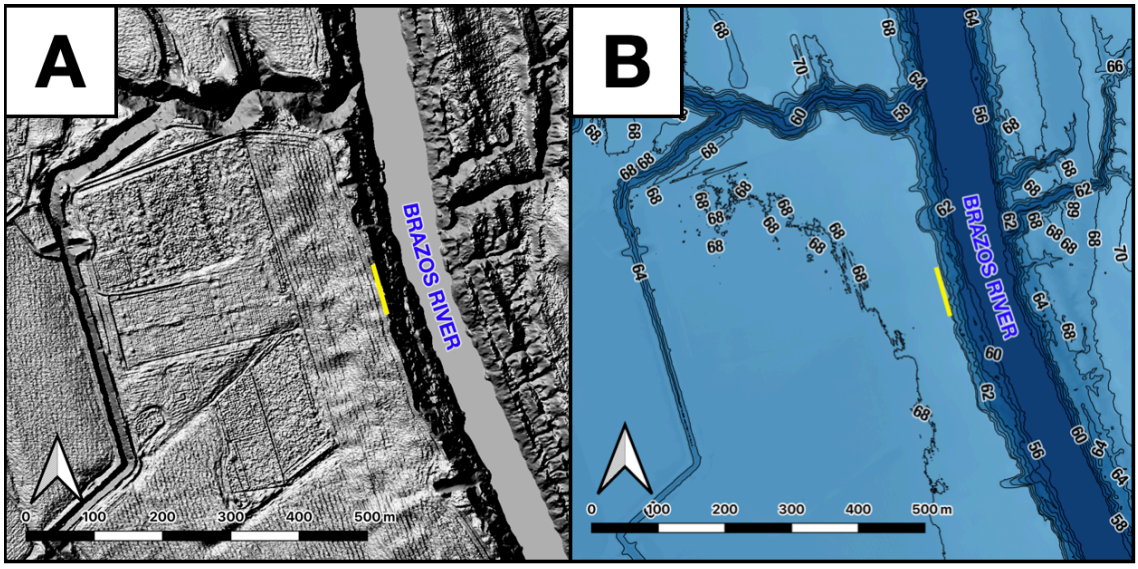

Figure 3.2. Map of fieldwork site. The yellow line is the electrical resistivity survey line, which ran from north (0 m) to south (78 m) between the agricultural fields to the west and the bluff overlooking the Brazos River to the east. Rendered from 2017 USGS lidar data at 70 cm horizontal resolution. North toward the top. A Hillshade view. B Topographic view; units in meters above sea level (masl).

3.3. Methods

3.3.1. Electrical Resistivity Tomography and Data Appraisal

The primary method to identify a hypothesized, bidirectional preferential pathway at the field site is ERT in a 14-electrode, dipole-dipole configuration at 6 m electrode spacing with 78 m array length. The basic principles of ERT acquisition, analysis, and interpretation are given elsewhere (Everett 2013; Furman et al. 2003; Loke 1999; Martin et al. 2020; Zonge et al. 2005). We define three terms here in simplified form (see the previously mentioned references for the scientific definitions):

1. Apparent resistivity – the raw data. Its vertical cross-section is called a pseudosection. These values do not reflect actual Earth resistivity because the

voltage measurement plotted at a given subsurface point is sensitive to a spatial average of the electrical properties of the geomaterials surrounding it.

2. Actual resistivity – the result of data inversion. Its vertical cross-section is called a tomogram. These values (albeit imperfectly) reflect Earth resistivity as a result of iteratively comparing and adjusting candidate resistivity models.
3. Root mean square (RMS) misfit – a measure of the difference between the apparent resistivity data and the corresponding response of the model obtained by inversion. RMS misfit is expressed as a percentage; values between 2-10% capture overall trends without fitting an excessive amount of noise.

We chose a location for the ERT electrode array directly above a clay wedge separating the river from the alluvial aquifer. We performed 39 surveys over 61 days from 2020-12-03 to 2021-02-01 (format yyyy-mm-dd); gaps in coverage are due to holidays and muddy conditions due to precipitation that prevented site access. We later filled in the time gaps of non-surveyed days by interpolation for visualization purposes only; the data appraisal analyses herein are performed only on the original, non-interpolated datasets.

In the tomograms, we identified a potential bidirectional preferential pathway that we called the House (due to its pentagonal shape) that is ~5 m wide and 4.5 m tall (see Figure 3A). It is centered ~3.7 mbgl (meters below ground level), and its resistivity fluctuates from 24-380 Ωm throughout the time-lapse. This large temporal fluctuation

contrasts with the relatively narrow range (~8-21 Ωm) found at other points on the time-lapse tomograms. We appraised the reliability of the ERT time-lapse imaging of the feature of interest by the following three procedures:

1. Robustness — how is our interpretation affected by a large change to the data collection process? This was tested by removing all data that utilize the electrode closest to the House.
2. Sensitivity — how is our interpretation affected by small perturbations to the measured data? This was tested by altering apparent electrical resistivity values to which the House is sensitive by a small amount, namely ±1-5%.
3. Repeatability and reproducibility — how is our interpretation affected by ambient environmental conditions? This was tested by comparing the imaging of the House during dry versus wet spells.

3.3.2. Hydrological Data

In addition to the ERT data, we also collected groundwater table, river stage and precipitation data. Unfortunately, the pressure transducer in the monitoring well (Texas Water Observatory (TWO) well (30°33'8.94"N 96°25'22.63"W)) failed a few days before our 61 day time-lapse study period began. We regressed the water table on the river stage over the previous several months using a polynomial function and applied this function to estimate the local water table during our survey period. River-stage measurements were taken by the United States Geologic Survey (USGS) at HW21 (USGS, 2021), 25.3 km upstream from the site. We adjusted river stage measured 25.3

km upstream to reflect the river stage adjacent to the site based on 9 months of concurrent observations of river stage at HW21 and HW60 (Rhodes et al., 2017). Rhodes' et al. (2017) 2015-2016 showed an ~5 m drop in Brazos River elevation between HW21 and HW60. HW60 is located only 730 m north of the study site. Finally, we used daily precipitation records from the National Oceanic & Atmospheric Administration at College Station Easterwood Airport, ~7 km from the study site (NOAA, 2021).

3.4. Results

Using the time-lapse electrical resistivity tomography and hydrologic data, we describe herein qualitatively and quantitatively some prominent subsurface features and suggest their geologic explanation. A representative snapshot from the time-lapse ERT sequence is shown in Figure 3.

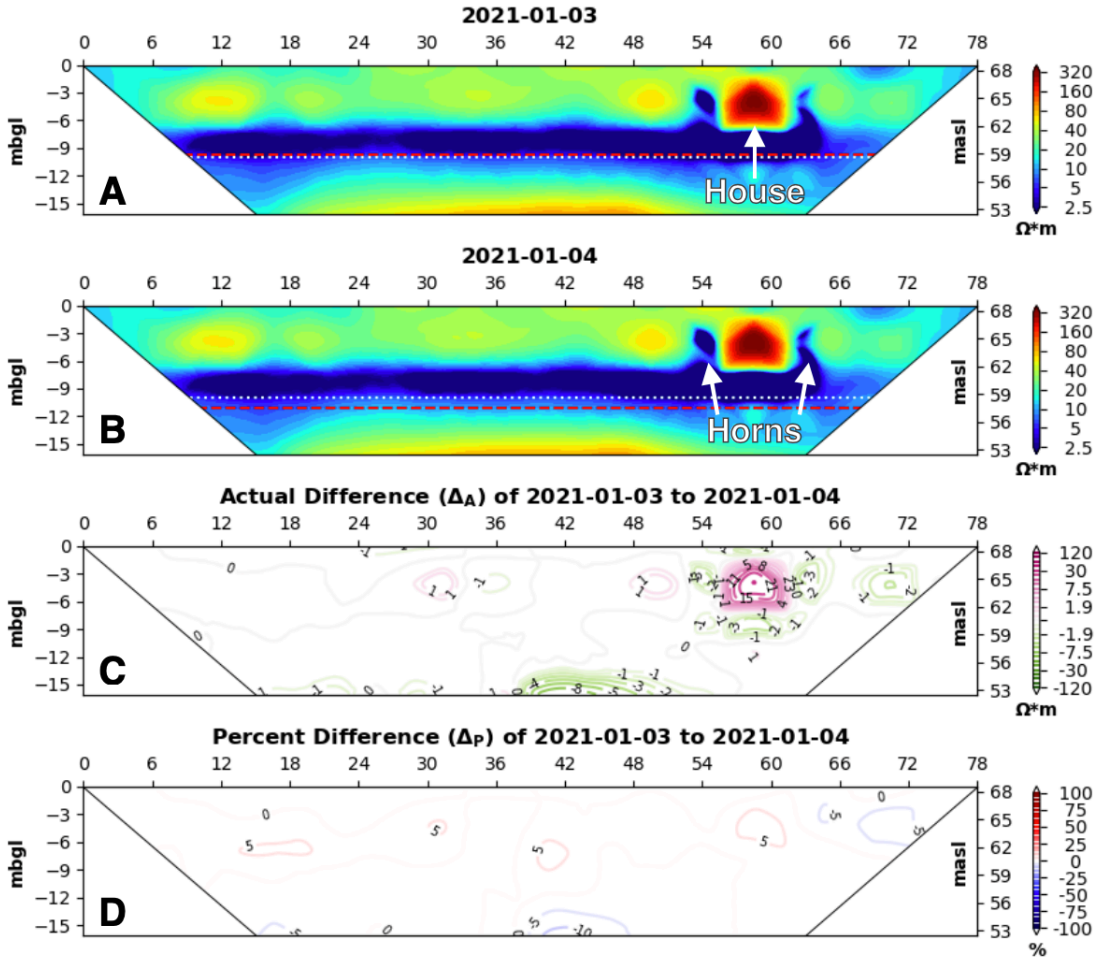

Figure 3.3. The time-lapse video (link below) contains 60 frames, each containing 4 subfigures; this figure is a snapshot of the time-lapse video. The axes are identical for all 4 subfigures; 78 m across the top x-axis (north to the left and south to the right) and 16.1 m deep along the z-axis, displayed as meters below ground level (mbgl) on the left and meters above sea level (masl) on the right. A Tomogram of the contoured electrical resistivity on a given day. We plot the current Brazos River stage as a dashed red line and the water table as a dotted white line. B Tomogram of the contoured electrical resistivity on the following day. C Absolute differences between those two tomograms. D Relative differences [%] between those two tomograms. (https://www.hydroshare.org/resource/f93624835f5145c2b597c9944aca9357/data/contents/MOIMOI_TimeLapse_MovingGW.mp4)

3.4.1. Observations of Colorbar Scales

The colorbars are logarithmically scaled in Figures 3A-B to capture >96% of subsurface bulk resistivity values, logarithmically scaled in Figure 3C to capture 100% of the absolute differences, and linearly scaled in Figure 3D to capture >99% of the relative differences. A linear scale is useful for revealing trends such as a doubling or halving of relative difference. From these colorbar scales we note that the subsurface at our site has the following characteristics: 1) resistivity generally varies between 2.5 and 320 Ωm throughout the sensed volume; 2) resistivity can exhibit day-to-day absolute changes in electrical resistivity as great as ±110 Ωm; and 3) resistivity can exhibit day-to-day relative changes in electrical resistivity spanning +1280% to -96%. We verified that this site is not subject to artificial forcing such as pumping (Stephen Labar, *pers. comm.*), and therefore the time-variable nature of this system is not the result of human activity. Since the sediments and bedrock in the subsurface do not move, day-to-day changes in electrical resistivity must be caused by the movement of subsurface water. In addition to vertical flow, horizontal flow (i.e. flow in or out of the tomographic plane) is hydraulically plausible.

3.4.2. Observations of Cyclical Features

We next turn to persistent features found in all of the tomograms. Three features are readily apparent; they are described using their dominant color and their interquartile range throughout the time sequence:

1) a top soil layer (green; 16-31 Ωm)

2) an intervening soil layer (blue; 3.2-7.3 Ωm)

3) a lowermost soil layer (orange; 18-51 Ωm)

The interface between the green and blue layer is sub-horizontal with gentle undulations. The interface between the blue and orange layer is concave downward.

Figure 3C, being a representative snapshot of the entire sequence, highlights that most of the snapshots contain large regions that typically experience very little change, as also illustrated in Figure 3D. Change is primarily concentrated in the top green layer near (x, z) = (58, -4) m and to a lesser degree near (x, z) = (66, -6) m.

3.4.3. Observations of Special Features

We now turn to those features in the tomograms where change is concentrated (Figures 4-5) and for convenience designate the concentrated areas of change with the following descriptive terms:

1) The House = the feature centered at (x, z) = (58, -4) m in the top green layer;

2) The Horns = the two regions immediately to the left and right of the House in the top green layer.

We use these shape-based terms for three reasons: to describe the shape of the feature simply and concisely; to use a memorable term (rather than e.g. “F-1”, “F-2”); to

avoid potential bias associated with terms that have geologic connotation (e.g. “shaft”, “pocket”, “tube”).

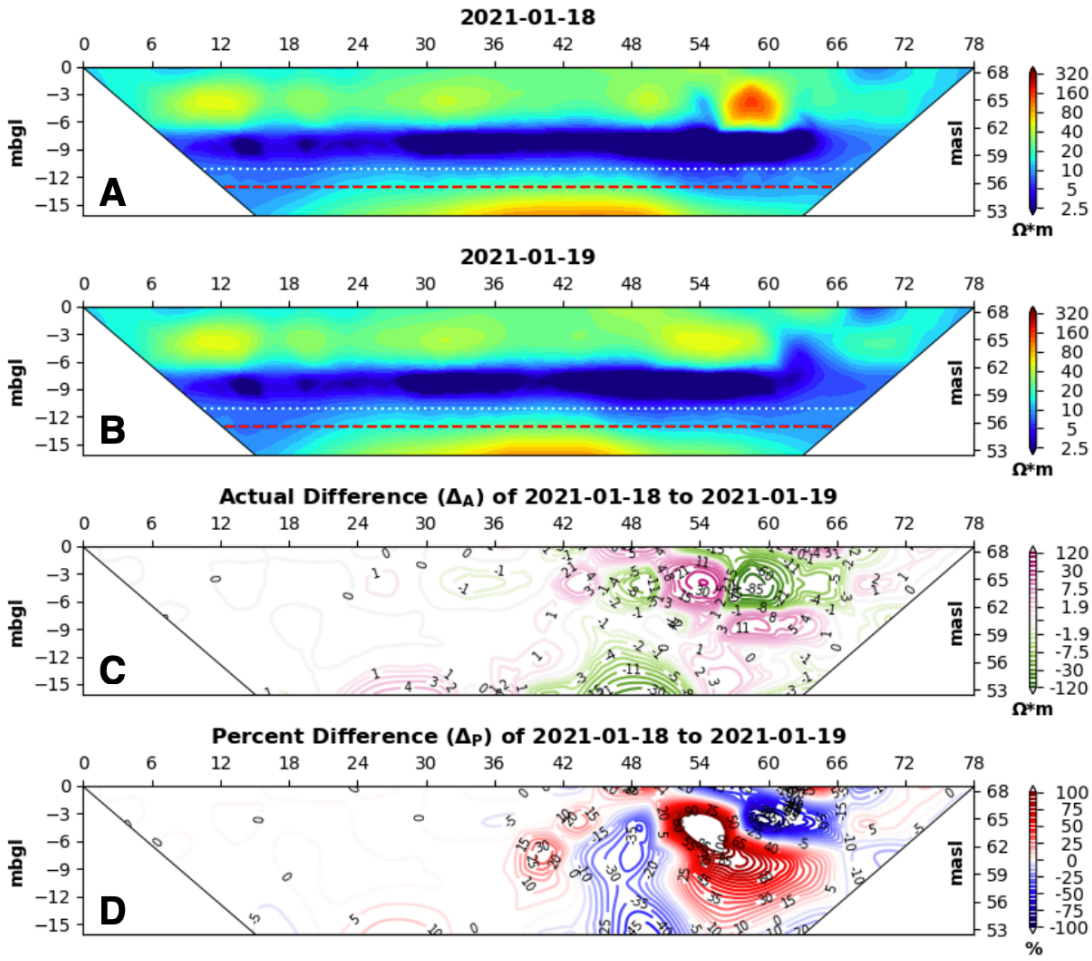

Figure 3.4. Time-lapse snapshot of 2021-01-18 to 2021-01-19 (both real, non-interpolated datasets) where the House vanishes in a single day.

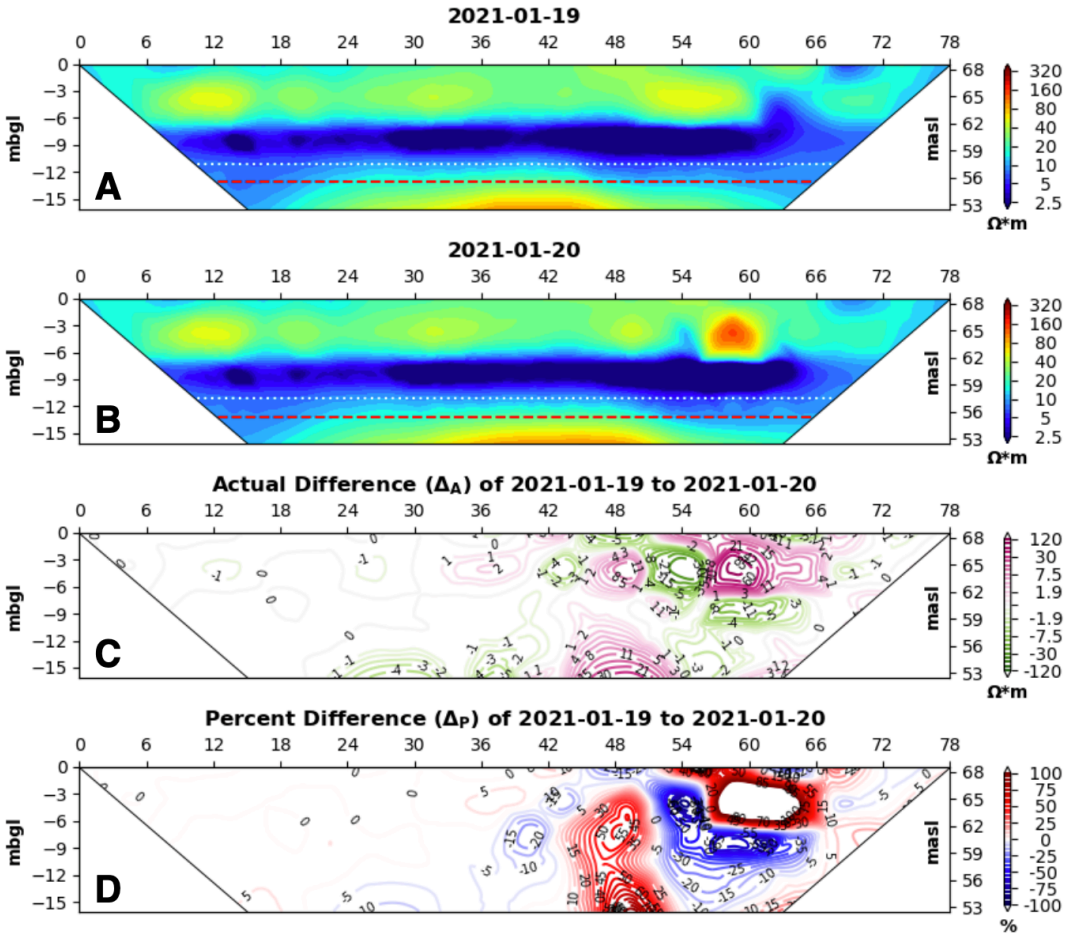

Figure 3.5. Time-lapse snapshot of 2021-01-19 to 2021-01-20 (both real, non-interpolated datasets) where the House reappears in a single day.

3.5. Discussion

We now describe a preliminary interpretation that identifies the location of a possible bidirectional preferential subsurface hydraulic pathway. In Figures 4-5, the location of the House undergoes rapid changes over three days. Similar rapid changes occur throughout the time-lapse survey. The most plausible interpretation of the cause of these changes is a pulse of water passing through the plane of the tomogram via a highly

permeable geomaterial (possibly sand). However, it remains to assess whether the House is simply an artifact of poor data collection, unstable modeling processes, or confounding environmental conditions. To investigate these possibilities, we subject the ERT data to three data appraisal analyses, namely robustness, sensitivity, and repeatability/reproducibility.

3.5.1. Robustness Analysis

The robustness analysis explores how an ERT tomogram is affected by a large change to the input dataset from which it is derived. We selected the sensor closest to the House (electrode #11) and removed all apparent resistivity readings associated with it. Per the dipole-dipole array setup, four electrodes are required to generate one reading, and so removing data associated with electrode #11 removed twenty-nine readings (out of 89 total). With the reduced dataset, we repeated the inversion (Figure 6). While the House *per se* was no longer visible, new features appeared further north in the top layer whose resistivity signatures also underwent significant fluctuations over the course of the time-lapse. Therefore, removing the sensor nearest the House (and simultaneously ~1/3 of the entire dataset) altered the location and reduced the intensity of a House-like feature, but did not completely remove its presence. This finding gives us a measure of confidence that the presence of a House-like feature is required to fit the full dataset.

We also analyzed for a possible instability of data associated with electrode #11 by comparing its percentage contributions to data and noise. The latter is defined as a signal that impedes measurement of the phenomena of interest and comprises 3.64 % of our data. We calculated this percentage from the number of noisy econs (“electrode

contributions", four of which compose one apparent-resistivity reading) compared to the total number of measured econs. As shown in Figure 6, the percent contributions to data (rendered in blue on the positive axis; values sum to 100 %) and noise (rendered in red on the negative axis; values sum to 100 %) are shown for each electrode. The differences (rendered in yellow; values sum to 0 %) between the two are rendered either above or below the percent contributions. Electrode #11 contributes 8.1 % of the data but only 7.7 % of the noise, therefore its +0.4 % contribution difference indicates that it does not generate disproportionately noisy measurements. From both analyses described above, we conclude that the House does not result from faulty data acquisition.

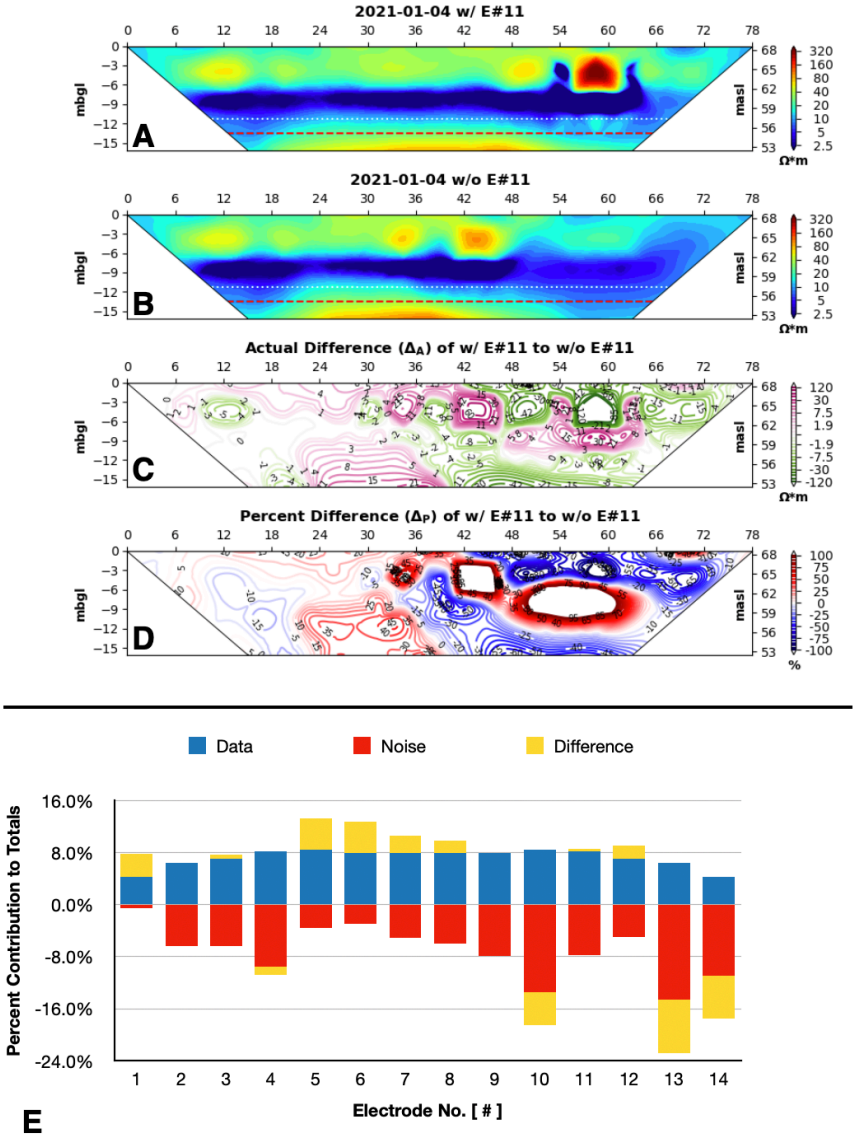

Figure 3.6. Robustness analysis on Electrode #11 (E#11). A Tomogram of 2021-01-04 rendered from complete dataset; House feature visible. B Tomogram of 2021-01-04 rendered from incomplete dataset without the data dependent on E#11; new, less well defined resistive House feature visible left of original location. C Actual difference of complete and incomplete datasets. D Percent difference of complete and incomplete datasets. E The percent contributions to data and noise.

3.5.2. Sensitivity Analysis

A sensitivity analysis investigates how an interpretation may be affected by small perturbations to the input data. We selected the ERT tomogram from 2020-12-24 in which the House was visible, and we made various perturbations to the nine apparent electrical resistivity readings associated with the House. The range in resistivities in this tomogram was 1.6-241 Ωm. We perturbed the central data point associated with the House in six different scenarios and then perturbed all nine apparent resistivities in three additional scenarios (Table 2). For scenarios with perturbations of 1% to -5%, only one point—the center point—was perturbed; for scenarios ±1% to ±5%, all nine points were perturbed (see Figure 7A). The perturbation values were generated randomly within defined ranges (see Figure 7B).

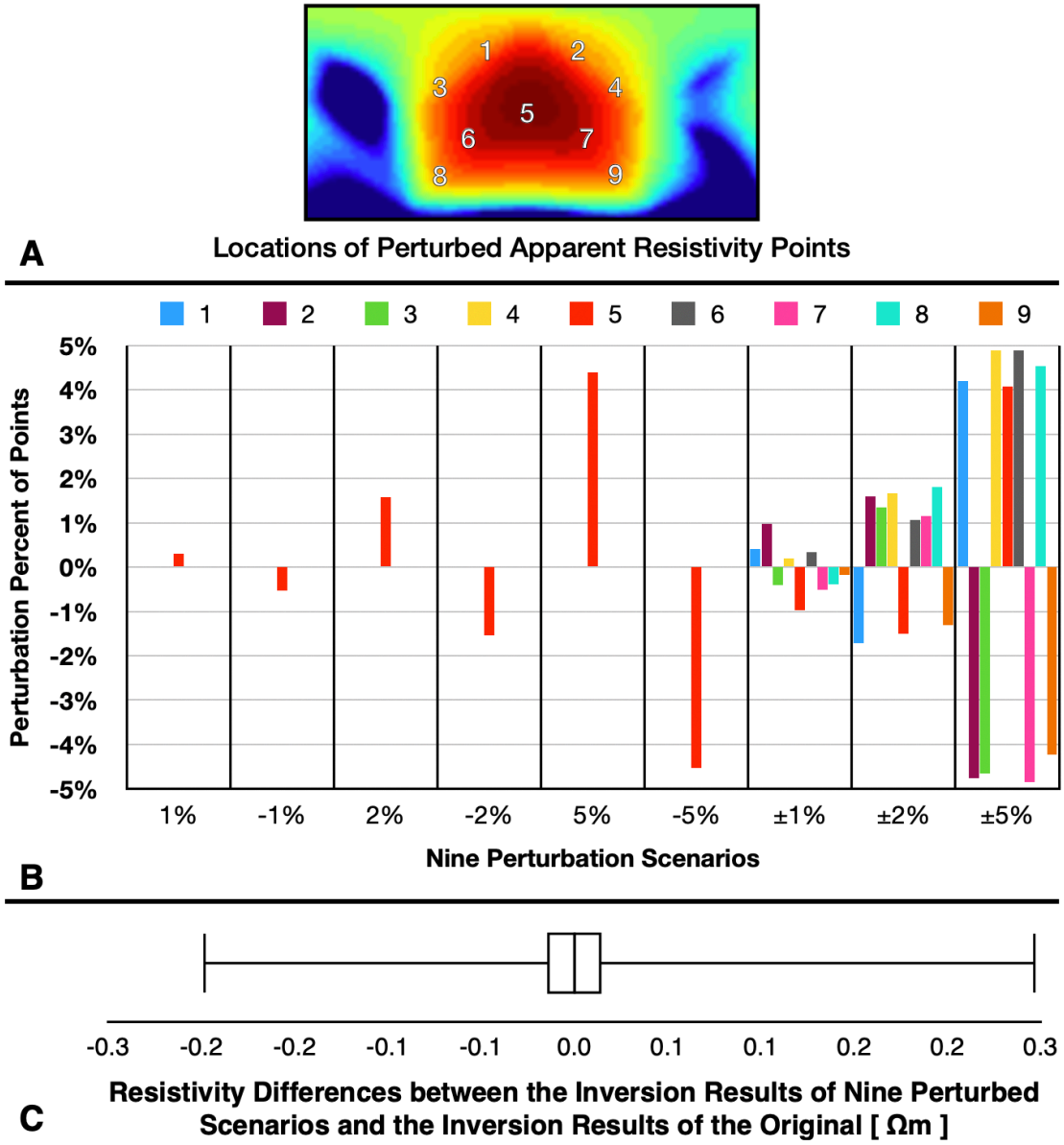

Figure 3.7. Sensitivity analysis on the House using nine perturbation scenarios of readings associated with the House. A Locations of the perturbed apparent resistivity points in relation to the House; non-perturbed points not shown. B Percentage perturbations of the nine points in nine separate scenarios. C Differences in inversion resistivities of these scenarios from those of the original are all equivalent and quantified in the box-and-whisker plot.

The sensitivity analysis revealed: 1) the RMS misfit values of the perturbed tomograms were the same as the original RMS of 7.63%, 2) the differences between the original and perturbed tomograms were essentially identical, and 3) the largest absolute resistivity difference in the perturbed and original tomograms is at the center of the House and is only 0.30 Ωm (see Figure 7C), i.e. three orders of magnitude less than the ~240 Ωm value at the center of the House. While we have not analyzed the sensitivity on other days, the absence of a significant effect amongst the nine considered scenarios suggests that the House feature is minimally affected by small perturbations to apparent resistivity readings. From this analysis, we conclude that the House is not an artifact of an unstable forward modeling or inversion process.

3.5.3. Repeatability and Reproducibility Analysis

A repeatability and reproducibility analysis investigates how an interpretation affected by ambient environmental conditions. We calculated the day-to-day repeatability of measured apparent resistivity over 5-consecutive-day periods during a dry and a wet spell. We also calculated the overall variation in the same quantity over the 61-day period of the surveys. As the dry spell-period, we chose two weeks during which the only two rainy days received 0.13 and 0.3 cm of precipitation, respectively. As the wet spell, we chose two weeks during which the total rain was greater than 2.5 cm, 1.96 cm of which fell in the three days immediately prior to the 5-day period. For the three intervals, we calculated the total apparent resistivity variation for each of the 89 datapoints, and then calculated the quartiles of those variations (Figure 8).

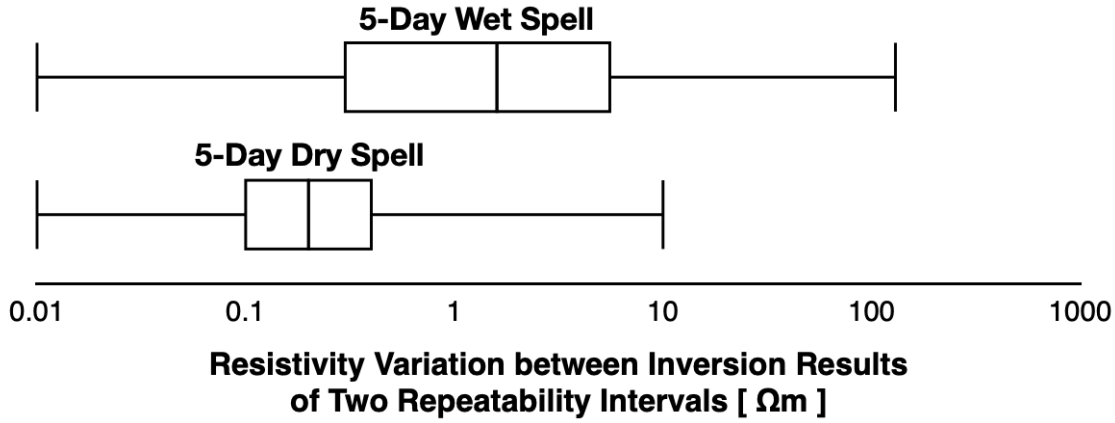

Figure 3.8. Repeatability and reproducibility analysis on electrical resistivity; these box-and-whisker plots compare the resistivity repeatability a 5 day dry spell compared to a 5 day wet spell and the reproducibility between them. While the minima for each are 0 Ωm, we plot the minima at 0.01 Ωm to accommodate the logarithmic scale.

We found the apparent resistivity during the dry spell to have a median variation of 0.2 Ωm, an interquartile range of 0.1 to 0.4 Ωm, and a maximum of 10 Ωm. The apparent resistivity during the wet spell had a median variation of 1.7 Ωm, an interquartile range of 0.4 to 5.7 Ωm, and a maximum of 130 Ωm. We therefore note: 1) the data are very repeatable during dry conditions (i.e. the dry spell) but not as repeatable during rainy conditions (i.e. the wet spell); 2) the reproducibility of the data between dry and wet spells is low; 3) subsurface resistivity can undergo significant variation in only a few days during time-varying hydrological conditions. These suggest that changing subsurface hydraulic conditions are responsible for the time-varying electrical resistivity of the House and Horns.

3.5.4. Forward Modelling

While the subsurface may contain distinct boundaries between geologic materials (e.g. between a loamy topsoil and an underlying clay layer or between a sand-dominated channel belt and an enclosing clay layer), an electrical resistivity tomogram tends to smooth out (blur) these distinct boundaries. This is a result of the transmission of electrical current through the spatially-variable material of the subsurface (see references in Methods). Forward modeling provides insight into how the smoothing process manifests itself in apparent resistivity readings, enabling a more accurate interpretation of the sensed subsurface volume. Forward modeling involves: 1) the specification of a subsurface model of electrical resistivity; and 2) the generation of a synthetic apparent resistivity pseudosection. Generation of a synthetic tomogram from the pseudosection can then be performed via the process of inversion. Our forward modeling and inversion exploration used the same parameter settings to those used to invert the original, measured data. An example of the forward modeling and the inversion of a synthetic resistivity structure is shown in Figure 9.

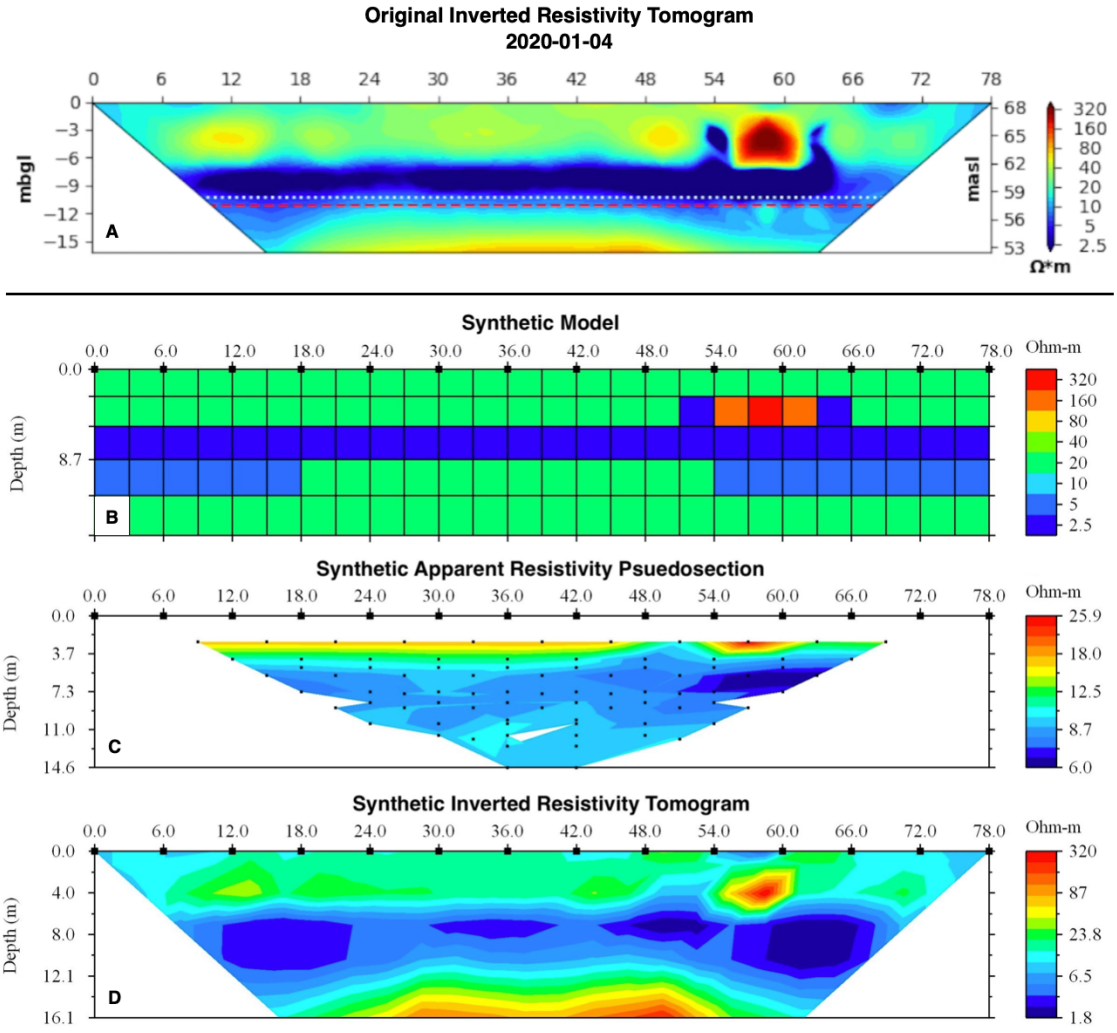

Figure 3.9. Process of forward modeling. A Original inverted resistivity tomogram from 2020-01-04. B Synthetic model used for forward modelling. C Resulting synthetic apparent resistivity pseudosection. D Synthetic inverted resistivity tomogram. Colorbar approximately equal to those used in time-lapse tomograms.

A synthetic Earth resistivity model was constructed based on the tomogram from the 2021-01-04 observations. The synthetic model has three layers along with a large resistive feature in the upper layer that is nested between conductive features of equal size. The synthetic tomogram generally captured the distribution of electrical resistivity

in the original tomogram including the House. From this, we can make several observations of how smooth model inversion affects visualization of the actual subsurface:

1) The original tomograms of the time-lapse (Figure 9A) **correctly** distinguish the three layers as seen in the synthetic tomogram (Figure 9D). The middle layer is more conductive than either the upper or lower layers, while the upper extent of the lowest layer rises towards the center of the synthetic tomogram.

2) The original tomograms **incorrectly** portray the lower layer having a higher resistivity (> 40 Ωm) than it likely has (note how the green lower layer in the Figure 9B synthetic model results in an orange lower layer in the 9D synthetic tomogram). This is not surprising considering the sensitivity of ERT diminishes with depth.

3) The original tomograms **correctly** distinguish between the resistive House feature and the conductive Horns, but it **incorrectly** distinguishes the left Horn as being larger and more prominent than the right one (note how the right Horn in the 9B synthetic model all but disappears in the 9D synthetic tomogram).

3.5.5. Precipitation Lag

Our interpretation of the vanishing and reappearance of the House is that it is caused by a pulse of fluid moving orthogonal to the plane of the tomogram. The two

immediate candidates for such an interpretation are a river water pulse and a rainwater pulse, respectively generated by a surge in river stage and a precipitation event. While a surge in river stage does occur on 2021-01-01 and peaks the following day, the peak river stage reaches an elevation corresponding to ~1.5m beneath the base of the House. Capillary action in the vadose zone could hypothetically transport river water upward through the sediments but could not transport river water an upward distance of 1.5 m

and then an additional 3 m distance to the top of the House in a single day (and retreat all the way back on the following day) (Lu and Likos, 2004).

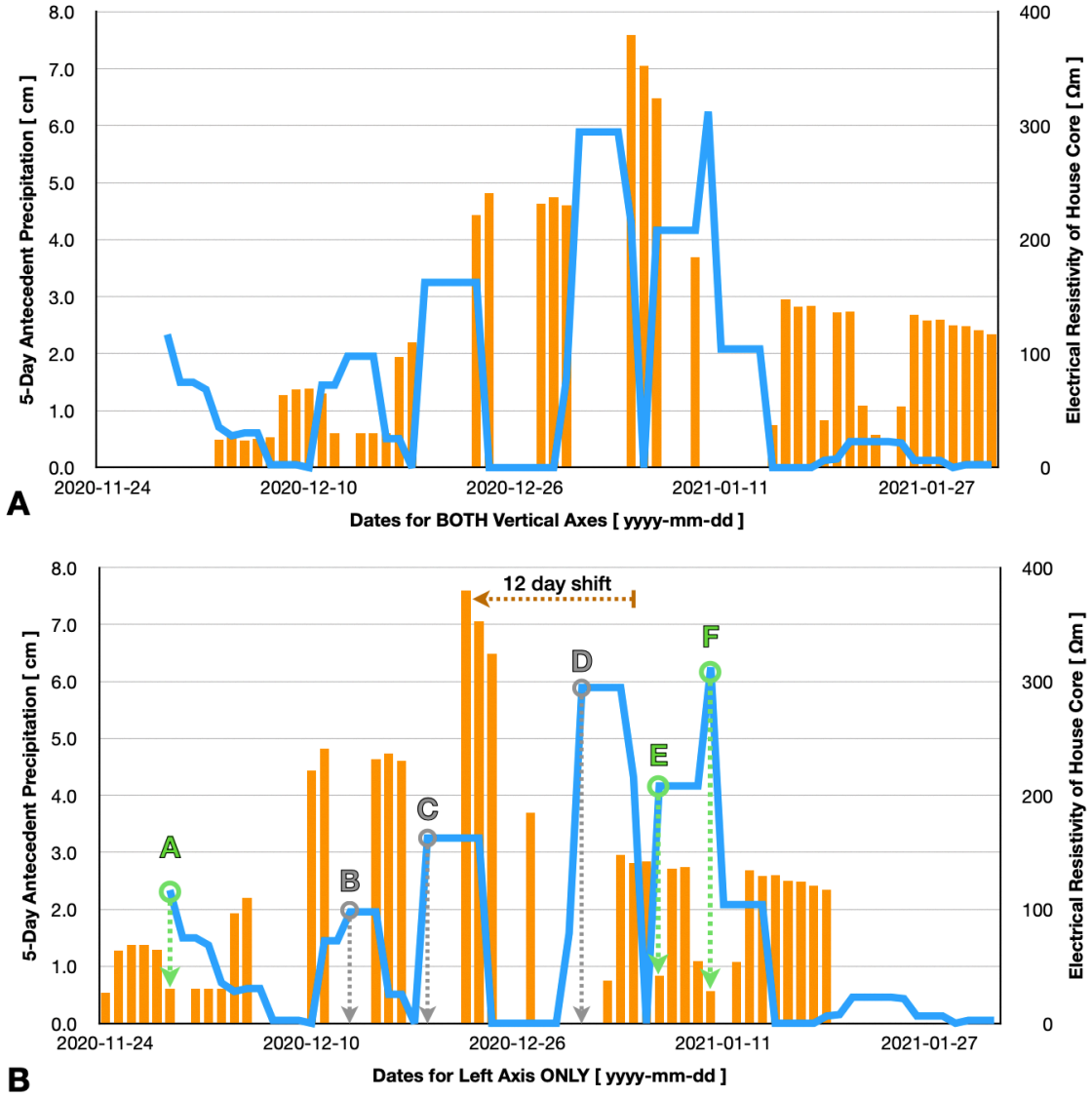

Figure 3.10. A Comparison of 5-day antecedent precipitation (blue line) and electrical resistivity (orange bars) at the core of the House. B Green arrows indicate days when antecedent precipitation exceeds 2.0 cm and the resistivity dropped 11-12 days later. Gray arrows indicate times when antecedent precipitation exceeds 2.0 cm but due to a data gap it cannot be stated whether resistivity dropped 11-12 days later or not.

We next consider a rainwater pulse. Comparison of the timing of precipitation amounts with fluctuations in resistivity at the center of the House (see Figure 10A) reveals three occasions (Figure 10B, points A, E, and F) in which the House vanishes (i.e. resistivity plummets) 11-12 days after the sum of precipitation over 5 days has exceeded 2 cm (see Figures 5 and 6 for an example of this vanishing; see Figure 10B for the timing of this vanishing). Five-day antecedent precipitation approaches or exceeds 2 cm three additional occasions (Figure 10B, points B, C, and D) during the timeframe of the ERT surveys, and at both 11 and 12 days after these precipitation events, ERT data gaps from lack of site access prevent us from telling whether the House vanishes then or not. From the consistent timing of the green arrows after precipitation exceeding 2 cm, we conclude that the repeated vanishing and reappearance of the House is caused by a pulse of rainwater passing through the plane of the tomogram at the location of the House.

We therefore have accomplished our first goal by identifying the location and timing of a hypothesized, preferential pathway capable of bidirectional flow using rigorously appraised geophysical data. The manner of its hypothesized flow in the opposite direction—making it a bidirectional pathway—will be considered next.

3.5.6. Final Interpretation

A geological scenario supported by the ERT time-lapse observations includes a tube of sand enclosed laterally by clay and underlain by the clay layer observed in three Texas Water Observatory well logs (Gretchen Miller, *pers. comm*.; Sedaghatdoost et al. 2019). This type of alluvial floodplain structure is consistent with a buried cutoff

meander channel (Figure 11A)—a "bypass of a meander loop in favor of a shorter path with the subsequent formation of an abandoned reach, called an oxbow lake" (Camporeale et al., 2008)—or a the throat of a buried crevasse splay (Figure 11B)—a "fan-shaped sediment [accumulation] that [is] deposited as the result of a breaching of the natural levee" (Davis, 2003). The throat is the location where the river breaches through its natural levee.

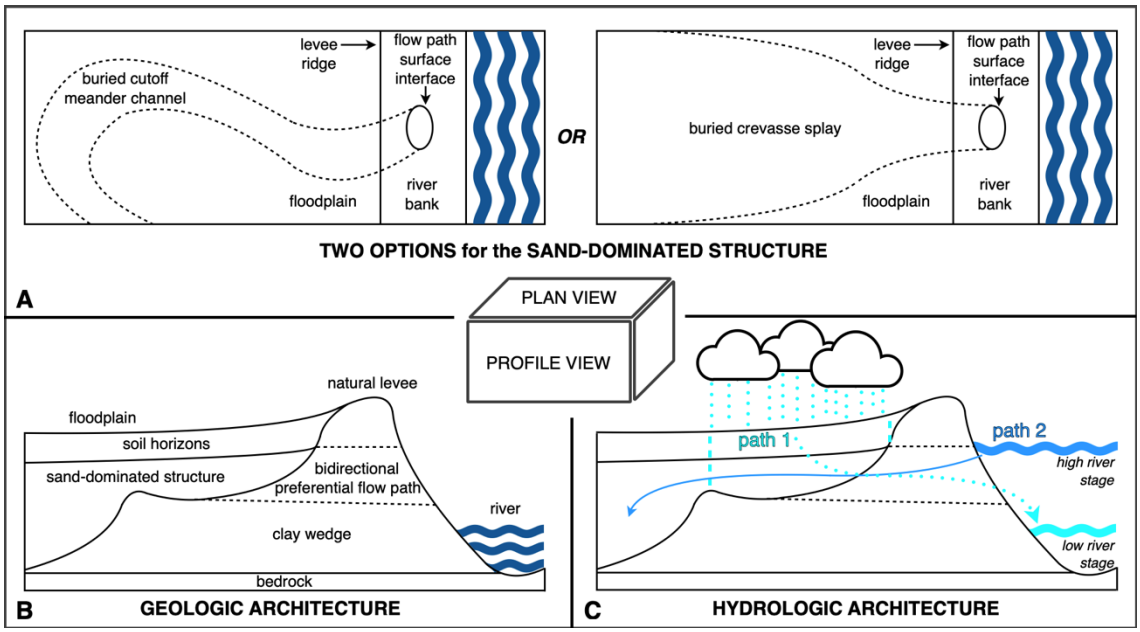

Figure 3.11. Conceptual model of hydrogeological architecture with a bidirectional preferential flow path; dimensions NOT to scale. A Plan views of the buried cutoff meander channel and buried crevasse splay, both in dashed lines and both sand-dominated structures. B Profile view of geologic architecture with the sand-dominated bidirectional preferential flow path. C Profile view of hydrologic architecture with the two flow paths; *path 1* shows meteoric water infiltrating into the subsurface and discharging out through the river bank out to a river stage lower than the flow path's surface interface; *path 2* shows river water infiltrating into the subsurface when river stage is higher than the flow path's (now submerged) surface interface and potentially recharging a shallow aquifer.

A hydrological scenario consistent with the ERT data is that rain water infiltrates and passes through either a sand-dominated buried cutoff meander channel or crevasse splay throat ("path 1" in Figure 11B). The rainwater would collect in the field to the west of the ERT survey line (Figure 2), infiltrate into the sand body (which could be either a cutoff meander channel (Figure 11A) or a crevasse splay (Figure 11B)), and then flow east through the plane of the ERT tomogram and discharge into the Brazos River. As rainwater passes through the plane of the tomogram, it would not simply increase or decrease the bulk resistivity of the involved geomaterials. Rather, the rainwater would moderate the resistivities of the geomaterials closer to its own value. We estimate the resistivity of the infiltrating rainwater at 20-40 Ωm, the background resistivity range into which the House and Horns fade for the following reason. Rainwater has a high initial electrical resistivity of ~60-2000 Ωm (Jonsson & Vonnegut 1991), and the on-site measurement of groundwater has a much lower resistivity of ~8-9 Ωm (Rhodes et al., 2018). As rainwater infiltrates the soil, dissolved ions from weathered soil minerals decrease the water's bulk electrical resistivity over time. Infiltrating rainwater which has not been in ground long (e.g. only the 11-12 days as noted in Figure 10) should be between those two ranges, which is how we estimated ~20-40 Ωm range for the rainwater pulse. The effect of this pulse on a relatively high resistivity, dry sand tube would be to decrease the bulk resistivity as the pulse saturates the pores. In contrast, a rain pulse would increase the bulk resistivity of a relatively low resistivity, groundwater-saturated clay lining.

Regardless of whether the House is a cross-section of a buried cutoff meander channel or a crevasse splay, both would act as a preferential pathway of water away from the main trunk of the river and into the floodplain during their formation ("path 2" in Figure 11C). At the present time however, this sand-dominated structure acts as preferential pathway toward the modern Brazos River. Therefore, to the previous list of hydrogeologic examples of bidirectional flow—meteoric water in the vadose zone, groundwater in forested slopes, and bank storage in riverbanks—we add infiltrating rainwater pulses in buried sand-dominated structures (such as cutoff meander channels or crevasse splays) that cut a preferential pathway between a floodplain's interior and its river.

We therefore have accomplished our second goal by developing a hydrogeological explanation for the existence of a bidirectional preferential pathway.

3.5.7. Implications and Future Research

While the structure and composition of alluvial floodplains is well known to be labyrinthine (e.g. Hajek et al. 2010; Jerolmack and Paola 2007; Martinius 2000), the present research improves our understanding of preferential pathways that can occur between a river and inland, shallow aquifers. Consider the following analogy. Medical professionals are familiar with the digestive system and are aware it works in both directions (i.e. stomach to mouth and vice versa). Similarly, to restore, decontaminate, and steward the aquifers, groundwater managers (scientists, engineers, or public officials) should be aware of the locations, physical dimensions and frequency over which river water and groundwater mix along alluvial floodplains. The medical

professional keeps in mind the entire physiological system and its surroundings; likewise the groundwater manager should keep in mind the ambient environmental, anthropogenic and ecological site context. The improved understanding benefits investigators modeling processes operating over both geologic and human time scales.

Over geologic time (thousands of years), floodwaters may break out of the banks of river through a breach in the bounding clay wedges and deposit sediments as a crevasse splay, forming a sand-dominated zone. Then, after burial of the crevasse splay, infiltrating rainwater preferentially flows back toward the river. River action may also cut through meander channels, cutting off meander bends and leaving them to be filled in with sediments by later floodwater events. Then, after burial of the cutoff meander channel, infiltrating rainwater preferentially flows back toward the river out of the riverbanks. In either case, this study demonstrates the important role of floodplain heterogeneity in the exchange of water, sediments, and contaminants between the river channel and the floodplain, specifically by bidirectional preferential pathways.

Over a human lifetime (80 years), infiltrating rainwater may collect in buried cutoff meander channels or crevasse splays—incorporating surface contaminants—and preferentially flow out of a spring into the river. These buried preferential flow features may allow high river stage events that do not breach the top of the channel drive river water into the subsurface of the floodplain—also incorporating surface contaminants. Therefore, floodplain heterogeneity is a controlling factor in the distribution of water,

sediments, and contaminants.

For geophysicists working in alluvial floodplain, identifying and characterizing bidirectional preferential pathways in alluvial floodplains must satisfy two conditions. The first is time-lapse data acquired during changing environmental conditions. Without a time-lapse, individual surveys could miss the times when the sand-dominated structure is relatively dry and visible as a high resistivity feature. Without precipitation events or a sufficiently high river stage, surveys would miss the sand-dominated structure conducting a pulse of water and moderating its resistivity.

Directions for future studies include: 1) hydrological investigations, using pump and tracer tests to determine the hydraulic properties of putative buried cutoff meander channels or crevasse splays; 2) geomorphological investigations to determine whether indicators of water-transport bidirectionality leave a surface signature that can be identified without labor-intensive geophysical studies; and 3) longer geophysical time series, to observe the temporal dynamics of the system through varying seasons.

3.6. Conclusions

At the basis of sustainable, scientific management of shallow groundwater resources are hydrogeological models. These models allow us to: 1) predict future hydrogeological conditions given specific starting conditions; 2) determine whether future conditions are desirable; and 3) make adjustments in the real world to achieve desired future conditions. It is consequently vital that model predictions are accurate.

Our research indicates that bidirectional preferential flow can occur in subsurface structures such as buried cutoff meander channels or crevasse splays, and that bidirectional preferential flow exerts an important control on the regulation and distribution of water and sediments. Therefore, an accurate groundwater model should include the bidirectional preferential flow occurring in such structures. Using models based on such knowledge, groundwater managers will be better prepared to sustainably steward shallow groundwater resources for current and future generations.

3.7. References

Bosch, D.D., Sheridan, J.M., and Lowrance, R.R. (1996) Hydraulic gradients and flow rates of a shallow coastal plain aquifer in a forested riparian buffer. Trans. ASAE, 39 (3), 865–871.

Bridge, J.S. (2009) Rivers and Floodplains: Forms, Processes, and Sedimentary Record, John Wiley & Sons.

Camporeale, C., Perucca, E., and Ridolfi, L. (2008) Significance of cutoff in meandering river dynamics. Journal of Geophysical Research: Earth Surface, 113 (F1).

Clark, B.R., Hart, R.M., and Gurdak, J.J., (2011) Groundwater availability of the Mississippi embayment. U.S. Geological Survey Professional Paper 1785.

Dafny, E., and Silburn, D.M. (2014) The hydrogeology of the Condamine River Alluvial Aquifer, Australia: a critical assessment. Hydrogeol. J., 22 (3), 705–727.

Davis, R.A. (2003) Coastal Geology, in Encyclopedia of Physical Science and Technology (Third Edition) (eds.Meyers, R.A.), Academic Press, New York, pp. 123–153.

Everett M. 2013. Near-surface applied geophysics. Cambridge, UK: Cambridge University Press

Furman, A., Ferré, T.P.A., and Warrick, A.W. (2003) A Sensitivity Analysis of Electrical Resistivity Tomography Array Types Using Analytical Element Modeling. Vadose Zone Journal, 2 (3), 416–423.

Ghazavi, R., Thomas, Z., Hamon, Y., and Merot, P. (2011) Soil water movement under a bottomland hedgerow during contrasting meteorological conditions. Hydrological Processes, 25 (9), 1431–1442.

Gleeson, T., Cuthbert, M., Ferguson, G., and Perrone, D. (2020) Global Groundwater Sustainability, Resources, and Systems in the Anthropocene, in Annual Review of Earth and Planetary Sciences, Vol 48, 2020, vol. 48, Annual Reviews, Palo Alto, pp. 431–463.

Griebler, C., and Avramov, M. (2015) Groundwater ecosystem services: a review. Freshw. Sci., 34 (1), 355–367.

Hajek E. A., Heller P. L., and Sheets B. A. 2010. Significance of channel-belt clustering in alluvial basins. Geology, 38(6), 535-538.

Jerolmack D. J. and Paola C. 2007. Complexity in a cellular model of river avulsion. Geomorphology, Special Issue 91(3-4), 259-270.

Klove, B., Ala-Aho, P., Bertrand, G., Gurdak, J.J., Kupfersberger, H., Kvaerner, J., Muotka, T., Mykra, H., Preda, E., Rossi, P., Uvo, C.B., Velasco, E., and Pulido-Velazquez, M. (2014) Climate change impacts on groundwater and dependent ecosystems. J. Hydrol., 518, 250–266.

Loke M. H. 1999. Electrical imaging surveys for environmental and engineering studies: a practical guide to 2-D and 3-D surveys. https://urldefense.com/v3/__https://www.aarhusgeosoftware.dk__;!!KwNVnqRv!RiVLnEsgJgJsUkGy2ApB0CccEj6nd7F9greAKlO7_fyI1HCFwhZG25k35X_9VcDmDSgqd9tcKrKPGA$

Lu, N., and Likos, W.J. (2004) Rate of Capillary Rise in Soil. J. Geotech. Geoenviron. Eng., 130 (6), 646–650.

Macdonald, D.M., Dixon, A.J., and Gooddy, D.C. (2018) Water and nitrate exchange between a managed river and peri-urban floodplain aquifer: Quantification and management implications. Ecol. Eng., 123, 226–237.

Martin, J.M., Everett, M.E., and Knappett, P.S.K. (2021) Coupling hydrogeophysics with hydrodynamic modelling to infer subsurface hydraulic architecture of an alluvial floodplain. Near Surf. Geophys., 19 (3), 335–352.

Martinius A. W. 2000. Labyrinthine facies architecture of the Tortola fluvial system and controls on deposition (Late Oligocene - Early Miocene, Loranca Basin, Spain). Journal of Sedimentary Rock, 70(4), 850-867.

Menichino, G.T., and Hester, E.T. (2015) The effect of macropores on bi-directional hydrologic exchange between a stream channel and riparian groundwater. J. Hydrol., 529, 830–842.

Nanson, G.C., and Croke, J.C. (1992) A genetic classification of floodplains. Geomorphology, 4 (6), 459–486.

National Oceanic & Atmospheric Administration (NOAA). 2021. Normals Annual/Seasonal Station Details for GHCND:USW00003904. https://www.ncdc.noaa.gov/cdo-web/datasets/NORMAL_ANN/stations/GHCND:USW00003904/detail

Rhodes K. A., Proffitt T., Rowley T., Knappett P. S. K., Montiel D., Dimova N., Tebo D. and Miller G. R. 2017. The importance of bank storage in supplying baseflow to rivers flowing through compartmentalized, alluvial aquifers. Water Resources Research, 53(12), 10539-10557.

Scheidegger, J.M., Jackson, C.R., Muddu, S., Tomer, S.K., and Filgueira, R. (2021) Integration of 2D Lateral Groundwater Flow into the Variable Infiltration Capacity (VIC) Model and Effects on Simulated Fluxes for Different Grid Resolutions and Aquifer Diffusivities. Water, 13 (5), 663.

Sedaghatdoost A., Mohanty B., and Huang Y. (2019) The effect of heterogeneities in soil physical and chemical properties on redox biogeochemistry in subsurface soils. American Geophysical Union Fall Meeting 2019, Expanded Abstracts, San Francisco, United States, B33E-08.

Texas Water Development Board (TWDB). (2017) Groundwater availability model for the Brazos River Alluvium. INTERA Inc. https://www.twdb.texas.gov/groundwater/models/gam/bzrv/bzrv.asp

United States Department of Agriculture (USDA). 2014. Soil Survey of Burleson County, Texas. https://www.nrcs.usda.gov/Internet/FSE_MANUSCRIPTS/texas/TX051/0/Burleson.pdf

United States Geological Survey (USGS). 2021. Brazos River at SH-21 near Bryan, TX. https://waterdata.usgs.gov/nwis/uv?site_no=08108700

Xiang, X., Li, Q., Khan, S., and Khalaf, O.I. (2021) Urban water resource management for sustainable environment planning using artificial intelligence techniques. Environ. Impact Assess. Rev., 86, 106515.

Zonge K., Wynn J. and Urquhart S. 2005. Resistivity, induced polarization, and complex resistivity. In D.K. Butler (Ed.), Near Surface Geophysics (pp. 265-300). Tulsa, OK: Society of Exploration Geophysicists.

4. MEASURING DIAGNOSTIC PROFICIENCY OF THE HUMAN ELEMENT: A CASE STUDY USING A GPR SURVEY FOR UNMARKED GRAVES IN A HISTORIC AFRICAN-AMERICAN CEMETERY

4.1. Introduction

Management of cemeteries in the 21st century has become increasingly necessary and valuable (Berezowski et al, 2021; Dick et al., 2017; Sherrod et al. 2020). As cemeteries become increasingly full, identifying open spaces and unmarked graves becomes increasingly necessary, and as non-invasive archaeological methods such as ground-penetrating radar (GPR) become increasingly proficient, cemeteries become increasingly valuable as "useful repositories of archaeological information" (Berezowski et al., 2021). That latter point is particularly true of 19-20th century African-American cemeteries for slaves and freedmen in the United States.

In the 1960's, America began its attempt at desegregation, and the new opportunities for African-Americans were accompanied by migrations from their previous communities (Archie Rison, pers. comm.; Spera et al., 2022). Those communities had collectively maintained their own cemeteries, but following the migrations, those cemeteries often fell into neglect. Geological processes buried, washed away, or degraded existing gravestones, botanical process hid others, and vandalism removed more. Other burials were lost due to lack of a gravestone (or simply having a wooden marker that rapidly decomposed) caused by the prohibitive expense of stone. Modern efforts by community stakeholders have restored existing gravestones and

landscaping of many of these cemeteries, but identification of unmarked graves remains an ongoing issue.

Typically, the proficiency of GPR (and other non-invasive methods) in identifying unmarked graves is considered solely in terms of the technological development of hardware, deployment configuration, and software. Much impressive work has been done and detailed in the literature about the best practices for selecting antenna shape and frequency (Dick et al., 2017; Zhao et al., 2021), whether to collect 2D vs. 2.5D vs 3D datasets (Sarris et al. 2018), visualization (Trinks and Hinterleitner, 2020; Yuan et al., 2018) and post-acquisition processing methods (Lu et al., 2020; Manataki et al., 2021), and whether to apply classification schemes using textural attributes (Zhao et al., 2013; Zhao et al., 2015) or hierarchical clustering with Gaussian mixture modeling (Bijamov et. al., 2014).

Underpinning the hardware, the deployment configurations, and the software however is the vital (though unfortunately overlooked) human element. If all graves had a unique radar signature and there was consequently zero uncertainty, this element would not exist; geophysicists would simply survey a few marked graves, determine the unique signature, and apply it to all searches for unmarked graves. But due to the complexity of soil composition, structure, and moisture content, of burial type, depth, and age, and of decomposition (Hansen et al., 2014), marked graves are characterized by a wide range of radar signatures (both individually and in aggregate). Consequently attempting to identify unmarked graves involves non-negligible uncertainty. Furthermore, we cannot reduce this uncertainty to zero because geophysical surveys are

inherently limited by available time, money, hardware, software, and site access in addition to cultural sensitivities and legal constraints. These limitations prevent the ground-truthing of every potential target. So in the midst of this non-negligible and non-removable uncertainty, a "go/no-go" decision for further investigation must be made by the "human in the loop".

Ultimately, decisions may be made by a geophysics practitioner, a software developer, or an instrument manufacturer. The basis for that decision may simply be a practitioner's expertise, a software developer's more quantitative confidence threshold derived from explicit numerical attributes or neural networks (Harkat et al., 2019), or an instrument manufacturer's field tested instrument design and parameter combinations. But whether resident only in the practitioner's mind, encoded in the software, or built explicitly into the hardware, the human element and all of its biases remain an important factor in the search for unmarked graves.

Which begs the question: how can the proficiency of the GPR practitioner be measured and improved?

To answer, consider the following medical analogy. A physician receives the results of some diagnostic test, say a series of computed tomography (CT) scans, and is asked, "Which of these patients have cancerous tumors?" The physician's response for each scan may be either positive or negative, and a subsequent biopsy of each patient may either verify or falsify that response. Determining the proficiency of the physician may be evaluated by calculating the physician's true-positive, true-negative, false-

positive (i.e. “false alarm”), and false-negative (i.e. “miss”) percentages (Metz, 1978; Bijamov et. al., 2014). Such measurement and improvement are not just concepts in medicine but are also found in studies developing training methods for detecting unexploded ordinance (Jayatilaka et al., 2018).

In like manner, the GPR practitioner can view a livestream of GPR data while surveying a historic cemetery suspected to have unmarked graves. While viewing the data livestream, the practitioner can classify a surveyed location as:

- Positive, or “yes, there is an unmarked grave here”
- Negative, or “no, there is not an unmarked grave here”

Subsequent data analysis can measure the fraction of correct classifications by using indicators for known on-site marked graves as a proxy for ground-truthing. After calculating an initial proficiency rating via the true-positive, true-negative, false-positive, and false-negative percentages, the practitioner can survey a second cemetery to test proficiency. We hypothesize that proficiency will improve between the first and second cemetery for this reason: the measurement of initial proficiency exposes the direction in which the aggregate of human bias tilts and may be compensated for accordingly.

The goals of this study are: 1) to classify whether observed radar signatures indicate unmarked graves in a GPR dataset of a 19-20th century African-American cemetery; 2) to verify or falsify the classifications using indicators of known graves at the same site as a proxy for ground-truthing; 3) to evaluate proficiency and subsequently

its improvement when practiced on a second cemetery; 4) to enable proficient interpretation of the subsurface for community stakeholders, and; 5) to highlight the implications of the research on the broader practice of geophysics.

In the following sections of this paper, we briefly discuss the characteristics of the fieldwork sites, the fundamentals of ground-penetrating radar, the collection of the datasets, and the development, training, and testing required to establish indicators of known graves. We describe and evaluate an operator's proficiency at the first and second cemeteries, highlight the implications of this work on the practice of geophysics, make a useful interpretation of the subsurface, and note some areas for future research.

4.2. Field Sites

To collect the datasets for our research and to investigate the locations of ~45 unmarked graves whose burials are noted in historical church records (Sherry Frisk, pers. comm.), we conducted a 4-day, 2851 m^2, 400-MHz GPR joint research and community service survey at the historic African-American Salem Cemetery, now situated on the grounds of the City Cemetery of College Station, TX. We later practiced the conclusions of our research in a 1-day, 187 m^2, 400-MHz survey at the historic Old Danville-Shepherd Hill (ODSH) Cemetery in Willis, TX.

The Salem Cemetery lies on Boonville series soil that is "very deep, somewhat poorly drained very slowly permeable soils on uplands…derived from weathered Yegua materials" (USDA, 2002). The ODSH Cemetery lies on Latium clay that is "very deep,

well drained, very slowly permeable soils…derived from weakly consolidated calcareous clays and marls…on gently sloping to moderately steep uplands" (USDA, 1997). Both of these soils are clay-rich, the soil type in which GPR is least effective, and this helps ensure the robustness of our results on other sites.

The Salem Cemetery was used as the burial ground for a local African-American congregation between the 19th and 20th centuries (Sherry Frisk, pers. comm.). The ODSH Cemetery has been used as the burial ground for non-Catholics or non-members of the Danville family (i.e. both African-Americans and non-African-Americans). The Catholic and Danville family cemeteries are to the east of ODSH. This cemetery is still accepting new burials (Stacy Callihan, pers. comm.).

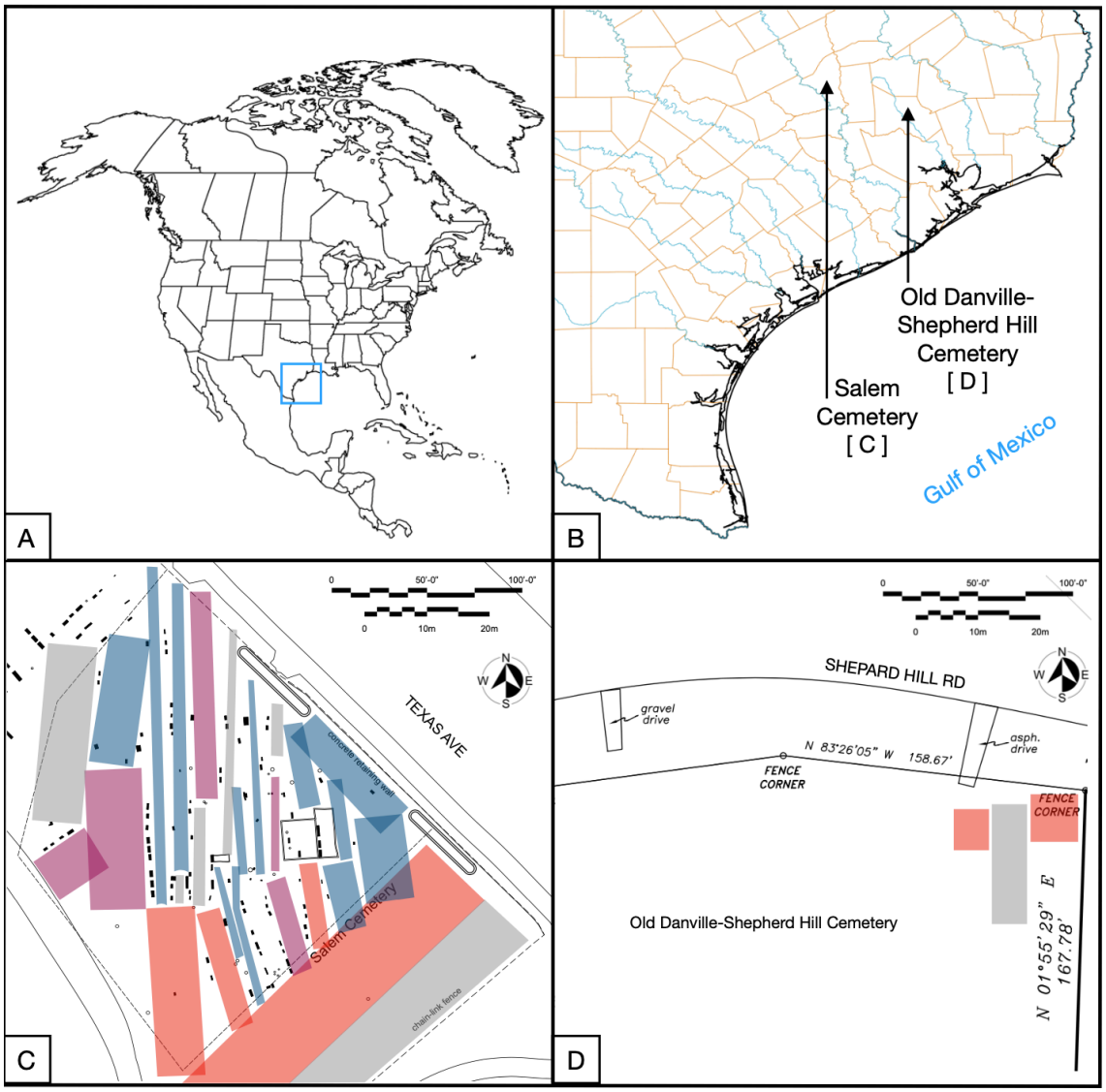

Figure 4.1. Context and site maps. A North American continent; blue square = subfigure B. B Coastal plains of Texas and the Gulf of Mexico. Arrows point to the two field sites. C Map of Salem Cemetery; black rectangles are gravestones, and black circles are trees. Shaped sections surveyed with GPR; purple = survey used in both training and testing datasets, red = survey used in training dataset, blue = survey used in testing dataset, gray = survey used in neither training nor testing datasets. D Map of the Old Danville-Shepherd Hill Cemetery. Same color scheme as Salem.

4.3. Methods

4.3.1. Ground-Penetrating Radar

The basic principles of GPR acquisition, analysis, and interpretation for archaeological investigations were pioneered by Imai et al. (1987) and recently reviewed by Bereowski et al. (2021). In short, the transmitting antenna of a GPR system transmits electromagnetic energy into the subsurface, which reflects off subsurface changes in dielectric permittivity. The receiving antenna of a GPR system detects the reflected energy as a vertical 1D amplitude trace known as an A-scan (Figure 2A; three A-scans shown side by side), showing travel time vs. amplitude (Annan, 2009). Stitching together the 1D amplitude traces creates a 2D vertical profile known as a B-scan (Figure 2B) and stitching together 2D profiles, at a given two-way travel time, creates a 2D horizontal time-slice map known as a C-scan (Figure 2C).

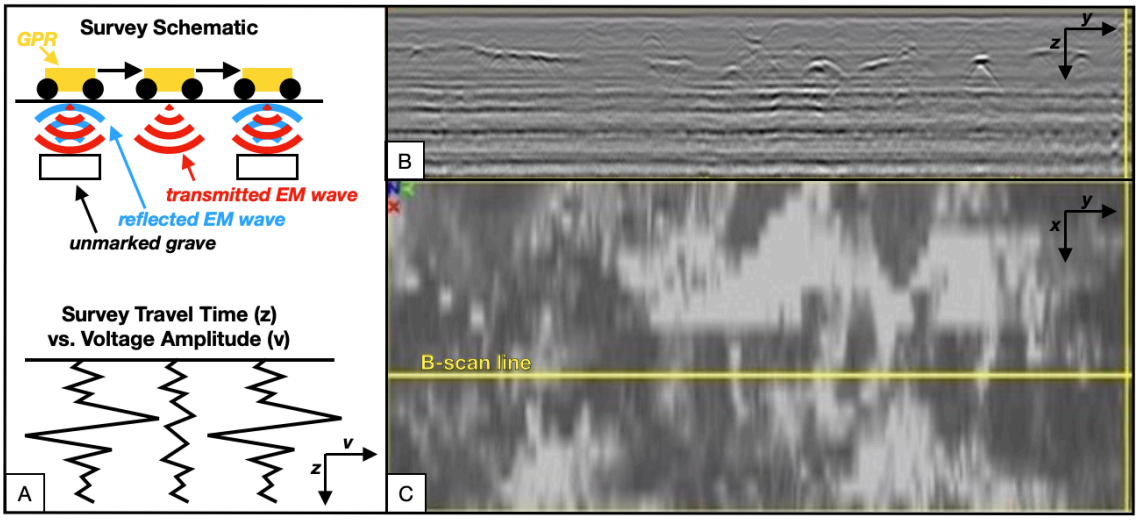

Figure 4.2. Fundamentals of GPR. **A** Upper image shows a schematic of a mobile GPR antenna (in yellow) transmitting an EM wave into the subsurface (in red) and receiving EM waves (in blue) reflecting off subsurface objects, such as unmarked graves (in black); lower image shows the corresponding 1D signals, particularly the higher

amplitudes when the transmitted EM wave encounters a contrast in dielectric constant in the subsurface. **B** Vertical B-scan. **C** Horizontal C-scan; horizontal yellow line shows the location of the vertical B-scan in subfigure B.

A major benefit of GPR is that it can collect an A-scan every few cm (or even less than one cm, if surveyed slowly enough), resulting in a dense dataset along the survey line. For archaeological investigations, each subsequent survey line is typically a few tens of cm away, resulting in a dataset that has a higher resolution along the survey line than between survey lines. This acquisition geometry is called a 2.5D survey, which is the type undertaken at our field sites. To help ensure the robustness of our results, we used no GPR processing techniques or filters other than an automatic gain control which was activated before the survey began—i.e. no standard processing steps such as DEWOW, high-pass/low-pass/frequency filtering, or migration.

Due to the irregularly spaced gravestones at the Salem Cemetery, we could not systematically survey the site and instead collected an irregular mosaic of GPR surveys ranging from a few to tens of m long and one to almost ten m wide (Figure 1C). Square plots at the Old Danville-Shepherd Hill Cemetery allowed us to make a regular mosaic of surveys (Figure 1D).

4.3.2. Indicator Development, Training, and Testing

In the medical analogy, the physician's positive or negative diagnosis of a non-invasive CT scans can be verified or falsified by subsequent invasive biopsy. In geophysics the equivalent to biopsy is ground-truth, i.e. an excavation. Unfortunately, excavation of tens to hundreds of targets is both cost and time prohibitive (and in the

case of unmarked graves, usually undesirable and/or not permitted). We therefore developed a novel, rapid proxy for ground-truthing.

First, we extracted three subsets of the Salem Cemetery GPR data: the areas beneath gravestones (known graves), the area immediately surrounding trees (known tree roots), and other ground (undisturbed soil, lacking an evident subsurface target). We split each of these data subsets into training (red and purple sections in Figure 1C and 1D) and testing datasets (blue and purple sections in Figure 1C and 1D). Of the total area surveyed at Salem, a partially overlapping 51.5% and 38.7% of the area was used for training and testing, respectively. In total, 75.0% of the Salem data for the training and testing datasets. In addition to this, we used 49.9% of the ODSH dataset specifically for the training dataset for identifying tree roots.

During training, common characteristics, or "GPR features" as they are often called, for each type of subsurface object were catalogued. We then evaluated the ability of the common characteristics to correctly classify the known graves, tree roots, and undisturbed soil in the testing datasets. Common characteristics that frequently appeared in both the training and testing datasets were retained and renamed "indicators"; others were discarded.

Next, we estimated the confidence that a suspected unmarked grave is in fact an unmarked grave by a three-step process. We first calculated the prevalence of the indicators or indicator sets (some subsurface objects manifest as multiple indicators) in the known subsurface objects from the training and testing datasets. We then compared the prevalence of these indicators between the training and testing datasets. If an

indicator appeared much more frequently in the training dataset than it does in the testing dataset, then it could not be trusted to be valid across the site. If however an indicator appeared much more frequently in the testing dataset than it does in the training dataset, then training was deemed incomplete. For our purposes, we used a moderate 30% difference as the threshold. In other words, indicators or indicator combinations with >30% difference in prevalence between the training and testing datasets were not used to make a positive classification of subsurface objects. We finally calculated our confidence estimate using the following equation:

$$C_{est} = 1 - |P_{training} - P_{testing}|, \text{ where } \left|P_{training} - P_{testing}\right| < 0.30 \quad \text{(Eq. 1)}$$

where C_{est} is the estimated confidence, $P_{training}$ is the prevalence of an indicator or indicator set in the training dataset, and $P_{testing}$ is the prevalence of an indicator or indicator set in the testing dataset. This confidence estimate C_{est} lets us calculate a quantitative measure that the target is an unmarked grave.

4.3.3. Proficiency Calculations

We measure our in-field classification proficiency, both at Salem and ODSH Cemeteries, with two-way contingency tables (true-positive, true-negative, false-positive, and false-negative percentages), using the aforementioned indicators as a proxy for ground-truthing. While false alarms and misses are almost inevitable, balancing the two prevents an overabundance of either. Tolerating more false alarms means accepting greater risk in: 1) overestimating the number of unmarked graves and; 2) preventing new burials in ground not actually containing a grave. Tolerating more misses means greater risk in: 1) inadequately memorializing past generations and; 2) allowing new burials in

ground already containing a grave. Therefore, an improvement in proficiency includes not just an increase of correct classifications between the first and second cemeteries, but also the achievement of a balanced trade-off between false alarms and misses.

4.4. Results

4.4.1. Initial Classifications

During data collection, the GPR equipment showed a B-scan livestream. We used the livestream to make in-field classifications of 55 potential unmarked graves at the Salem Cemetery and 2 potential unmarked graves at the ODSH Cemetery (Figure 3).

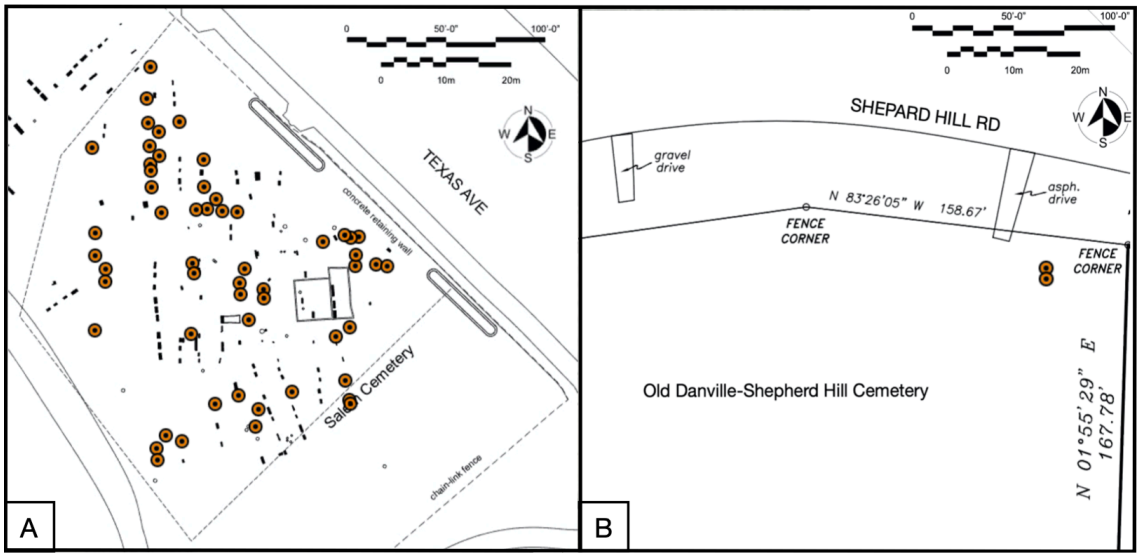

Figure 4.3. Locations of in-field classification of potential unmarked graves (orange circles). A Salem Cemetery. B Old Danville-Shepherd Hill Cemetery.

4.4.2. Indicators and Indicator Sets

The Salem survey covered areas known to contain graves, tree roots, and

undisturbed soil. Six initial common radar characteristics for known graves were reduced to five indicators, twelve for roots were reduced to five, and six for soil were reduced to four. Figure 4 shows typical images of these radar indicators along with a nomenclature.

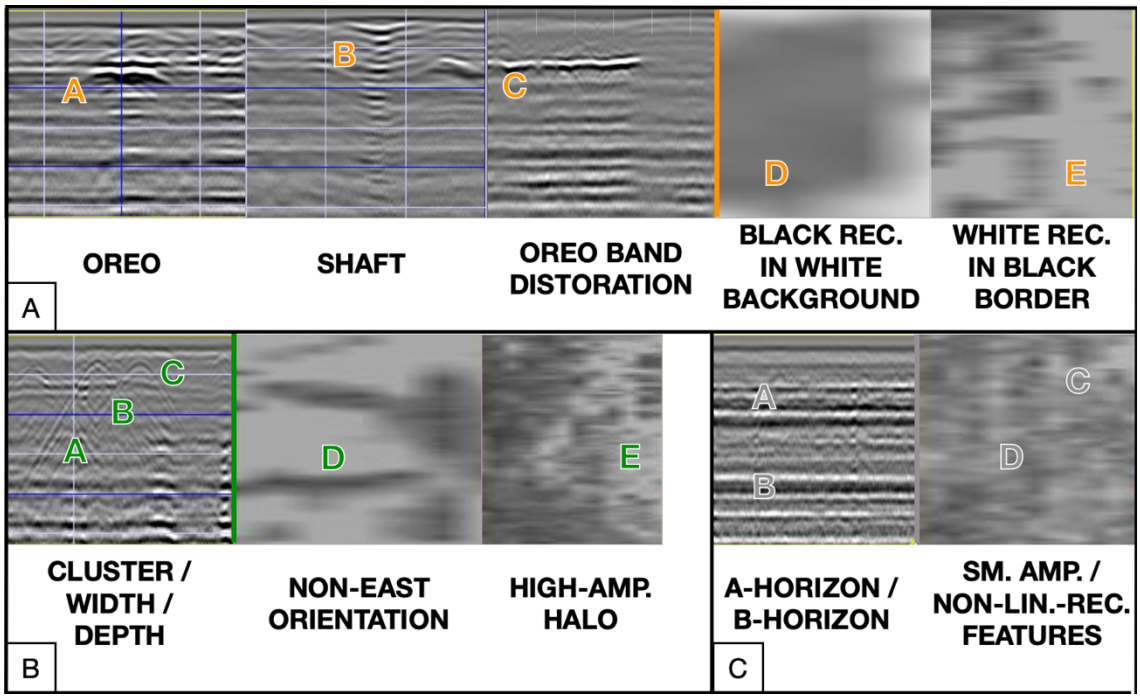

Figure 4.4. Typical images for the indicators of subsurface objects. Indicators to the left of the solid vertical lines are in the B-scans while those to the right are in the C-scans. Typical dimensions of these indicators include: A Oreo = black-white-black high amplitudes with (y, z) = (~0.5-0.6m, ~12-20ns), Shaft = vertical distortion with (z) = (~0-6ns), Oreo Band Distortion = distortion at foot of graves with (y) = (~0.2-0.5m), Black Rectangle in White Background = (x, y) = (~1.5-2m, ~1m), White Rectangle in Black Border = (x, y) = (~1-1.7m, ~0.5-1m) B Cluster = several hyperbolas, Width = (y) = (~0.5m) at 6ns done from the hyperbola peak, Depth = (z) = (~4-16ns), Non-East Orientation = distinct feature, but not pointing (relatively) straight toward the east like almost all known graves, High Amplitude Halo = white halo surrounding the center of a tree C A-Horizon = base at (z) = (~12ns), B-Horizon = base at (z) = (~25-36ns), Smoothly Varying Amplitude = no sudden changes in amplitude between time slices, Non-Linear or Rectangle Features = no sudden changes in amplitude within time slices.

We calculated the prevalence of these radar indicators and sets of indicators (hereafter collectively referred to as "indicators") among the known graves, roots, and soil. We then selected those that appeared in >70% of both training and testing datasets (highlighted in the red box in Figure 4). Indicators to the left of the red box appear considerably more often in the training than testing datasets and are therefore considered non-diagnostic for use across the entire Salem Cemetery. Those below the red box appear considerably more often in the testing than training datasets and therefore are composed of indicators imperfectly defined in the testing phase.

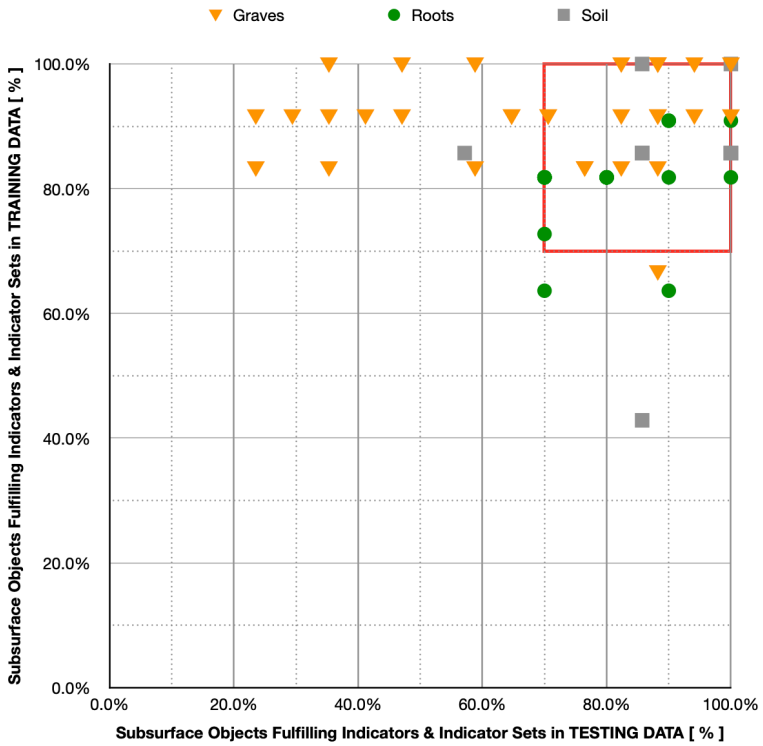

Figure 4.5. Prevalence of indicators in the training and testing datasets for known graves (orange triangles), tree roots (green circles), and undisturbed soil (gray squares). Red square highlights the indicators and indicator sets that appear in ≥70% of the subsurface objects in both the training and testing datasets.

Using Eq. 1, we estimate the confidence that each indicator set can correctly identify an unmarked grave, root, or section of soil (Figure 6). Graves have 17 indicators, roots have 31, and soil has 14. Indicators to the left of the red lines were more prevalent in the testing than in training and hence are susceptible to miss actual unmarked graves. Indicators to the right of the red lines were more prevalent in the training than in testing and hence are susceptible to generate false alarms.

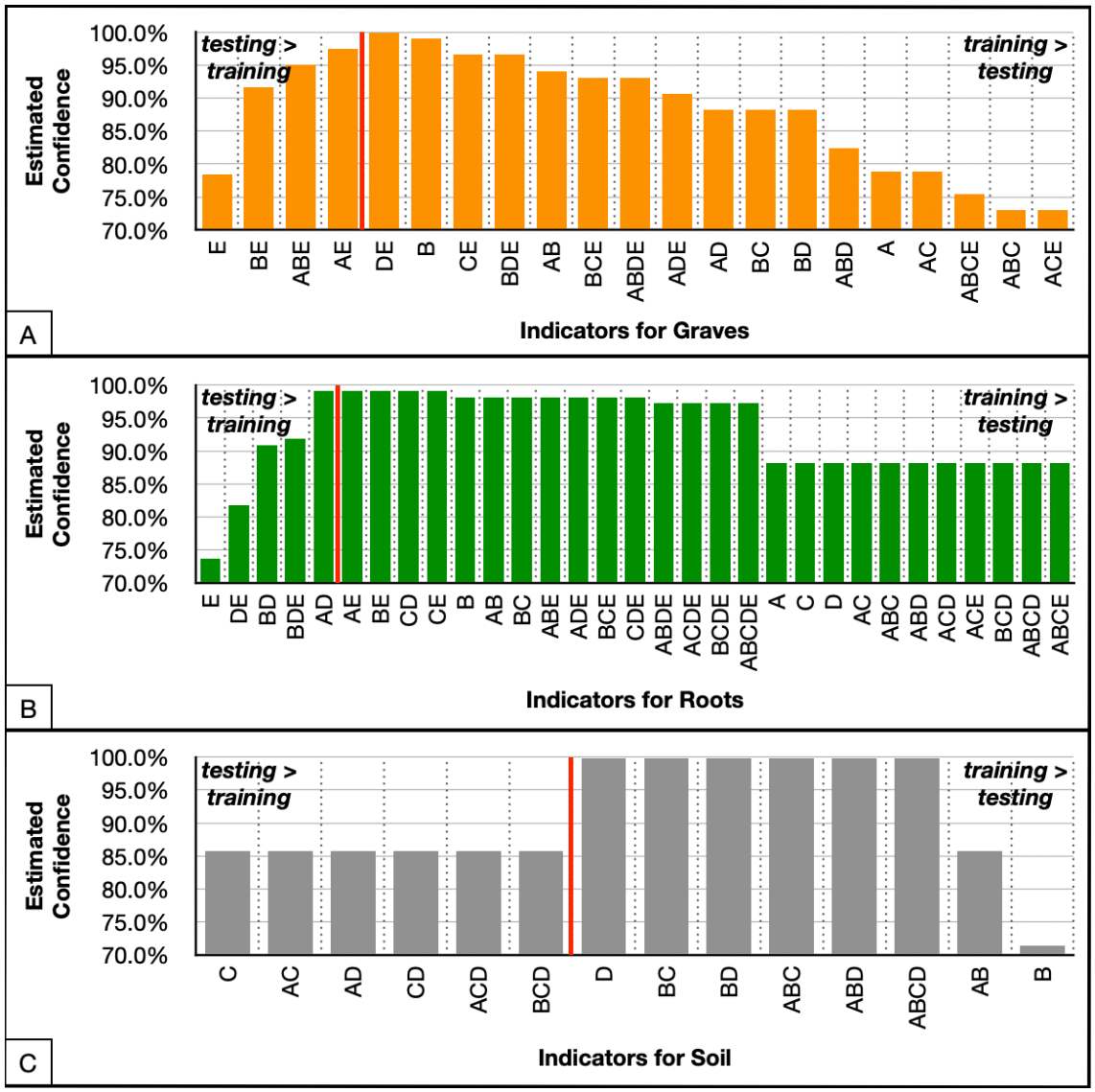

Figure 4.6. Estimated confidences in indicators to correctly identify unmarked graves, roots, and undisturbed soil. A Indicators for graves. B Indicators for roots. C Indicators for soil.

4.4.3. Verifications, Surprises, and Reclassifications

With the indicators and their associated confidence levels, we re-examined the entire Salem and ODSH datasets, including the remaining 25% of the surveyed area not used in either training or testing. This visual analysis using the indicators either verified our in-field classification of potential unmarked graves, surprised us with a potential unmarked grave not flagged as such during data collection, or reclassified a potential unmarked grave as either a root or undisturbed soil (Figure 7).

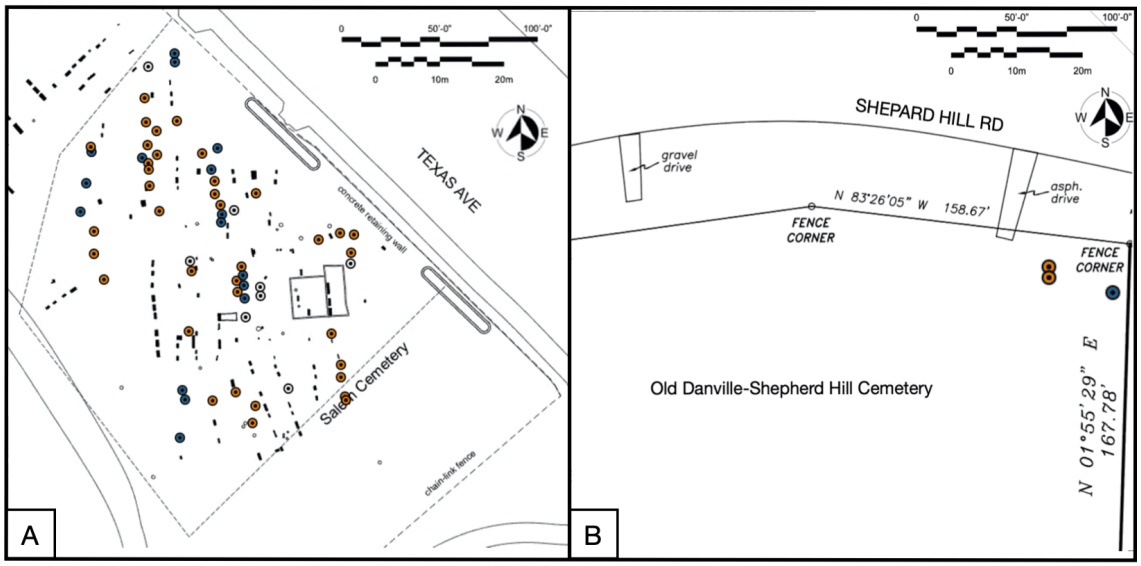

Figure 4.7. A Site map of Salem Cemetery with verified (orange dots) and surprise (blue dots) unmarked graves. Site also contains subsurface objects classified as unmarked graves during data acquisition and then reclassified as either roots or soil during data analysis (white dots). B Site map of ODSH. Same colour scheme as Salem.

4.5. Discussion

4.5.1. Initial Proficiency, Improved Proficiency, and Implications

We now calculate our proficiencies at the Salem and ODSH Cemeteries. Using Figure 8, we make one major point per subfigure:

- Fig. 8A shows our overall accuracy of in-field classifications—the sum of true-positive (blue) and true-negative (red)—increasing from 66.2% at Salem to 75.0% at ODSH, i.e. that operator proficiency improved. This suggests that our development at Salem of indicators-as-a-proxy-for-ground-truthing permits better in-field classifications at a different cemetery, ODSH.
- Fig. 8B shows the two false classifications becoming closer to 50-50 at ODSH compared to Salem. This suggests that operator bias toward false alarms or misses is balancing overall, as originally hypothesized.
- Fig. 8C shows the two true classifications (both scaled to 100%) almost swapping in value between TP and TN. This is likely due to many fewer actual unmarked graves in the surveyed area at ODSH (3 within 187 m^2) than at Salem (54 within 2851 m^2).
- Fig. 8D shows actual positive fractions (both scaled to 100%). This indicates that the true-positive fraction (TPF)—also known as "sensitivity" per Metz (1978), i.e. our ability to correctly identify subsurface objects in the midst of noise—remained relatively constant.

- Fig. 8E shows actual negative fractions (both scaled to 100%). This indicates that the true negative fraction (TNF)—also known as "specificity" per Metz (1978), i.e. our ability to correctly identify the absence of a subsurface target in the midst of noise—increased.

From the first and fifth points listed above, we conclude that detection accuracy increased because the operator—i.e. the human element—got better at looking at a livestream of raw, noisy data, seeing something that might be an unmarked grave, but concluding it actually was not one.

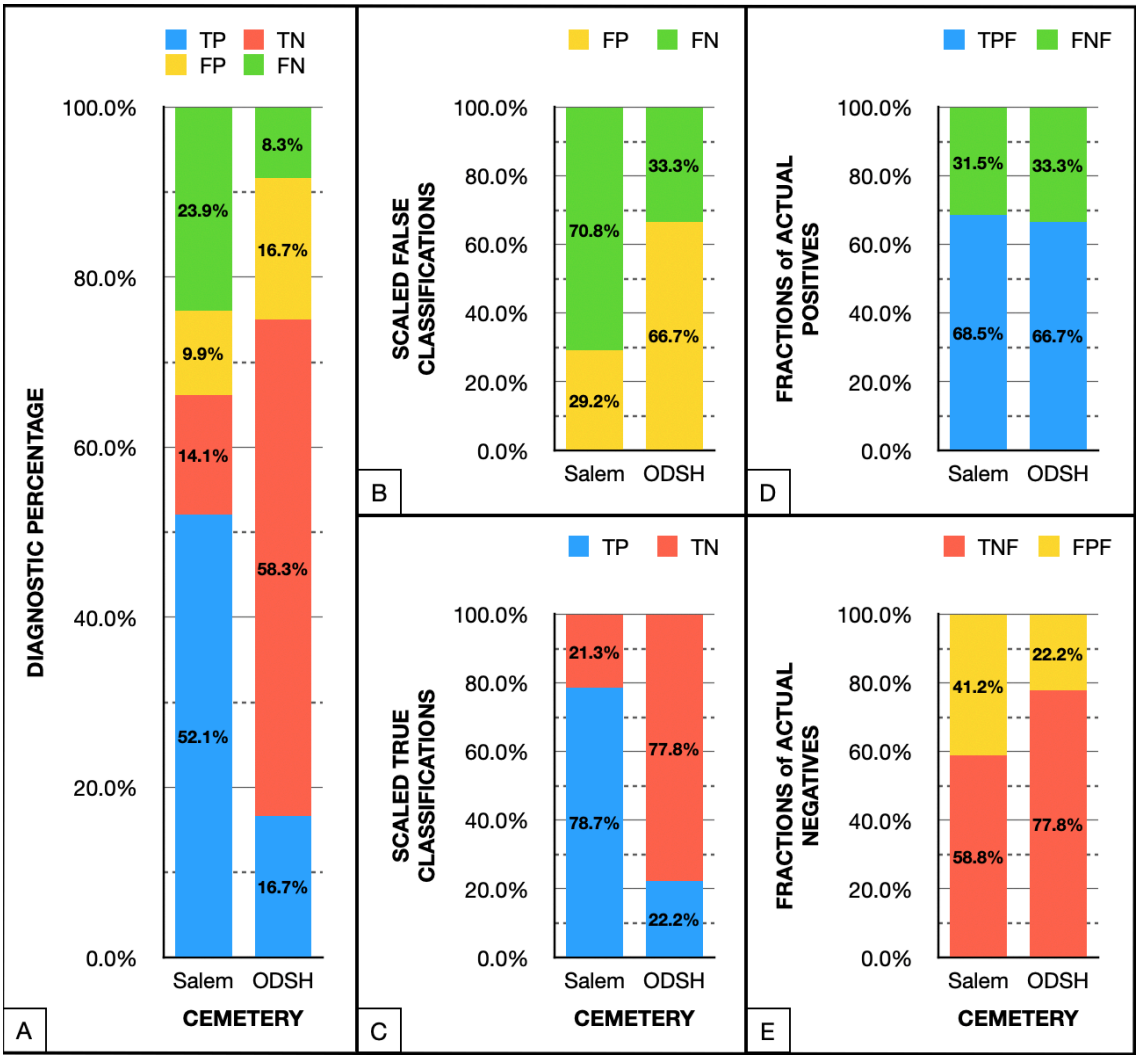

Figure 4.8. Initial and improved proficiencies. A Percentages calculated relative to the sum of all true and false classifications. B Percentages calculated relative to the sum of false classifications. C Percentages calculated relative to the sum of true classifications. D Percentages calculated relative to the sum of actual positives, both truly and falsely classified. E Percentages calculated relative to the sum of actual negatives, both truly and falsely classified. *Accuracy = TP + TN. TP = true-positive, TN = true-negative, FP = false-positive, FN = false-negative. TPF = true-positive fraction (i.e. sensitivity), FNF = false-negative fraction, TNF = true-negative fraction (i.e. specificity), FPF = false-positive fraction.*

This pilot evaluation of the GPR proficiency of the human element to detect unmarked graves promises a powerful tool with which to highlight operator biases—whether on the side of false-positives or false-negatives—as well as their skills—whether accuracy is due more to making true-positive or true-negative classifications. The protocol established herein furthermore gives a quantitative means by which to measure how further experience and effort improves or degrades proficiency.

While using a confidence threshold of 70% may represent a fair balancing of bias, other threshold may be more appropriate in different situations. For example, a cemetery staff may need to know the locations of unmarked graves as they plan new burials in an increasingly full cemetery. The geophysics practitioner may then desire to err on the side of false-positives (i.e. to lower the confidence threshold) to avoid as much as possible a new burial being accidentally made in a pre-existing grave. A historian or genealogist may seek to know the locations of unmarked graves for documentation or memorialization purposes. The geophysics practitioner may then desire to err on the side of false-negatives (i.e. to increase the confidence threshold) to avoid as much as possible

over-estimating the number of unmarked graves. Having quantitative confidence values in each type of indicator enhances the operator decision-making capacity.

4.5.2. Final Archaeological Interpretation for Community Stakeholders and Implications

The map in Figure 7A (as well as tables containing the geographic coordinates for each dot) fulfilled the basic request of the community stakeholders of the Salem Cemetery: to identify for them the locations of potential unmarked graves so they could properly memorialize those locations. The orange and blue dots let them know which pin flags from data collection to leave in the ground and also where pin flags needed to be added, respectively, until proper memorials could be secured. The white ones let them know which pin flags could be removed. But that map gave the community stakeholders (with their own limitations of time and money) no way to prioritize one potential unmarked grave location over another. As a remedy, we imported the map into ArcGIS Online, making use of popup windows and inset images (Figure 9). The open link to this map is https://arcg.is/0j4Hmf (Martin, 2022).

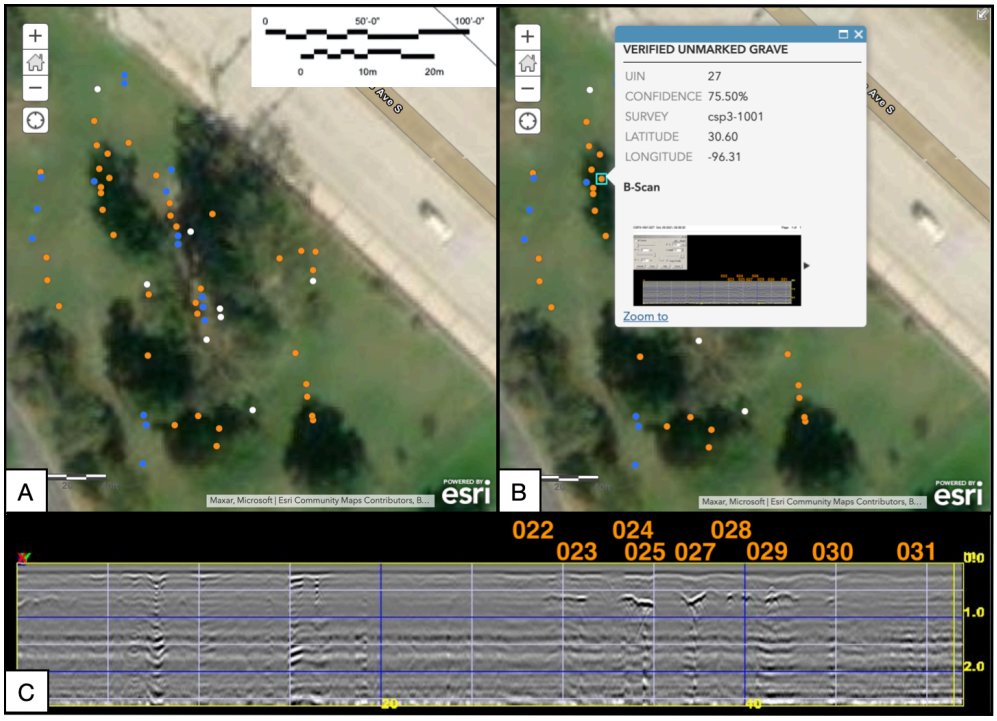

Figure 4.9. Interactive ArcGIS site map of the Salem Cemetery. A Site contains verified (orange dots) and surprise (blue dots) unmarked graves. Site also contains subsurface objects classified as unmarked graves during data acquisition and then reclassified as either roots or soil during data analysis (white dots). B Example popup window when a dot is clicked. C The B-scan showing the location of the subsurface object UIN-027, directly beneath the orange "027."

Figure 9A is effectively the same as Figure 7A; the difference being the map background (we superimposed the scale in the upper-right). But as shown in Figure 9B, clicking a dot brings up a popup window of information including: a bolded label of either "verified unmarked grave", "surprise unmarked grave", or "reclassified object", a unique identification number (UIN) for each object, our estimated confidence that the object has been correctly identified, the survey line from the survey mosaic, the geographic coordinates, and inset B- and C-scans (viewable by clicking the arrow on the right side of the B-scan). Right clicking on these images allows one to view these images

full-sized in a separate tab (Figure 9C). The UIN for each object is placed either above (in the B-scans) or to the left of (in the C-scans) where the object is visible.

This type of interactive map therefore allows community stakeholders to determine which locations to prioritize given their limitations of time and money. In a single platform, it also affords the geophysics practitioner to showcase their findings to community stakeholders from municipal officials to private citizens, to quickly train students and community volunteers in the basics of visually identifying unmarked graves, and to highlight real-world GPR data acquisition, processing, and interpretation protocols.

4.5.3. Future Research

Since the concept of measuring the proficiency of the human element was popularized in the late 1970's in the field of medicine (e.g. Metz 1978), avenues of future research opened in many fields and herein we extend the concept to geophysics. Whether a university research group, a university classroom, a geophysics company, or a public research institution, the protocol described herein allows for a quantitative and objective evaluation of operator proficiency. The operator may be a GPR specialist, university student, or community volunteer. Regardless, measurement of proficiency and its improvement as experience is gained at different sites identifies bias, affording the operator an opportunity to hone their target detection skills while quantifiably measuring their improvement.

4.6. Conclusions

Correctly identifying unmarked graves depends on more than just the proficiency of GPR technology including hardware, deployment configuration, and software. It also fundamentally depends on the proficiency of the human element, specifically that of the operator conducting the GPR survey. Proficiency is determined by true-positive, true-negative, false-positive, and false-negative percentages. Measuring proficiency requires a priori knowledge of the site's actual buried targets which, in the absence of sufficient resources for a full archaeological excavation, is not feasible. The protocol developed herein assumes that creating visual indicators of radar signatures of known subsurface objects is a suitable proxy for ground-truthing. The protocol allows reasonable estimates of the confidence that each indicator correctly identifies subsurface objects. Measuring operator proficiency identifies both relative skill in correctly identifying subsurface objects or lack thereof. It can also reveal bias in erring toward false alarms or misses. This procedure allows the operators to hone target detection skills and mitigate bias.

4.7. References

Annan, P. (2009) Chapter 1. Electromagnetic Principles of Ground Penetrating Radar, in *Ground Penetrating Radar: Theory and Applications*, pp. 1–40.

Berezowski, V., Mallett, X., Ellis, J., and Moffat, I. (2021) Using Ground Penetrating Radar and Resistivity Methods to Locate Unmarked Graves: A Review. *Remote Sens.*, **13** (15), 2880.

Bijamov, A., Fernández, J.P., Barrowes, B.E., Shamatava, I., O'Neill, K., and Shubitidze, F. (2014) Camp Butner Live-Site UXO Classification Using Hierarchical Clustering and Gaussian Mixture Modeling. *IEEE Transactions on Geoscience and Remote Sensing*, **52** (8), 5218–5229.

Dick, H.C., Pringle, J.K., Wisniewski, K.D., Goodwin, J., van der Putten, R., Evans, G.T., Francis, J.D., Cassella, J.P., and Hansen, J.D. (2017) Determining geophysical responses from burials in graveyards and cemeteries. *Geophysics*, **82** (6), B245–B255.

Hansen, J.D., Pringle, J.K., and Goodwin, J. (2014) GPR and bulk ground resistivity surveys in graveyards: Locating unmarked burials in contrasting soil types. *Forensic Sci.Int.*, **237**, E14–E29.

Harkat, H., Ruano, A.E., Ruano, M.G., and Bennani, S.D. (2019) GPR target detection using a neural network classifier designed by a multi-objective genetic algorithm. *Appl. Soft. Comput.*, **79**, 310–325.

Imai, T., Sakayama, T., and Kanemori, T. (1987) Use of Ground-Probing Radar and Resistivity Surveys for Archaeological Investigations. *Geophysics*, **52** (2), 137–150.

Lu, G., Zhao, W., Forte, E., Tian, G., Li, Y., and Pipan, M. (2020) Multi-frequency and multi-attribute GPR data fusion based on 2-D wavelet transform. *Measurement*, **166**, 108243.

Jayatilaka, L., Sengeh, D.M., Herrmann, C., Bertuccelli, L., Antos, D., Grosz, B.J., and Gajos, K.Z. (2018) PETALS: Improving Learning of Expert Skill in Humanitarian Demining. *Proceedings of the 1st ACM SIGCAS Conference on Computing and Sustainable Societies*, 1–11.

Manataki, M., Vafidis, A., and Sarris, A. (2021) GPR Data Interpretation Approaches in Archaeological Prospection. *Appl. Sci.-Basel*, **11** (16), 7531.

Martin, J.M. (2022) Historic African-American Salem Cemetery College Station, TX Identification of Unmarked Graves Using Ground-Penetrating Radar. https://arcg.is/0j4Hmf

Metz, C.E. (1978) Basic principles of ROC analysis. *Seminars in Nuclear Medicine*, **8** (4), 283–298.

Reynolds, J.M. (2011) *An introduction to applied and environmental geophysics*, John Wiley & Sons.

Sarris, A., Kalayci, T., Moffat, I., and Manataki, M. (2018) An Introduction to Geophysical and Geochemical Methods in Digital Geoarchaeology, in *Digital Geoarchaeology: New Techniques for Interdisciplinary Human-Environmental Research* (eds.Siart, C., Forbriger, M., and Bubenzer, O.), Springer International Publishing Ag, Cham, pp. 215–236.

Sherrod, L., Willever, H., Shollenberger, K., Potter, C., Thorne, R., and Kline, A. (2020) Geophysical Investigations of United States Revolutionary War Era (1777-1778) Mass Burial Sites in Pennsylvania, USA. *J. Environ. Eng. Geophys.*, **25** (4), 477–496.

Spera, S.A., Franklin, M.S., Zizzamia, E.A., and Smith, R.K. (2022) Recovering a Black Cemetery: Automated Mapping of Hidden Gravesites Using an sUAV and GIS in East End Cemetery, Richmond, VA. *Int. J. Hist. Archaeol.*

Trinks, I., and Hinterleitner, A. (2020) Beyond Amplitudes: Multi-Trace Coherence Analysis for Ground-Penetrating Radar Data Imaging. *Remote Sens.*, **12** (10), 1583.

United States Department of Agriculture (USDA). 1997. Latium Series, Established Series, Rev. GLL-SEB-ACT. https://soilseries.sc.egov.usda.gov/OSD_Docs/L/LATIUM.html

United States Department of Agriculture (USDA). 2002. Boonville Series, Established Series, Rev. WGC-ELG. https://soilseries.sc.egov.usda.gov/OSD_Docs/B/boonville.html

Yuan, D., Hong, M., and An, Z. (2018) Visualizing GPR Data Using Spatial-Subband Configuration. *IEEE Access*, **6**, 54651–54659.

Zhao, W., Forte, E., Pipan, M., and Tian, G. (2013) Ground Penetrating Radar (GPR) attribute analysis for archaeological prospection. *Journal of Applied Geophysics*, **97**, 107–117.

Zhao, W., Forte, E., Levi, S.T., Pipan, M., and Tian, G. (2015) Improved high-resolution GPR imaging and characterization of prehistoric archaeological features by means of attribute analysis. *Journal of Archaeological Science*, **54**, 77–85.

Zhao, W., Yuan, L., Forte, E., Lu, G., Tian, G., and Pipan, M. (2021) Multi-Frequency GPR Data Fusion with Genetic Algorithms for Archaeological Prospection. *Remote Sens.*, **13** (14), 2804.

5. CONCLUSIONS

The work has as its main contributions new, geophysics-based understandings of the hydrodynamics involved in alluvial aquifers. These understandings include the refilling of a depleted alluvial aquifer whose geologic cross-section is asymmetric as well as the bidirectional preferential flow pathways between an alluvial river and an adjacent alluvial aquifer. The latter is considered on both the human and geologic time scales. The work also contributes a novel application of diagnostic accuracy, failure, and bias as a protocol for the quantitative and objective evaluation of an operator's proficiency in identifying geophysically-detected subsurface targets.

The main impact of these contributions is a better ability to limit and measure the risk inherent in hydrogeologic models used to make groundwater management decisions. The better understanding of the refilling of a depleted alluvial aquifer will inform best placement practices for new groundwater wells—whether extraction or monitoring—in the cities and urbanizing corridors of alluvial floodplains. The better understanding of bidirectional flow will inform hydrogeologic models seeking to consider both the human and geologic time scales. The other major impact of this work is not only that the novel application of diagnostic accuracy, failure, and bias to geophysics allows for the measurement of proficiency, but also that it highlights the relative skills and biases in each human operator of geophysical equipment, data analysis, and modeling. As a derivative application of that last impact, this work contributes a practical and rapid means to train student volunteers and community stakeholders in the basic skills necessary to identify unmarked graves.